Universidade do Estado do Rio de Janeiro
Centro de Tecnologia e Ciências
Instituto de Física Armando Dias Tavares

Lina Milena Huertas Guativa

Measurement of dijet production with a leading proton in proton-proton collisions at $\sqrt{s} = 8$ TeV with the CMS and TOTEM detectors at the LHC

Rio de Janeiro
2017

Lina Milena Huertas Guativa

Measurement of dijet production with a leading proton in proton-proton collisions at $\sqrt{s} = 8$ TeV with the CMS and TOTEM detectors at the LHC

Tese apresentada, como requisito parcial para obtenção do título de Doutor, ao Programa de Pós-Graduação em Física, da Universidade do Estado do Rio de Janeiro.

Orientador: Prof. Dr. Alberto Franco de Sá Santoro
Coorientador: Prof. Dr. Antonio Vilela Pereira

Rio de Janeiro
2017

CATALOGAÇÃO NA FONTE
UERJ / REDE SIRIUS / BIBLIOTECA CTC/D

H887 Huertas Guativa, Lina Milena
Measurement of dijet production with a leading proton in proton-proton collisions at $\sqrt{s} = 8$ TeV with the CMS and TOTEM detectors at the LHC / Lina Milena Huertas Guativa. – 2017.
135 f. :il.

Orientador: Alberto Franco de Sá Santoro.
Coorientador: Antonio Vilela Pereira.
Tese (Doutorado) – Universidade do Estado do Rio de Janeiro, Instituto de Física Armando Dias Tavares.

1. Difração - Teses. 2. Interações próton-próton - Teses. 3. Aceleradores de partículas - Teses. 4. Solenóide de múon compacto - Teses. 5. Grande colisor de hádrones (França e Suíça) - Teses. I. Santoro, Alberto Franco de Sá. II. Pereira, Antonio Vilela. III. Instituto de Física Armando Dias Tavares. IV. Título

CDU 539.12

Assinatura

Data

Lina Milena Huertas Guativa

Measurement of dijet production with a leading proton in proton-proton collisions at $\sqrt{s} = 8$ TeV with the CMS and TOTEM detectors at the LHC

Tese apresentada, como requisito parcial para obtenção do título de Doutor, ao Programa de Pós-Graduação em Física, da Universidade do Estado do Rio de Janeiro.

Aprovada em 4 de Agosto de 2017.
Banca Examinadora:

Prof. Dr. Alberto Franco de Sá Santoro (Orientador)
Instituto de Física Armando Dias Tavares – UERJ

Prof. Dr. Antonio Vilela Pereira (Coorientador)
Instituto de Física Armando Dias Tavares – UERJ

Prof. Dr. Luiz Mundim
Instituto de Física Armando Dias Tavares – UERJ

Prof. Dr. Wagner Carvalho
Instituto de Física Armando Dias Tavares – UERJ

Prof. Dr. Gilvan Alves
Centro Brasileiro de Pesquisas Físicas

Prof. Dr. Ignacio Bediaga
Centro Brasileiro de Pesquisas Físicas

Rio de Janeiro

2017

AGRADECIMENTOS

Gostaria de agradecer especialmente aos meus orientadores Alberto Franco de Sá Santoro e Antonio Vilela Pereira, pela oportunidade, paciência e ajuda indispensável durante todos estes anos.

Um especial agradecimento aos pesquisadores Michele Arneodo, quem foi o meu supervisor durante minha estadia no CERN, e Alexander Proskuryakov quem foi o pioneiro deste trabalho.

Agradeço ao pessoal da DFNAE e da HEPGRID, pelos conselhos e ajuda.

Aos membros da banca, os professores Luiz Mundim, Wagner Carvalho, Gilvan Alves e Ignacio Bediaga por todos os comentários e sugestões.

Agradeço ao Programa de Pós Graduação em Física da UERJ, à CAPES e à FAPERJ pelo apoio econômico durante todo o trabalho.

À minha família e ao meu amor, que sempre me incentivaram com palavras de encorajamento e motivação.

Finalmente, tenho que agradecer ao Brasil, o país que me acolheu por seis anos e onde ganhei grandes amigos. A minhas amigas do alma Eliza, Luana e July.

RESUMO

HUERTAS GUATIVA, L. M. *Medição da produção de dijatos associada a um próton frontal em colisões de prótons a* $\sqrt{s} = 8$ TeV *com os detectores CMS e TOTEM no LHC*. 2017. 135 f. Tese (Doutorado em Física) – Instituto de Física Armando Dias Tavares, Universidade do Estado do Rio de Janeiro, Rio de Janeiro, 2017.

Esta tese apresenta o estudo da produção de dijatos associada a um próton espalhado na região frontal. A análise usa os dados em comum coletados simultaneamente com os experimentos CMS e TOTEM no LHC com colisões entre prótons a $\sqrt{s} = 8$ TeV durante a tomada de dados com $\beta^* = 90$ m a baixa luminosidade. Os dados correspondem a uma luminosidade integrada de $37,5\ \text{nb}^{-1}$. A análise apresenta a medição da seção de choque da produção de dijatos, em função de ξ, a fração do *momentum* longitudinal perdida pelo próton, e em função de t, o quadri-*momentum* transferido ao quadrado. A seção de choque de dijatos na região cinemática definida por $0,03 < |t| < 1\ \text{GeV}^2$, $\xi < 0,1$, e por dois jatos com *momentum* transverso $p_T > 40$ GeV, e pseudorapidez $|\eta| < 4,4$, foi medida como $\sigma_{\text{jj}}^{pX} = 22,6 \pm 1,0\,(\text{stat})\,^{+3,1}_{-3,4}\,(\text{syst}) \pm 0,9\,(\text{lumi})\,\text{nb}$. O fator de supressão da seção de choque com respeito à predição das PDFs difrativas medidas nos experimentos do HERA também é apresentado. A razão das seções de choque diffrativa simples e inclusiva é apresentada em função de x, a fração do *momentum* do párton iniciando o espalhamento duro. Esta razão na região cinemática definida acima, para valores de x na região de $-3,2 \leq \log_{10} x \leq -1,3$, foi medida como $R = (\sigma_{\text{jj}}^{pX}/\Delta\xi)/\sigma_{\text{jj}} = 0,0209 \pm 0,0008\,(\text{stat})\,^{+0,0021}_{-0,0026}\,(\text{syst})$.

Palavras-chave: Difração simples. Produção de dijatos. Roman Pots. CMS/TOTEM.

ABSTRACT

HUERTAS GUATIVA, L. M. *Measurement of dijet production with a leading proton in proton-proton collisions at* $\sqrt{s} = 8$ TeV *with the CMS and TOTEM detectors at the LHC*. 2017. 135 f. Tese (Doutorado em Física) – Instituto de Física Armando Dias Tavares, Universidade do Estado do Rio de Janeiro, Rio de Janeiro, 2017.

A study of dijet production associated with a leading proton is presented. The analysis is based on a common data set collected simultaneously with the CMS and TOTEM experiments at the LHC with proton-proton collisions at $\sqrt{s} = 8$ TeV during a dedicated run with $\beta^* = 90$ m, at low instantaneous luminosity. The data correspond to an integrated luminosity of 37.5 nb^{-1}. The analysis presents the measurements of the dijet production cross section, as a function of ξ, the proton fractional momentum loss, and as a function of t, the 4-momentum transfer squared at the proton vertex. The dijet cross section in the kinematic region defined by $\xi < 0.1$, $0.03 < |t| < 1$ GeV^2, for jets with transverse momentum $p_T > 40$ GeV, and pseudorapidity $|\eta| < 4.4$, was measured to be $\sigma_{\rm jj}^{pX} = 22.6 \pm 1.0\,({\rm stat})\,^{+3.1}_{-3.4}\,({\rm syst}) \pm 0.9\,({\rm lumi})$ nb. The suppression factor of the cross section with respect to the prediction from the diffractive PDFs measured at HERA is also presented. The ratio of the single-diffractive to inclusive dijet yields is presented as a function of x, the momentum fraction of the parton initiating the hard scattering. The ratio in the kinematic region defined above, for x values in the range $-3.2 \leq \log_{10} x \leq -1.3$, was measured as $R = (\sigma_{\rm jj}^{pX}/\Delta\xi)/\sigma_{\rm jj} = 0.0209 \pm 0.0008\,({\rm stat})\,^{+0.0021}_{-0.0026}\,({\rm syst})$.

Keywords: Single diffraction. Dijet production. Roman Pots. CMS/TOTEM.

LIST OF FIGURES

Figure 1 - Single (left panel) and double (right panel) diffractive dissociation processes in pp collisions. . . . 18
Figure 2 - Scheme of a Reggeon exchange in the reaction $12 \longrightarrow 34$ with Mandelstam variables $s = (p_1 + p_2)^2$ and $t = (p_1 - p_3)^2$. . . . 19
Figure 3 - Leading mesonic resonances ρ, f_2, a_2, w, etc., all superimposed interleaved by a Reggeon trajectory $\alpha_{\mathbb{R}}(t) = 0.5 + 0.9|t|$. . . . 21
Figure 4 - Compilation of the total σ_{tot}, elastic σ_{el} and inelastic σ_{inel} cross section measurements in pp and $p\bar{p}$ collisions. . . . 21
Figure 5 - Diffractive structure function measured by CDF compared with expectations based on dPDFs extracted by the H1 Collaboration. . . . 23
Figure 6 - Ratio of diffractive to non-diffractive dijet event rates measured by CDF. 24
Figure 7 - Results for diffractive dijet production at $\sqrt{s} = 7$ TeV. . . . 25
Figure 8 - The LHC experiments . . . 27
Figure 9 - CMS detector . . . 28
Figure 10 - Longitudinal view of the CMS detector. . . . 30
Figure 11 - CMS forward subdetectors . . . 31
Figure 12 - L1 trigger in CMS . . . 32
Figure 13 - TOTEM experiment . . . 35
Figure 14 - The vacuum chambers of a RP unit accommodating the horizontal and the vertical pots and the Beam Position Monitor. . . . 36
Figure 15 - Overlap between the horizontal and vertical detectors. . . . 37
Figure 16 - Location of the RP TOTEM stations. . . . 37
Figure 17 - The acceptance of a common CMS/TOTEM experiment in the azimuth-pseudorapidity plane. . . . 39
Figure 18 - The pseudorapidity distribution of charged particles and of the energy flow at $\sqrt{s} = 14$ TeV . . . 40
Figure 19 - Diffractive dijet cross section as a function of t (left) and ξ (right) for events with at least two jets with $p_T > 40$ GeV. . . . 43
Figure 20 - Diffractive dijet cross section as a function of t (left) and ξ (right) for events with at least two jets with $p_T > 40$ GeV. . . . 44
Figure 21 - $\log(\xi)$ vs $\log(|t|)$ acceptance for sector 45 (left) and sector 56 (right) with POMWIG. . . . 44
Figure 22 - $\log(\xi)$ vs $\log(|t|)$ acceptance for sector 45 (left) and sector 56 (right) with PYTHIA8 4C. . . . 45
Figure 23 - $\log(\xi)$ vs $\log(|t|)$ acceptance for sector 45 (left) and sector 56 (right) with PYTHIA8 CUETP8M1. . . . 45

Figure 24 - Ratio between data and POMWIG yields as a function of β, after all selection cuts; the MC includes the rapidity survival probability. 46
Figure 25 - Distribution of the z primary vertex position. 47
Figure 26 - Distributions of t, ξ, θ_x^* and θ_y^* for the selected events in sector 45. . . . 49
Figure 27 - Distributions of t, ξ, θ_x^* and θ_y^* for the selected events in sector 56. . . . 50
Figure 28 - Roman Pot hit position for MC events with a proton in the RP acceptance in sector 45 (left panel) and sector 56 (right panel). 52
Figure 29 - Roman Pot acceptance versus t, ξ, θ_x^* and θ_y^* for events with a proton in sector 56. 53
Figure 30 - Ratio of the RP acceptances using the parametrised simulation and the RP detector simulation as a function of θ_x^* and ξ. 54
Figure 31 - Roman Pot acceptance versus t, ξ, θ_x^* and θ_y^* for events with a proton in sector 56, after the correction described in the text. 55
Figure 32 - Ratio of the RP acceptances using the parametrised simulation and the RP detector simulation as a function of θ_x^* and ξ, after the correction described in the text. 56
Figure 33 - Roman Pot acceptance versus t, ξ, θ_x^* and θ_y^* for events with a proton traversing the top and bottom RPs, with the parametrised simulation and the full RP detector simulation. 57
Figure 34 - Schematic diagram of diffractive dijet production. The diagram shows an example of the gg$\rightarrow$ jet jet process; the qq and gq initial states also contribute. 59
Figure 35 - Number of merged events as a function of the lumi section. 60
Figure 36 - Efficiency of the "HLT_L1DoubleJet20" trigger as a function of the transverse momentum of the second jet. 61
Figure 37 - Variation of the trigger efficiency fit parameters within uncertainties. . 62
Figure 38 - Roman Pot hit position in sector 45 (left panel) and sector 56 (right panel) for data events after all selection cuts. 64
Figure 39 - Distributions of jet p_T, η and x for events before the diffractive selection. 66
Figure 40 - Distributions of jet p_T, η, $\Delta\eta$ and $\Delta\phi$, as well as x, θ_x^*, θ_y^*, t, ξ and β for the selected events in which the proton is detected in sector 45. . . 67
Figure 41 - Distributions of jet p_T, η, $\Delta\eta$ and $\Delta\phi$, as well as x, θ_x^*, θ_y^*, t, ξ and β for the selected events in which the proton is detected in sector 56. . . 68
Figure 42 - Distributions of the dijet invariant mass M_{jj}, mass of the system X, M_X, and the dijet mass fraction R_{jj}, for the selected events with the proton detected in sector 45. 69

Figure 43 - Distributions of the dijet invariant mass M_{jj}, mass of the system X, M_X, and the dijet mass fraction R_{jj}, for the selected events with the proton detected in sector 56. 69
Figure 44 - Distribution of $\xi_{\text{CMS}} - \xi_{\text{TOTEM}}$ for events with a proton detected in sector 45 (left panel) and sector 56 (right panel). 70
Figure 45 - Distribution of ξ_{TOTEM} for sector 45 (left) and sector 56 (right). 71
Figure 46 - Distribution of ξ_{TOTEM} after the $\xi_{\text{CMS}} - \xi_{\text{TOTEM}}$ cut for sector 45 (left) and sector 56 (right). 71
Figure 47 - Distribution of t after the $\xi_{\text{CMS}} - \xi_{\text{TOTEM}}$ cut for sector 45 (left) and sector 56 (right). 72
Figure 48 - Distribution of $\xi_{\text{CMS}} - \xi_{\text{TOTEM}}$ for sector 45 (left) and 56 (right). 73
Figure 49 - Distribution of ξ for sector 45 (left) and 56 (right). 73
Figure 50 - Distribution of ξ after the $\xi_{\text{CMS}} - \xi_{\text{TOTEM}} \leq 0$ cut for sector 45 (left) and sector 56 (right). 74
Figure 51 - Distribution of t after the $\xi_{\text{CMS}} - \xi_{\text{TOTEM}} \leq 0$ cut for sector 45 (left) and sector 56 (right). 74
Figure 52 - Distribution of $\xi_{\text{CMS}} - \xi_{\text{TOTEM}}$ for events in sector 45 (left) and sector 56 (right), for top and bottom configurations. 75
Figure 53 - Distribution of x (left panel) and y (right panel) position of tracks in the RP stations. 76
Figure 54 - Distribution of x (left panel) and y (right panel) position of tracks in the RP stations. 77
Figure 55 - Distribution of t (left panel) and ξ (right panel). 78
Figure 56 - Response matrix for t, ξ and $\log(x)$ with POMWIG. 80
Figure 57 - Response matrix for t, ξ and $\log(x)$ with PYTHIA8 4C. 81
Figure 58 - Response matrix for t, ξ and $\log(x)$ with PYTHIA8 CUETP8M1. 82
Figure 59 - Response matrix for $\log(x)$ with PYTHIA6. 82
Figure 60 - Response matrix for $\log(x)$ with HERWIG6. 83
Figure 61 - Response matrix for $\log(x)$ with PYTHIA8 4C. 83
Figure 62 - Response matrix for $\log(x)$ with PYTHIA8 CUETP8M1. 84
Figure 63 - Relative change of χ^2 distribution. 84
Figure 64 - Relative change of χ^2 distribution. 85
Figure 65 - Relative change of χ^2 distribution. 85
Figure 66 - $\chi^2_{unfolded}$ values per iteration for the t (left), ξ (central) and $\log(x)$ (right) distributions for events in sector 45. 86
Figure 67 - $\chi^2_{unfolded}$ values per iteration for the t (left), ξ (central) and $\log(x)$ (right) distributions for events in sector 56. 86
Figure 68 - $\chi^2_{unfolded}$ values per iteration for the $\log(x)$ distribution. 87
Figure 69 - Unfolding bias for events in sector 45. 88

Figure 70 - Unfolding bias for events in sector 56. 89
Figure 71 - Relative variation of each systematic uncertainty for events in sector 45. 95
Figure 72 - Relative variation of each systematic uncertainty for events in sector 56. 96
Figure 73 - Differential cross section as a function of t (top) and ξ (bottom) for single-diffractive dijet production. 98
Figure 74 - Differential cross section as a function of t (left) and as a function of ξ (right) for single-diffractive dijet production. 100
Figure 75 - Differential cross section as a function of t (left) and ξ (right) for single-diffractive dijet production when the results of the two sectors are averaged. 101
Figure 76 - Distribution of ξ_{CMS} (left) and the differential cross section as a function of ξ for single-diffractive dijet production (right). 102
Figure 77 - Differential cross section as a function of ξ_{CMS} for single-diffractive dijet production. 103
Figure 78 - Inclusive dijet cross section as a function of x. 104
Figure 79 - Single-diffractive dijet cross section as a function of $\log(x)$. 105
Figure 80 - Ratio of the single-diffractive and inclusive dijet event yields in the region of $0.03 < |t| < 1$ GeV and $\xi < 0.1$ when the proton is detected in the RPs located in sector 45 (top panel) and 56 (bottom panel). . . 106
Figure 81 - Ratio of the single-diffractive and inclusive dijet cross sections in the region given by $\xi < 0.1$ and $0.03 < |t| < 1$ GeV^2. 107
Figure 82 - Ratio of the single-diffractive and inclusive dijet cross sections in the region of $0.03 < |t| < 1$ GeV^2 and $\xi < 0.1$. 107
Figure 83 - Distributions of energy for the PF Gamma particle. 115
Figure 84 - Distributions of energy for the PF Neutral Hadron particle. 115
Figure 85 - Distributions of energy for the PF Gamma HF particle. 116
Figure 86 - Distributions of energy for the PF Hadron HF particle. 116
Figure 87 - Cross sections as a function of t and ξ, as well as the ratio of the single-diffractive and non-diffractive event yields. 118
Figure 88 - Cross sections as a function of t and ξ, as well as the ratio of the single-diffractive and non-diffractive event yields. 118
Figure 89 - Cross sections as a function of t and ξ, as well as the ratio of the single-diffractive and non-diffractive event yields. 119
Figure 90 - Cross sections as a function of t and ξ, as well as the ratio of the single-diffractive and non-diffractive event yields. 119
Figure 91 - Cross sections as a function of t and ξ, as well as the ratio of the single-diffractive and non-diffractive event yields. 120
Figure 92 - Cross sections as a function of t and ξ, as well as the ratio of the single-diffractive and non-diffractive event yields. 120

Figure 93 - Cross sections as a function of t and ξ, as well as the ratio of the single-diffractive and non-diffractive event yields. 121
Figure 94 - Cross sections as a function of t and ξ, as well as the ratio of the single-diffractive and non-diffractive event yields. 121
Figure 95 - Cross sections as a function of t and ξ, as well as the ratio of the single-diffractive and non-diffractive event yields. 122
Figure 96 - Cross sections as a function of t and ξ, as well as the ratio of the single-diffractive and non-diffractive event yields. 122
Figure 97 - Number of events as a function of t after the full event selection with the cut in $p_T > 30$ GeV. 124
Figure 98 - Number of events as a function of t after the full event selection with the cut in $p_T > 35$ GeV (left panel) and $p_T > 40$ GeV (right panel) for the jets. 124
Figure 99 - Ratio of the single-diffractive to the non-diffractive events with the cut in $p_T > 30$ GeV (left), $p_T > 35$ GeV (center) and $p_T > 40$ GeV (right). 125
Figure 100 - Ratio of the single-diffractive to the non-diffractive events. 125
Figure 101 - Distribution of $\xi_{\text{CMS}} - \xi_{\text{TOTEM}}$ for sector 45 (left panel) and sector 56 (right panel). 127
Figure 102 - Distribution of ξ_{TOTEM} for sector 45 (left) and sector 56 (right) before the $\xi_{\text{CMS}} - \xi_{\text{TOTEM}}$ cut. 127
Figure 103 - Distribution of ξ_{TOTEM} for sector 45 (left) and for sector 56 (right) after the $\xi_{\text{CMS}} - \xi_{\text{TOTEM}}$ cut. 128
Figure 104 - Distribution of t for sector 45 (left panel) and for sector 56 (right panel), after all cuts including the $\xi_{\text{CMS}} - \xi_{\text{TOTEM}}$ cut. 128
Figure 105 - Cross sections as a function of t and ξ. 135

LIST OF TABLES

Table 1 - LHC parameters for proton-proton collisions during the period of 2012. 27

Table 2 - Cross sections for Pomeron and Reggeon exchange contributions in POMWIG in the kinematical region defined by $p_T > 40$ GeV, $|\eta| < 4.4$, $0.03 < |t| < 1.0$ GeV^2 and $\xi < 0.1$. 42

Table 3 - Correction factors related to the proton reconstruction. 51

Table 4 - Merged CMS+TOTEM samples for dijet events at 8 TeV. 60

Table 5 - Merged CMS+TOTEM samples for minimum-bias events at 8 TeV. . . 60

Table 6 - Merged CMS+TOTEM samples for zero-bias events at 8 TeV. 60

Table 7 - Thresholds used for PF objects. 63

Table 8 - Number of events after each selection. 64

Table 9 - Individual contributions of the different systematic effects to the measurement of the t and ξ cross sections for single-diffractive dijet production in the kinematic region of $p_T > 40$ GeV, $|\eta| < 4.4$, $\xi < 0.1$ and $0.03 < |t| < 1$ GeV^2. 92

Table 10 - Individual contributions of the different systematic effects to the measurement of the inclusive dijet cross section, in the kinematic region of $p_T > 40$ GeV, $|\eta| < 4.4$ and $-3.2 \leq \log_{10} x \leq -1.3$. 93

Table 11 - Individual contributions of the different systematic effects to the measurement of the single-diffractive dijet cross section as a function of x in the kinematic region of $p_T > 40$ GeV, $|\eta| < 4.4$, $\xi < 0.1$, $0.03 < |t| < 1$ GeV^2 and $-3.2 \leq \log_{10} x \leq -1.3$. 93

Table 12 - Individual contributions of the different systematic effects to the measurement of the ratio of the single-diffractive and inclusive dijet cross sections in the region of $p_T > 40$ GeV, $|\eta| < 4.4$, $\xi < 0.1$, $0.03 < |t| < 1$ GeV^2 and $-3.2 \leq \log_{10} x \leq -1.3$. 94

Table 13 - Individual contributions of the different systematic effects to the measurement of the slope of the t distributions. 99

Table 14 - Individual contributions of the different systematic effects to the measurement of the t cross section for sector 45. 130

Table 15 - Individual contributions of the different systematic effects to the measurement of the t cross section for sector 56 are shown separately. 130

Table 16 - Individual contributions of the different systematic effects to the measurement of the ξ cross section for sector 45. 131

Table 17 - Individual contributions of the different systematic effects to the measurement of the ξ cross section for sector 56. 131

Table 18 - Individual contributions of the different systematic effects to the measurement of the non-diffractive dijet cross section as a function of x. 132
Table 19 - Individual contributions of the different systematic effects to the measurement of the single-diffractive cross section as a function of x. . . . 132
Table 20 - Individual contributions of the different systematic effects to the measurement of the single-diffractive to non-diffractive dijet yields for sector 45. 133
Table 21 - Individual contributions of the different systematic effects to the measurement of the single-diffractive to non-diffractive dijet yields for sector 56. 133
Table 22 - Merged CMS+TOTEM samples for dijets events at 8 TeV. 134

CONTENTS

	INTRODUCTION	15
1	**THEORICAL OVERVIEW**	17
1.1	**Diffraction**	17
1.2	**Soft diffraction**	19
1.2.1	Regge Theory	19
1.3	**Hard Diffraction**	22
2	**THE CMS AND TOTEM EXPERIMENTS**	26
2.1	***The Large Hadron Collider*** **(LHC)**	26
2.2	**Compact Muon Solenoid**	28
2.2.1	Subdetectors	28
2.2.2	Trigger and computing	31
2.3	**Data Quality Monitoring (DQM) for physics analysis**	32
2.3.1	Online and Offline DQM	33
2.3.2	DQM shifts	34
2.3.3	Service Work Activities	34
2.4	**TOTEM experiment**	34
2.4.1	The RP detector	35
2.4.2	T1 and T2 detectors	36
2.5	**CMS/TOTEM combined acceptance**	38
3	**MONTE CARLO SIMULATION**	41
3.1	**Roman Pot detectors acceptance and resolution**	46
4	**DATA ANALYSIS**	58
4.1	**Data Samples**	58
4.2	**Event selection**	61
4.3	**Background**	65
4.4	**Unfolding**	78
5	**RESULTS**	90
5.1	**Systematic uncertainties**	90
5.2	**Extraction of the cross section as a function of t and ξ**	97
5.2.1	Comparison to CMS-only analysis	102
5.3	**Extraction of the ratio of the single-diffractive to inclusive dijet yields**	103
	CONCLUSIONS	108
	REFERENCES	110
	APPENDIX A – Particle Flow thresholds	114
	APPENDIX B – Effect of the reweighting on the generators	117

APPENDIX C – p_T threshold in t distribution 123
APPENDIX D – Background 126
APPENDIX E – Systematic Uncertainties 129
APPENDIX F – Prompt Reconstruction vs Reprocessed data 134

INTRODUCTION

In pp collisions a significant fraction of the total cross section is attributed to diffractive processes. Diffractive events are characterised by the fact that at least one of the two protons emerges from the interaction intact or excited into a low mass state, with only a small energy loss. These processes can be explained by the exchange of a virtual object, the so-called *Pomeron*, with the vacuum quantum numbers (1); no hadrons are therefore produced in a large rapidity range adjacent to the scattered proton, the so-called Large Rapidity Gap (LRG).

Hard diffraction has been studied in hadron-hadron and electron-proton collisions at CERN (2), Fermilab (3; 4; 5; 6), and DESY (7; 8; 9; 10). In the presence of a hard scale, diffractive processes can be described in terms of the convolution of diffractive parton distribution functions (dPDFs) and hard scattering cross sections, which can be calculated in pQCD. The dPDFs have been determined by the HERA experiments (7; 8; 9) by means of QCD fits to inclusive diffractive deep inelastic scattering data. The diffractive PDFs have been successfully applied to describe different hard diffractive processes in *ep* collisions. This success is based on the factorization theorem proven for electron-proton interactions, and on the validity of the QCD evolution equations for the dPDFs (11; 12; 13). However, in hard diffractive hadron-hadron collisions factorization is expected to be broken because of the presence of soft rescattering between the spectator partons. This leads to the suppression of the observed diffractive cross section in hadron-hadron interactions (14). The suppression factor, often called rapidity gap survival probability, was estimated to be $\sim 10\%$ at Tevatron energies (5).

Experimentally, diffractive events can be selected either by exploiting the presence of the LRG or by measuring the scattered proton. The latter method is superior since it gives direct access to the measurement of t, the squared four momentum transfer at the proton vertex, and allows the suppression of the contribution from proton-dissociative events, in which the proton dissociates into a low-mass state. As the acceptance in pseudorapidity at CMS (15) is roughly $|\eta| < 2.5$ for tracking information and $|\eta| < 5$ for calorimeter information, the measurement of the scattered proton is not possible. This is however achieved with the coverage in the forward direction by the TOTEM (16; 17) experiment.

This thesis presents the measurement of single-diffractive dijet production at LHC, $pp \to Xp$ or $pp \to pX$, with X including two jets; the system X is measured in CMS, and the scattered proton in the TOTEM Roman Pots (RPs). The single-diffractive dijet cross section is measured as a function of ξ, the proton fractional momentum loss, and t. The ratio of the single-diffractive to inclusive dijet cross section is measured as a function of x, the longitudinal momentum fraction of the proton carried by the parton. This is the

first measurement of hard diffraction with a proton tag at LHC and complements that presented in Ref. (18), which is based on CMS-only information. This thesis starts with a review of Regge theory, the concept of soft and hard Pomeron, as well as the diffraction phenomenology at HERA and the Tevatron. In Chapter 2, the main features of the LHC accelerator, and the CMS and TOTEM detectors are discussed. The simulation used in the analysis is described in Chapter 3. The data analysis is described in detail in Chapter 4, along with the used data samples. The results are presented in Chapter 5. The conclusions of the analysis are presented in Chapter 6.

1 THEORICAL OVERVIEW

The elementary particles and their fundamental interactions are extremely well described within the Standard Model (SM). The SM is a gauge field theory developed as a result of experimental and theorical research. The SM provides an unified theoretical description of the three fundamental interactions (strong, week and electromagnetic). The elementary particles within this theory are classified according to their spin: fermions have half-integer spin while bosons have integer spin.

QCD (*Quantum ChromoDynamics*) is the theory of the strong interactions within the Standard Model of particle physics. The fundamental degrees of freedom of QCD, quarks and gluons, are already well established even though they cannot be observed as free particles, but only in color neutral bound states (confinement), mesons and baryons (hadrons). Today, QCD has firmly occupied its place as part of the SM. However, there is a large number of observations that lack a detailed qualitative or quantitative explanation.

QCD has achieved a remarkable success in describing the high energy and large momentum transfer processes, where the quarks in the hadrons behave, to some extent, as free particles and a perturbative approach can therefore be used. Nevertheless, the largest fraction of hadronic interactions involve low momentum transfer processes, where a transition from partons to hadrons occurs, denoted as hadronization. In this regime, the effective strong coupling constant is large and a description with a perturbative approach is not possible. The hadronization of a single quark creates a tight cone of particles called Jet. Jets are measured in particle detectors, rather than quarks, and studied in order to determine the properties of the original quarks.

When two hadrons collide, inelastic processes contribute to around 50% of the cross section. The remaining almost-half of the total cross section is due to elastic (around 25%) and (mainly soft) *diffractive* processes. The latter can be characterised by the exchange of a color-singlet object (historically known as *Pomeron*) resulting in the dissociation of one (single diffraction) or both (double diffraction) incoming hadrons, which are scattered at very small angles and carry most of the initial energy (Figure 1).

This chapter introduces diffractive dissociation processes, discussing the necessary formalism of Regge theory, the Pomeron, some aspects of diffraction at HERA and hard diffraction at hadron colliders.

1.1 Diffraction

The term diffraction comes from the optical analogy and was introduced in nuclear high energy physics in the 50's by Landau and collaborators (19). Within this terminology

Figure 1 - Single (left panel) and double (right panel) diffractive dissociation processes in pp collisions.

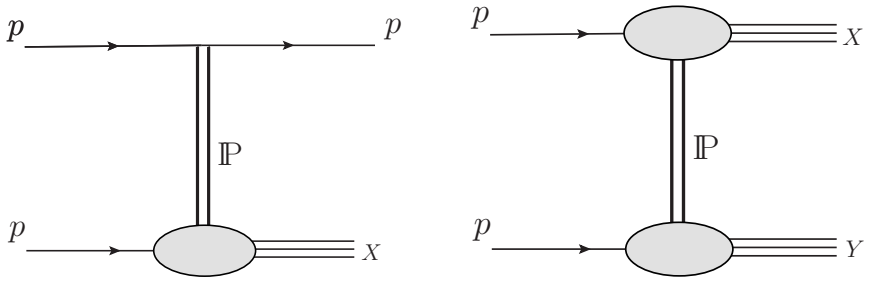

Source: The author, 2017.

the propagation and the interaction of the hadrons are nothing but the absorption of their wave function caused by the many inelastic channels open at high energy. In optics the intensity of the diffracted light at small angles and large wave numbers k is given by:

$$I(\phi) \simeq I(0)(1 - Bk^2\phi^2), \tag{1}$$

where $B \propto R^2$ (R is the obstacle radius) and $q \simeq k\phi$ is the momentum transfer.

Diffractive processes have a similar behavior, the cross sections at low values of $|t|$ behave as:

$$\frac{d\sigma}{dt} = \left.\frac{d\sigma}{dt}\right|_{t=0} e^{B|t|} \simeq \left.\frac{d\sigma}{dt}\right|_{t=0} (1 - B|t|), \tag{2}$$

Once again B is proportional to the obstacle size, and as in optics a dip followed by a secondary maximum has also been observed.

In terms of particle physics, hadronic diffractive processes can be formulated as a reaction in which no quantum numbers are exchanged between the colliding particles and a large, non exponentially suppressed, rapidity gap (LRG) is observed. The requirement of LRG to identify diffractive processes was proposed by Bjorken in the 90's when the final state is not fully reconstructed (14).

The theorical and successful framework for diffraction is Regge theory. This theory models the hadronic interaction in terms of exchanges of objects called as Reggeons and Pomerons. Even though, the true nature of these objects in terms of QCD are not straightforward.

Diffractive processes are predominantly is soft (interaction with small momentum transfer). In the 90's, the UA8 and HERA experiments showed that diffractive scattering also have a hard component. For example, jets with large momentum transfer were observed in addition to the scattered proton.

Figure 2 - Scheme of a Reggeon exchange in the reaction $12 \longrightarrow 34$ with Mandelstam variables $s = (p_1 + p_2)^2$ and $t = (p_1 - p_3)^2$.

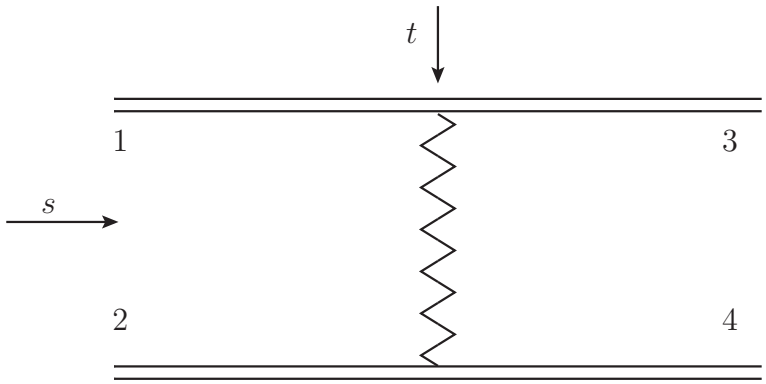

Source: The author, 2017.

1.2 **Soft diffraction**

Soft diffractive processes are charaterized by low values ($\sim (\mathrm{MeV/c})^2$) of the squared four momentum transfer t. The theorical framework is the Regge theory, which describes the hadronic interactions through the exchange of Reggeon trajectories called Reggeons.

1.2.1 Regge Theory

This theory predicts the total cross section as a function of the center-of-mass energy. It is based on the general properties of the S-matrix, unitarity, analycity and crossing. The S-matrix describes the transition between an initial state $|i\rangle$ and a final state $|f\rangle$. The matrix elements of S can be represented as:

$$S_{if} = \delta_{if} + i(2\pi)^4 \delta^4 \left(\sum_i p_i - \sum_f p_f \right) A_{if} \tag{3}$$

where A_{if} is the scattering amplitude and written usually in terms of the Madelstam variables s, t, u. In the case of the two body process $12 \longrightarrow 34$ (Fig. 2), the variables are defined as:

$$s = (p_1 + p_2)^2 \quad t = (p_1 - p_3)^2 \quad u = (p_1 - p_4)^2 \tag{4}$$

where s expresses the energy of the collision and t reflects the momentum transfer connected with the scattering polar angle θ of the first particle.

Following from the analyticity and crossing symmetries of the amplitude (20; 21), Regge theory states that the scattering amplitude $A_{12\to34}(s,t)$ shown in Figure 2 can be related to the crossed one $A_{1\bar{3}\to\bar{2}4}(s',t')$ where $s'=t$, $t'=s$ and $\bar{2}$, $\bar{3}$ are the antiparticles of 2, 3, respectively. In other words, it relates the high energy behavior of the s-channel amplitude to the t-channel one provided that one substitutes antiparticles of 2, 3 and their four-momenta.

Regge theory describes the scattering process in the asymptotic limit. The theory predicts that the asymptotic behavior of the scattering in the s-channel, where $s\to\infty$ and $s >> t$, is determined by the poles in the complex angular momentum plane $A(l,t)$ in the t-channel. These poles are found by interpolating the resonances in the t-channel due to the exchange of particles. These particles lie in linear trajectories called Reggeons. The general expression for a straight line trajectory is:

$$\alpha(t)=\alpha(0)+\alpha' t \tag{5}$$

where $\alpha(0)$ and α' are denoted as the trajectory intercept and the slope, respectively.

The leading mesonic trajectories, i.e. those with the largest $\alpha(0)$, were fitted in data giving a Reggeon intercept $\alpha(0)\sim 0.5$, as shown in Figure 3 (22). Note that the Reggeon trajectory interpolates mesonic resonances of different quantum numbers. For instance, f_2 carries parities $P=+1$, $C=+1$ whereas ρ carries $P=-1$, $C=-1$, and similarly for the other trajectories.

According to Regge theory, the total cross section can be parametrized as a function of the square of the center-of-mass energy s as:

$$\sigma_{tot}\sim s^{\alpha(0)-1} \qquad s\longrightarrow\infty \tag{6}$$

where $\alpha(0)$, are the intercepts of the trajectories exchanged.

According to Eq. 6, a Reggeon intercept smaller than one means that the total hadronic cross section should be a monotonically decreasing function of s.

Experimentally it was observed that the total cross section at higher center-of-mass energies (Figure 4 (23)) increased as a function of the center-of-mass energy, which was in contradiction with the mechanism based on a Reggeon exchange that predicted a slow decrease of the total cross section.

Donnachie and Landshoff (24) later introduced the description of the total cross section for pp, p$\bar{\text{p}}$, $\phi^{\pm}$p, $K^{\pm}$p, γp . They performed a fit to all the data available at that time using only two main trajectories:

$$\sigma_{\text{tot}}=Xs^{0.0808}+Ys^{-0.4525} \tag{7}$$

where X and Y are parameters which depend on the process. The first trajectory, called

Figure 3 - Leading mesonic resonances ρ, f_2, a_2, w, etc., all superimposed interleaved by a Reggeon trajectory $\alpha_{\mathbb{R}}(t) = 0.5 + 0.9|t|$.

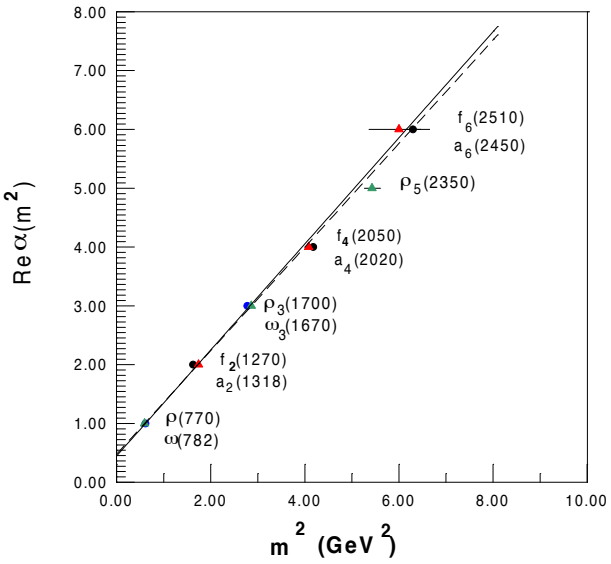

Source: DESGROLARD et al., 2000, p.556.

Figure 4 - Compilation of the total σ_{tot}, elastic σ_{el} and inelastic σ_{inel} cross section measurements in pp and p$\bar{\text{p}}$ collisions.

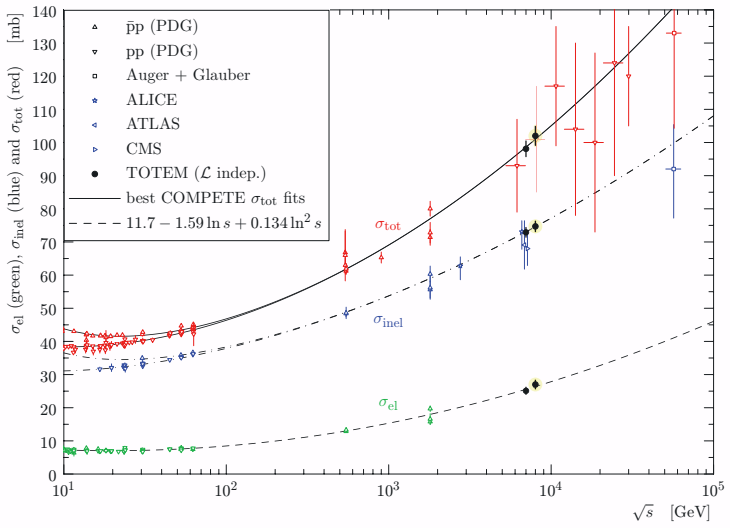

Source: TOTEM COLLABORATION, 2013, p.3.

Pomeron trajectory, has an intercept $\alpha_{I\!P}(0) = 1.0808$ while the second represents a Reggeon trajectory and has an intercept $\alpha_{I\!R}(0) = 0.5475$. The Pomeron is responsible for the rise of the total cross section as a function of the center-of-mass energy.

The introduction of the notion of duality (25; 26) gives to Regge theory some technical difficulties. This inspired Veneziano to propose a celebrated formula to avoid double counting (27) and gave more applicability to Regge theory. A more elaborated method with application to almost all soft interactions is the Three Component Deck Model, which gives a good description of the diffractive dissociation phenomena (28; 29; 30).

1.3 **Hard Diffraction**

Ingelman and Schlein (31) proposed in 1985 that the observation of high p_T jets would probe the partonic structure of the Pomeron. The first observation of jet production was reported by the UA8 collaboration (32) at CERN. The H1 (33) and ZEUS (34; 35) experiments at HERA also found evidence for a hard Pomeron structure but, in addition, with a large gluonic component.

The HERA experiments proved that collinear factorization, which separates the perturbative and non-perturbative contributions, holds not only in inelastic DIS (Deep Inelastic Scattering) but also in diffractive DIS (12; 36). Within this framework the cross section for a hard process can be obtained as a convolution of the diffractive parton distribution functions (dPDF) of the proton and the cross section of the parton-parton interaction:

$$d\sigma = f_i^D(x, Q^2, x_{I\!P}, t) \otimes \sigma^i_{\text{hard}}(x, Q^2). \tag{8}$$

where x is the proton longitudinal momentum fraction carried by the parton i, Q^2 is the virtuality, $x_{I\!P}$ the proton momentum fraction loss and t is the squared four momentum transfer at the proton vertex.

The dependence of the dPDFs, $f_i^D(x, Q^2, x_{I\!P}, t)$, on the kinematic variables related to the proton vertex can be parametrised in terms of the exchange of the Pomeron and the universal parton densities:

$$f_i^D(x, Q^2, x_{I\!P}, t) = f_{I\!P/P}(x_{I\!P}, t) \cdot f_i(\beta = x/x_{I\!P}, Q^2). \tag{9}$$

The parton structure of the Pomeron is described by the parton distributions $f_i(\beta, Q^2)$, where β is the fraction of the Pomeron momentum carried by the interacting parton and Q^2 is the quark virtuality. The flux factor $f_{I\!P/P}(x_{I\!P}, t)$, describing the flux of

Figure 5 - Diffractive structure function measured by CDF compared with expectations based on dPDFs extracted by the H1 Collaboration.

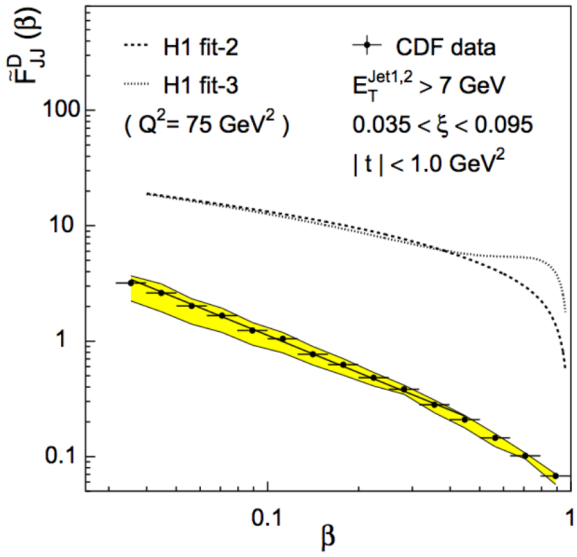

Legend: Diffractive structure function as a function of β. CDF data compared with expectations from the parton densities of the proton extracted from diffractive deep inelastic scattering by the H1 Collaboration at HERA.
Source: CDF COLLABORATION, 2001, p.45.

the Pomerons in the proton, can be extracted from hadron-hadron scattering, assuming universality of the Pomeron flux.

The dPDFs have been determined by the HERA experiments (7; 8; 9) by means of QCD fits to the inclusive diffractive DIS process ep $\rightarrow$ eXY, where X is a high-mass system and Y is the scattered proton or its low-mass excitation. dPDFs and their uncertainties were determined from a next-to-leading order QCD analysis of the Q^2 and β dependences of the cross section. The data used in the fits were selected using two methods: the requirement of a large rapidity gap between the final state proton and the rest of the hadronic system and by the detection of the final state proton in the leading proton spectrometers.

The results of diffractive processes studied by CDF at Tevatron (5) shows a suppression by a factor ~ 10 relative to predictions based on the dPDFs measured from HERA (see Fig. 5 (37)), indicating a breakdown of QCD factorization observed in soft diffraction processes. The measurement of the diffractive structure function F_{jj}^{pX} disagrees mainly in normalization. The suppression is attributed to additional soft partonic interactions which spoil the gap formed by the Pomeron exchange and also break the outgoing proton. The probability that the event with rapidity gaps survives the soft exchanges is called the soft survival probability factor $\langle S^2 \rangle$.

In the CDF experiment the suppression factor was determined by comparing the

Figure 6 - Ratio of diffractive to non-diffractive dijet event rates measured by CDF.

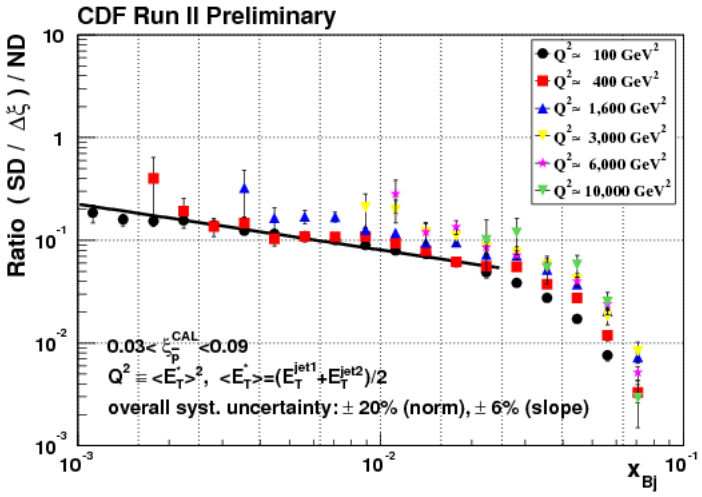

Legend: Ratio of diffractive to non-diffractive dijet event rates as a function of x_{Bj}, the momentum fraction of the parton in the antiproton, for different values of Q^2.
Source: CDF COLLABORATION, 2008, p.2.

rates of single-diffractive and inclusive events (see Fig. 6 (38)). The ratio $R(x,\xi,t)$ of single-diffractive and inclusive dijet cross sections, $\sigma_{\rm jj}^{\rm pX}(x,Q^2,\xi,t)$ and $\sigma_{\rm jj}(x,Q^2)$, is to leading order (LO) approximation proportional to the ratio of the corresponding structure functions, i.e:

$$R(x,\xi,t) = \frac{\sigma_{\rm jj}^{\rm pX}(x,Q^2,\xi,t)}{\sigma_{\rm jj}(x,Q^2)} \approx \frac{F_{\rm jj}^{\rm pX}(x,Q^2,\xi,t)}{F_{\rm jj}(x,Q^2)}. \tag{10}$$

It was found to a great extent independent of the details of the process (i.e. it does not depend on ξ, t, β, Q^2).

The factorization breaking was also observed in single-diffractive W, b-quark, J/ψ production and double diffractive production of events with a gap between jets (Jet+Gap+Jet). All processes yield similar single-diffractive to inclusive ratios $\sim 1\%$ and lead to the same factorization breaking.

The CDF experiment has also tested QCD factorization comparing the measurement of the diffractive structure function at $\sqrt{s} = 630$ GeV with the measurements obtained at $\sqrt{s} = 1800$ GeV (39). The ratio $R(x,\xi,t)$ of single-diffractive and inclusive dijet cross sections exhibit similar x dependence at the two energies, but the 630 GeV data lie systematically above the 1800 GeV data. Due to the large uncertainties no definitive conclusions can be drawn about the dependence in s of the factorization breakdown.

Recent results of hard diffraction in dijet production with a LRG at CMS show that the factorization breaking mechanism is not yet well modelled (18). To select diffractive events was imposed in the selection the requirements of pseudorapidity $\eta_{max} < 3$ ($\eta_{min} >$

Figure 7 - Results for diffractive dijet production at $\sqrt{s} = 7$ TeV.

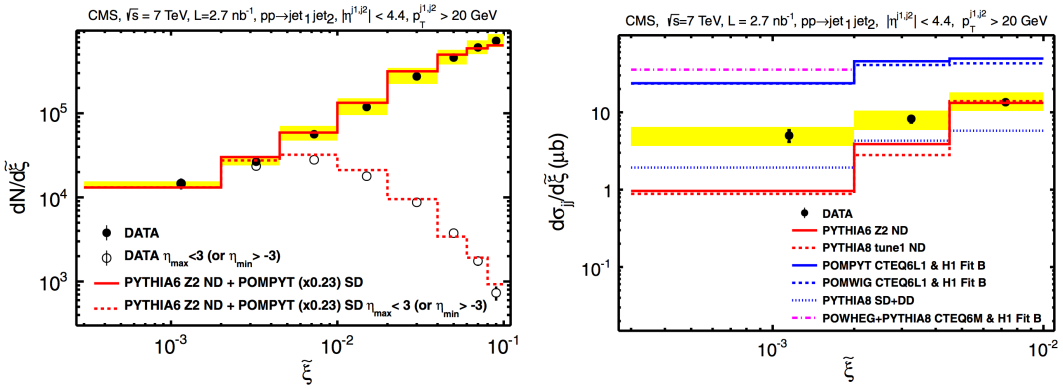

Legend: Left panel shows the reconstructed $\widetilde{\xi}$ distributions with (open symbols) and without (closed symbols) the $\eta_{max} < 3$ requirement, compared to Monte Carlo predictions. Right panel shows the differential cross section for inclusive dijet production as a function of $\widetilde{\xi}$ compared to Monte Carlo predictions.
Source: CMS COLLABORATION, 2013, p.7.

-3) for the objects measured from the calorimeters. Figure 7 shows the results for dijet production at $\sqrt{s} = 7$ TeV. The left panel shows the effect of the selection requiring a LRG on either side of the detector ($\eta_{max} < 3$ or $\eta_{min} > -3$). This selection rejects events with large values of $\widetilde{\xi}$, which corresponds approximately to the fractional momentum loss of the scattered proton in the diffractive process. The region at small values of $\widetilde{\xi}$ is not affected. The right panel shows the cross section as a function of $\widetilde{\xi}$. The low $\widetilde{\xi}$ bin shows a significant contribution from diffractive dijet production, observed for the first time at the LHC. The associated rapidity gap survival probability is estimated to be 0.08 ± 0.04 (NLO) to 0.12 ± 0.05 (LO).

2 THE CMS AND TOTEM EXPERIMENTS

This chapter introduces the LHC and present the general design of the CMS and TOTEM experiments, a more detailed description of the detectors can be found in Ref. (15) and Refs. (16; 17).

2.1 *The Large Hadron Collider* (LHC)

The LHC (40) is a two-ring superconducting accelerator and collider installed in the existing 26.7 km tunnel that was constructed between 1984 and 1989 for the *Large Electron Positron* (LEP). LHC can produce collisions with either protons or heavy ions. The protons are brought to a collision at four points along the LHC beam line. Surrounding two of these interaction points sit the general purpose detectors *Compact Muon Solenoid* (CMS) and *A Toroidal LHC Apparatus* (ATLAS) (Figure 8). These detectors are designed to record collisions at the highest instantaneous luminosity the LHC can supply, with design of 10^{34} cm^{-2}s^{-1}. The other interaction points are surrounded by the special purpose detectors *A Large Ion Collider Experiment* (ALICE) and *LHC beauty experiment* (LHCb) and are designed to have instantaneous luminosities of 2×10^{29} cm^{-2}s^{-1} and 10^{27} cm^{-2}s^{-1}, respectively.

At the LHC, the number of events per second generated in the collisions is proportional to the cross section $N = \sigma\mathcal{L}$, where $\mathcal{L}$ is the machine instantaneous luminosity, defined as the number of collisions per unit time and cross-sectional area of the beams:

$$\mathcal{L} = \frac{\gamma f k_B N_p^2}{4\pi\varepsilon_n\beta^*}F \tag{11}$$

where γ is the relativistic Lorentz factor, f is the revolution frequency, k_B is the number of bunches per beam, N_p is the number of particles per bunch, ε_n is the normalized transverse beam emittance (with a design value of 3.75 μm), β^* is the so-called betatron function at the IP, and F is the geometric luminosity reduction factor due to the crossing angle at the IP.

The LHC was designed to accelerate protons to an energy of 7 TeV and collide them at a center-of-mass energy of $\sqrt{s} = 14$ TeV, 2808 bunches per ring, and the time between two bunch crossings in the interaction point of 25 ns, which spaces the bunches about 7.5 m apart along the beam axis.

In the years 2010 and 2011 the LHC was operated with proton beam energies of 3.5 TeV. In 2012, the beam energy of 4 TeV was reached, resulting in a proton-proton center-of-mass energy of 8 TeV and a bunch spacing of 50 ns. This LHC running period

Figure 8 - The LHC experiments

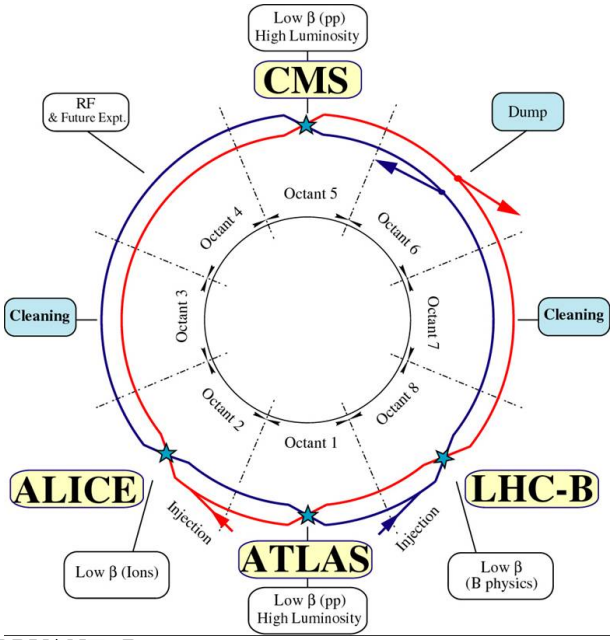

Source: EVANS, L. and BRYANT, P., 2008, p.8.

Table 1 - LHC parameters for proton-proton collisions during the period of 2012.

Parameter	**Variable**	**Value**
Proton energy	E	4 TeV
Number of particles/bunch	N_p	$1,15 \times 10^{11}$
Betatron value in the IP	β^*	0,6 m
Number of bunches	k_B	1380
Integrated luminosity	L	15 fb^{-1}
Bunch spacing	τ_b	50 ns

Source: LHC, 2012, p.1.

is called Run-1. In Spring 2013, the LHC was shut down for about 2 years to allow the consolidation and upgrade of numerous machine systems.

In July 2015 LHC started to collide proton beams with a center-of-mass energy of 13 TeV (LHC running period called Run-2). After a short period of 50 ns operation, the machine collected data with a bunch spacing of 25 ns.

This analysis is based on the data with pp collisions at $\sqrt{s} = 8$ TeV. Table 1 summarizes the conditions for this running period.

Figure 9 - CMS detector

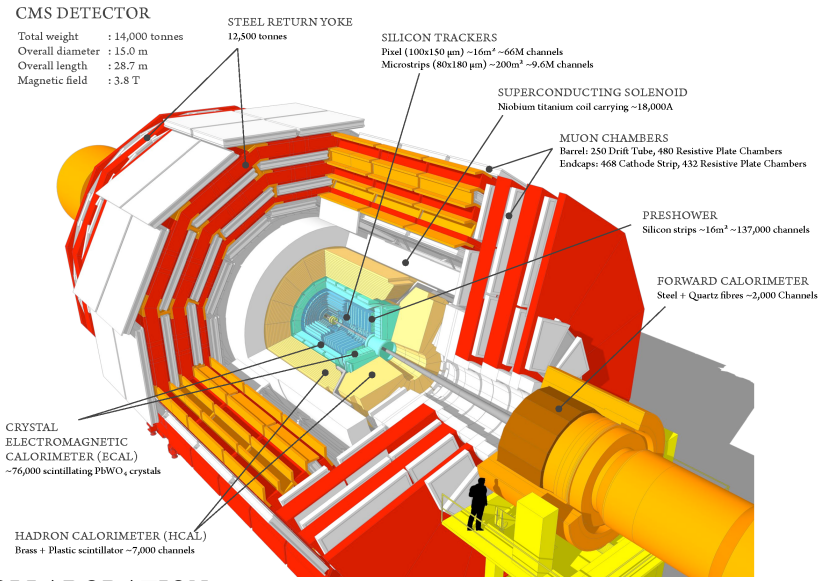

Source: CMS COLLABORATION, 2008, p.3.

2.2 **Compact Muon Solenoid**

The CMS detector is built around one of the interaction points (IP5) of the LHC. CMS was designed to be a general purpose detector that would have sensitivity to a wide range of physics. The central feature of CMS is a superconducting solenoid magnet with a 6 m diameter and 13 m length that provides a 3.8 T magnetic field. CMS has a cylindrical shape with an onion like design where inner subdetectors are nested inside of outer ones. From inside out, these subdetectors are an all silicon tracker, an electromagnetic calorimeter, a hadronic calorimenter, the magnet and the muon system.

CMS employs a right handed coordinate system with the x-axis pointing to the center of the LHC ring, the y-axis pointing vertically upward, and z-axis be along the beam line pointing in the counter-clockwise direction. The polar angle θ is defined relative to the z-axis. The pseudorapidity η is defined as $\eta = -ln\tan(\theta/2)$. The azimuthal angle ϕ is defined relative to the x-axis, meaning that vertically upward (downward) has a ϕ value of $\pi/2$ (-$\pi/2$).

2.2.1 Subdetectors

The innermost part of CMS is an all silicon tracker. Closest to the interaction point are pixel detectors with three barrel layers and two endcap disks, totaling 1,440 modules. Outside of this are strip detectors with ten barrel layers and twelve endcap disks. The tracker extends up to a pseudorapidity range of 2.5. Both the strips and the pixels have an

analog readout of the deposited charge with a maximum readout of roughly three times the charge expected to be deposited by a muon. Charge from particles traversing the inner tracker is expected to be spread out among multiple sensors in the same layer (of pixels or strips), allowing the position of the particle to be calculated more precisely than simply the center of the sensor. The charge sharing also allows the possibility to identify hits where two particles have overlapped.

Outside of the inner tracker is the calorimeter. The purpose of the calorimeter is to measure the energy of particles and aid in their identification by stopping particles at different points in the detector. The calorimeter is split into an inner electromagnetic calorimeter (ECAL) and an outer hadronic calorimeter (HCAL), each composed of a barrel and two endcap sections. The ECAL is made of 75,848 lead tungstate ($PbWO_4$) crystals split between the barrel and endcap. As particles lose energy in the ECAL the crystals emit scintillation light which is collected by photodetectors. In the barrel section of the ECAL, an energy resolution of about 1% is achieved for unconverted or late-converting photons in the tens of GeV energy range. The remaining barrel photons have a resolution of about 1.3% up to a pseudorapidity of $|\eta| = 1$, rising to about 2.5% at $|\eta| = 1.4$. In the endcaps, the resolution of unconverted or late-converting photons is about 2.5%, while the remaining endcap photons have a resolution between 3 and 4% (41). When combining information from the entire detector, including that from the tracker, the jet energy resolution amounts typically to 15% at 10 GeV, 8% at 100 GeV, and 4% at 1 TeV, to be compared to about 40%, 12%, and 5% obtained when the ECAL and HCAL calorimeters alone are used.

In the region $|\eta| < 1.74$, the HCAL cells have widths of 0.087 in pseudorapidity and 0.087 in azimuth (ϕ). In the η-ϕ plane, and for $|\eta| < 1.48$, the HCAL cells map on to 5×5 ECAL crystals arrays to form calorimeter towers projecting radially outwards from close to the nominal interaction point. At larger values of $|\eta|$, the size of the towers increases and the matching ECAL arrays contain fewer crystals. Within each tower, the energy deposits in ECAL and HCAL cells are summed to define the calorimeter tower energies, and subsequently used to provide the energies and directions of hadronic jets. Electrons and photons are likely to stop in the ECAL where they deposit all of their energies. Hadrons, electrically charged or neutral, will deposit some energy in the ECAL but will deposit most in the HCAL where they are very likely to come to a rest. High-momentum muons will deposit of the order of two GeV of energy in the calorimeter and are generally the only charged SM particles that are able to exit the calorimeter.

The HCAL is particularly important for the measurement of hadronic jets and neutrinos or exotic particles resulting in apparent missing transverse energy. Figure 10 shows the longitudinal view of the CMS detector. The Hadron calorimenter Barrel (HB) covers the pseudorapidity range $|\eta| < 1.3$ and consists of 36 azimutal wedged assembled intro two half-barrels (HB+ and HB-). The hadron calorimeter endcaps (HE) cover a

Figure 10 - Longitudinal view of the CMS detector.

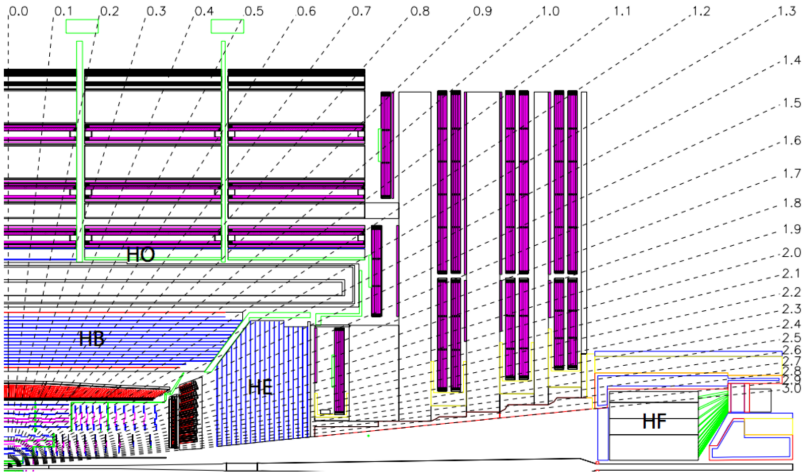

Legend: Figure shows the locations of the hadron barrel (HB), endcap (HE), outer (HO) and forward (HF) calorimenters.
Source: CMS COLLABORATION, 2008, p.123.

substantial portion of the rapidity range, $1.3 < |\eta| < 3$, a region containing about 34% fo the particles produced in the final state. The hadronic forward calorimeter (HF) extends the coverage $3.0 < |\eta| < 5.0$. Additional scintillators called outer calorimenter (HO) are located outside of the solenoid and act as tail catchers effectively increasing the thickness of the calorimenter in the central pseudo rapidity region.

The outermost part of the detector is the muon system which is split into three parts: Cathode Strip Chambers (CSC), Drift Tubes (DT), and Resistive Plate Chambers (RPC). The CSC cover the forward part of the detector with $|\eta| > 0.9$ while the DT and the RPC cover the barrel portion extending up to $|\eta|$ of 1.2 and 1.6, respectively. The muon system consists of four stations of chambers with the steel for the magnet return yoke located between the stations. The magnet return yoke provides a magnetic field in the muon system.

There are several subdetectors with coverage beyond $|\eta| = 5$. The forward instrumentation consists of the Hadronic Forward calorimeter (HF), the Centauro And STrange Object Research (CASTOR) and Zero Degree Calorimeter (ZDC) (Figure 11). The HF is located at a distance of 11.2 m on both sides of the interaction point (IP5) covering the pseudorapidity range $3 < |\eta| < 5$, the detector is designed to carry out the measurements of the forward energy flow and forward jets. The CASTOR detector is located at a distance of 14.4 m from IP5 and covers the pseudorapidity range $-6.6 < \eta < -5.2$. The ZDC detector consists of two calorimeters that are located at a distance of 140 m on both sides from the IP. The detector is designed to measure neutrons and very forward photons providing detection coverage in the pseudorapidity region of $|\eta| > 8.4$. A separate experiment TOTEM (Section 2.4) as well as the proton detectors CMS-TOTEM Preci-

Figure 11 - CMS forward subdetectors

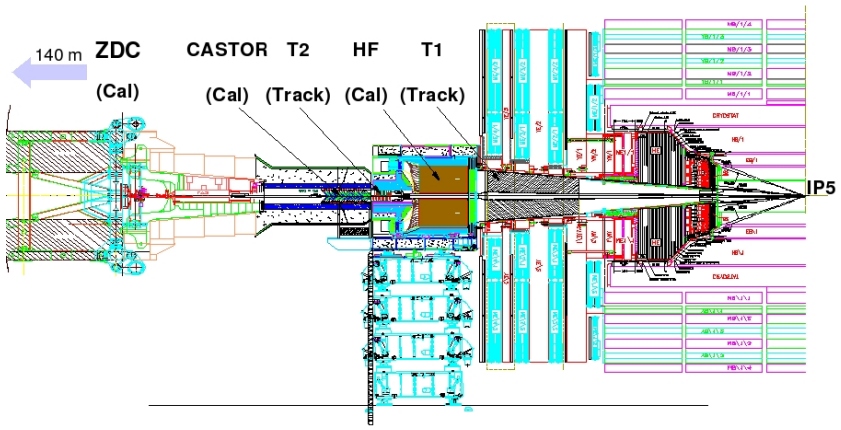

Source: CMS COLLABORATION, 2008, p.157.

sion Proton Spectrometer (CT-PPS) are additional forward detectors around the CMS interaction point. They further extend the forward reach available around IP5.

2.2.2 Trigger and computing

The rate of bunch crossings, or events, at CMS is too large for all of them to be readout and stored offline. To deal with this, CMS employs a two level trigger that selects interesting events online. The level one (L1) trigger must reduce the rate of events readout to less than 100 kHz in less than 4 μs requiring a completely electronics-based approach. Events are selected by a variety of algorithms but most of them look for a high momentum track in the muon system, large amount of energy in the ECAL or HCAL, or a combination of these. Multi-object triggers are specifically important for the isolation of new physics signals, that often result in complex final states that can be separated from some SM processes already at trigger level. Signals from these systems trigger the readout of data from the entire detector through the data acquisition system.

As the LHC was designed to operate with 25 ns bunch spacing, many of the subsystems, the tracker especially, only readout the data in the 25 ns window associated with the event. This means that triggers that *pre-fire* or *post-fire* will not contain much of the data from the event.

Once the data are readout by the data acquisition system after an L1 trigger, it is passed to a computing farm located above CMS. The next step in the trigger, the High Level Trigger (HLT), then runs on the computing farm. The HLT must reduce the number of events to a few hundred Hertz. The HLT is split into two different phases, Level 2 (L2), and Level 3 (L3). The L2 step is mostly concerned with confirming the L1 decision using more robust algorithms, the detector finest granularity, and reducing the

Figure 12 - L1 trigger in CMS

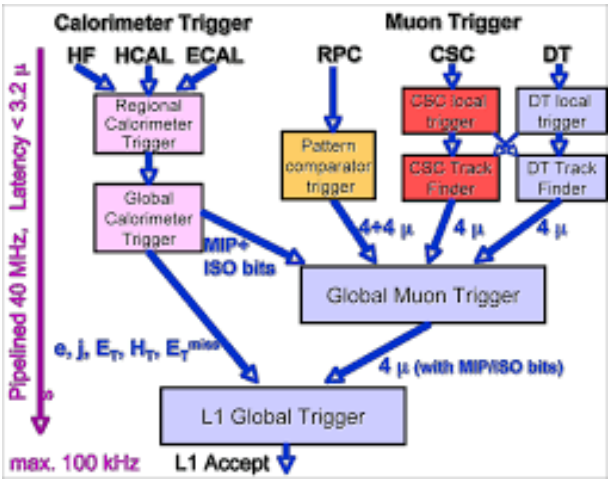

Source: CMS COLLABORATION, 2008, p.248.

rate so that a more complex reconstruction can be performed in the L3 step within the time restrictions. The L3 step reconstructs tracks in the inner silicon tracker and match them to objects in other parts of the detector, such as tracks found in the muon system or energy deposits in the electromagnetic calorimeter.

The CMS HLT, being composed of all the single-object triggers and the cross-object triggers, is characterized by a wide variety of different signatures that are searched for; if any are found, the data are passed to computers located at CERN and throughout the world for storage and further analysis. CMS maintains a software package, CMSSW, which is responsible for taking the raw data readout from CMS, and reconstructing what was happening in the event. This includes applying calibration constants, finding tracks, and identifying particles. The package includes the implementation of the HLT as well. After this reconstruction, the data size is at the scale of petabytes per second, which is too large for offline analyzers to run over frequently. To deal with this, skims of the data are produced, dropping lower level quantities and selecting only events that a particular analysis is interested in studying.

2.3 **Data Quality Monitoring (DQM) for physics analysis**

The CMS detector was built to make physics measurements using collision data collected from the LHC. To maintain high operation efficiency and reliable data certification, DQM has an important role within the CMS collaboration. Beginning at the CMS detector, some data are sent to the DQM tools and monitored by online shifters. All data are sent to the main computing facilities and processed there. Offline shifters monitor this data to detect any issues. The DQM system comprises:

- Tools for the creation, filling, transport and archival of histogram and scalar monitor elements, with standardized algorithms for performing automated quality and validity tests on distributions.
- Monitoring system live online of the detector, trigger, data acquisition hardware status and data throughput, offline reconstruction, and validating calibration results, software releases, and simulated data.
- Visualization of the monitoring results.
- Certification of datasets and subsets thereof for physics analysis.
- Retrieval of DQM quantities from the conditions database.
- Standardization and integration of DQM components in the CMS software;
- Organization and operation of activities, including shifts and tutorials.

The value of the DQM system is its ability to quickly and accurately identify problems.

2.3.1 Online and Offline DQM

There are two levels of the DQM framework: online and offline. Whereas the focus of the online system is more on detector performance, the offline DQM system is focused more on reconstruction.

The goal of the online DQM is mostly centered on discovering problems with detector hardware. The online DQM system is started by the central data acquisition system (DAQ) when the CMS is taking data and stopped when CMS is not. In this way, the DQM applications are an integral part of the data-taking process. The online DQM system consists of distributions that come from two different sources: the DQM applications directly and HLT filter units.

After events are fully processed and reconstructed through the CMS software, the increased statistics available offline may reveal subtle problems not found online, the reconstruction process may introduce errors, or both.

The DQM applications perform algorithms, called quality tests, that run checks on the data for known problems. The monitor element data are uploaded to a central DQM GUI web server for visualization in real time. Based on the results of the quality tests, there are alarms to warn people about problems. The tracking and bookkeeping of CMS data taking periods is managed via the Run Registry. The Run Registry is a database with a front-end web application; it serves as both a user interface and a persistent store of the information. Along with the DQM GUI, it is one of the major tools used by shifters to monitor and categorize the state of the detector at different times.

2.3.2 DQM shifts

In order to ensure that CMS is operating as efficiently as possible, there is always someone on shift for the DQM system when the CMS detector is collecting data. To monitor the online DQM at the site of the CMS detector, there are online shifts 24/7 during detector operation. The goal of the online DQM shifter is to quickly identify problems with detector performance or detector integrity during a run and notify the relevant expert to fix the problem immediately. In some cases, this may require stopping the data taking to ensure that the data are of high quality and optimal operation efficiency is achieved. The offline DQM shifter produces data certification for all relevant datasets, which include prompt reconstruction after the data was taken or subsequent iterations of re-reconstruction that may take place to improve alignment, calibration issues, and/or bug fixes. The DQM shifters of CMS are given four major tasks: (1) make sure all the DQM applications are working, as any application not visible in the GUI could indicate that the application may have crashed and needs to be restarted; (2) inspect all of the relevant histograms in the GUI, follow shift instructions, and contact an expert in case of problems; (3) provide bookkeeping of all relevant runs using the Run Registry; (4) produce a summary of shifts and report any issues. In case of persistent problems or issues outside the depth of the shifter's experience, they are to contact the DQM expert on call.

2.3.3 Service Work Activities

During my stay at CERN I took part in activities related to the CMS Collaboration. The activities performed in this period were:

- Shifts for the DQM online system during the Run-2.
- Coordination of the trigger strategy for the forward and small-x QCD physics group: preparation of the *menu* or list of specific paths with specific thresholds, for the low-pileup data taking in Run-2.
- Validation of FSQ triggers: validation and monitoring of the performance of each HLT path.

2.4 **TOTEM experiment**

The TOTEM (TOTal Cross Section, Elastic Scattering and Diffraction Dissociation Measurements at the LHC) experiment is composed of three different detectors

Figure 13 - TOTEM experiment

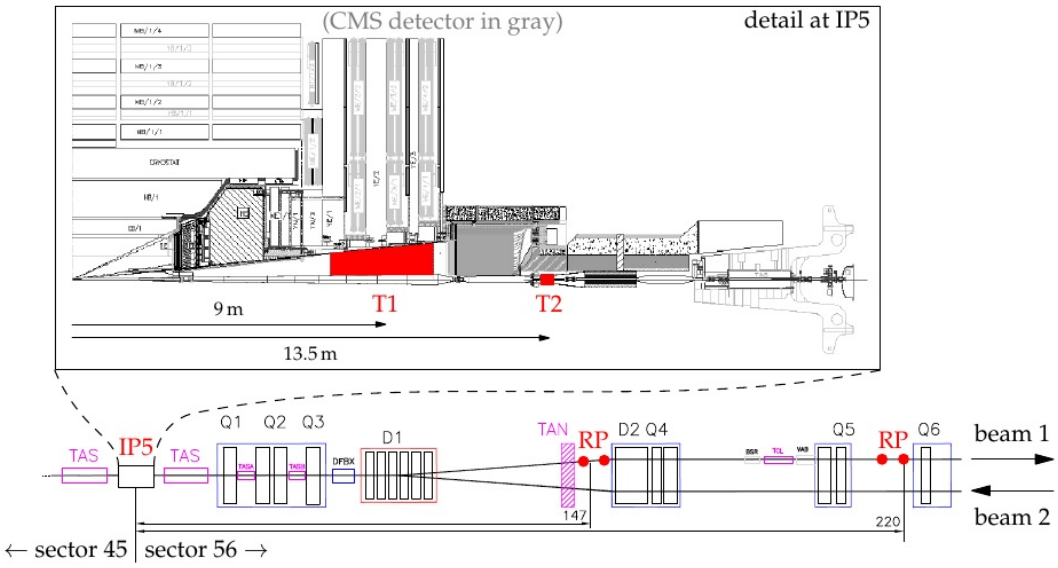

Source: TOTEM COLLABORATION, 2008, p.2.

located symmetrically on both sides of the interaction point (IP5). Figure 13 shows the experimental apparatus and its location partly embedded in the forward region of the CMS experiment: one arm of the T1 and T2 detectors, placed in front of the HF and CASTOR calorimeters of CMS respectively; the RP stations at about 147 m and 220 m.

2.4.1 The RP detector

The detection of the leading protons from diffractive and elastic interactions is performed by movable beam insertions called *Roman Pots* (RP). The Roman Pot is an experimental technique introduced at the ISR and successfully employed in later colliders like the $Sp\bar{p}S$, TeVatron, RHIC and DESY. The TOTEM silicon detectors are placed inside a secondary vacuum vessel, called "pot", and moved into the primary vacuum of the machine through vacuum bellows. In this way the detectors are physically separated from the primary vacuum which is so preserved against an uncontrolled out-gassing of the detector materials. Moreover, once a stable beam condition is reached, they can be moved very close to the beam, which allows to detect the protons at very small angles.

The RP system consists of four stations (placed at about ±140 and ±220 m from the IP), each one composed by two units, about 4 m distant. Each unit is composed by one RP approaching the beam horizontally and two RPs approaching the beam vertically from below or above. A schematic drawing of the beam pipe of a RP unit with its insertios is shown in Figure 14.

Figure 14 - The vacuum chambers of a RP unit accommodating the horizontal and the vertical pots and the Beam Position Monitor.

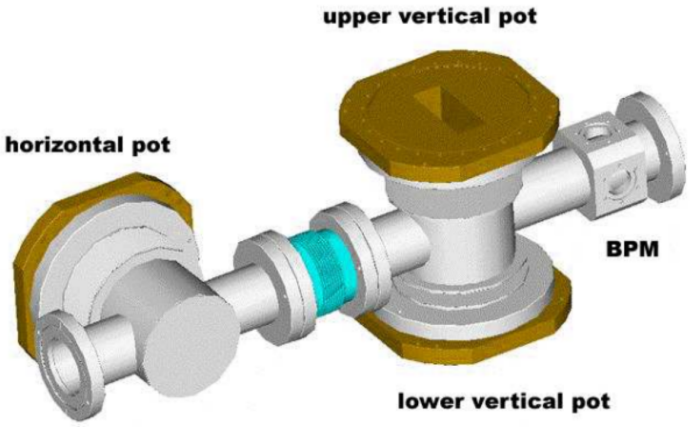

Source: TOTEM COLLABORATION, 2008, p.14.

The single horizontal pot in each unit, placed on the radially outer side of the LHC ring, server two purposes. Firstly, it completes the acceptance for diffractively scattered protons whose momentum loss deviates them towards this pot. On the radially inner side of the LHC ring no detector is needed since only background protons arrive in that position. Secondly, the detectors in the horizontal pots overlap with the ones in the vertical pots, which correlates their positions via common particle tracks (see Fig. 15). This feature is used for the relative alignment of the three pots in a unit. Each pot is equipped with a stack of 10 planes of silicon strip detectors. Half of them will have their strips oriented at an angle of $+45°$ with respect to the edge facing the beam, and the other half at an angle of $-45°$, measuring the coordinates u and ν respectively. This configuration has the advantage that the hit profiles in the two projections are equivalent and the measurement of each track projection in five planes is advantageous for the reduction of uncorrelated background.

The RP stations in the LHC sector 45 have positive z coordinates, while those in sector 56 have negative z coordinates according to the chosen coordinate system (Figure 16). In the following we will refer as sector 45 or sector 56 to locate TOTEM detectors sitting on the left side or right side of the IP respectively.

2.4.2 T1 and T2 detectors

T1 and T2 are dedicated to the measurement of the inelastic rate and are positioned to detect particles from almost all interactions. These detectors have to:

- provide a fully inclusive trigger for minimum bias and diffractive events;

Figure 15 - Overlap between the horizontal and vertical detectors.

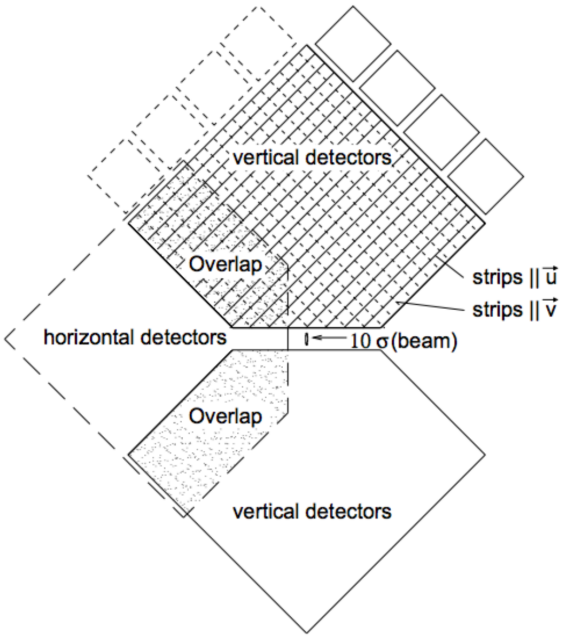

Source: TOTEM COLLABORATION, 2008, p.14.

Figure 16 - Location of the RP TOTEM stations.

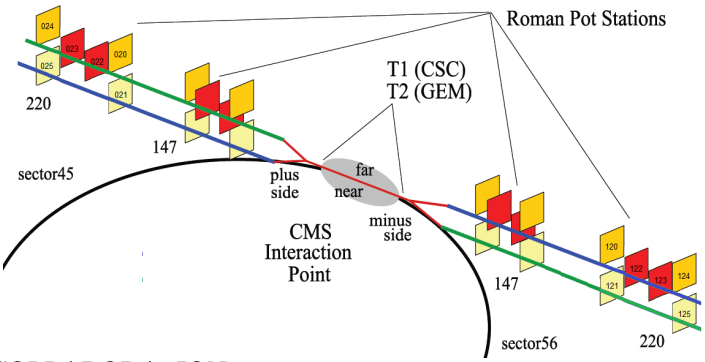

Source: TOTEM COLLABORATION, 2008, p.1.

- make possible to reconstruct the primary vertex of an event to reject tracks not crossing the interaction point (IP);
- be perfectly left-right symmetric with respect to the IP, in order to have a better control on the systematic uncertainties.

The T1 telescope is installed in the CMS endcaps region, at a distance of 7.5 to 10.5 m from the IP5. Each arm of T1, covers the pseudorapidity range $3.1 < |\eta| < 4.7$ (corresponding to a polar angle $18 < \theta < 90$ mrad) and is composed of five planes of Cathode Strip Chambers (CSC), equally spaced in z. T1 has to be able to provide a minimum bias trigger with a very high and well known efficiency and has to allow background (i.e. beam-beam or beam-beampipe) suppression after track reconstruction. These reasons led to the choice of CSC detectors, a widely used technology fast enough for TOTEM pourposes and lightweight enough to be positioned in front of the CMS forward calorimeters.

The T2 telescope, placed at about 14 m from the IP, detects charged particles produced in the pseudorapidity range $5.3 < |\eta| < 6.5$ (corresponding to a polar angular range $3 < \theta < 10$ mrad). One arm of the T2 telescope consists of 2 quarters, each composed by 10 triple-GEM (Gas Electron Multipliers) semicircular chambers. As for T1, T2 has to provide a fully inclusive trigger for inelastic (mainly diffractive) events. Moreover, even if T2 is further from the interaction point than T1, it has to allow track reconstruction with almost the same rejection power of T1 to discriminate background.

2.5 CMS/TOTEM combined acceptance

While the measurement of the total cross-section and elastic scattering can be performed using only TOTEM detectors, the integration of TOTEM and the general purpose CMS detector offers the prospect of more detailed studies of diffractive events. The TOTEM triggers, combining information from the inelastic detectors and the silicon detectors in the Roman Pots 220 m upstream, are incorporated into the general CMS trigger scheme, thus offering the ability to combine them with other CMS triggers. The digitization of the TOTEM detectors and the data acquisition system are both fully compatible with the CMS DAQ thus enabling a common read-out of both detectors, while still maintaining a stand-alone read-out for TOTEM.

The CMS experiment extended by the TOTEM detectors into the very forward region and the Roman Pot detectors along the LHC beam line is the largest acceptance detector, ever implemented at a hadron collider. The nearly complete acceptance for charged and neutral particles (except for a gap between T2 and the Roman Pots) of such a combined experiment is shown in Figure 17.

Figure 17 - The acceptance of a common CMS/TOTEM experiment in the azimuth-pseudorapidity plane.

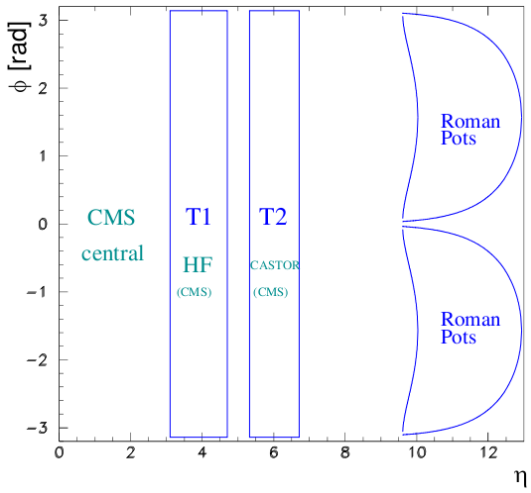

Source: TOTEM COLLABORATION, 2008, p.3.

Figure 18 shows the simulated pseudorapidity distributions of charged particles and of the energy flow at the LHC, demonstrating that with the common CMS/TOTEM acceptance almost all charged and neutral particles are detected as well as a fair fraction of the energy flow. The large coverage of such a "combined experiment" will allow for unique measurements that are also discussed in a common CMS/TOTEM physics group.

Figure 18 - The pseudorapidity distribution of charged particles and of the energy flow at $\sqrt{s} = 14$ TeV

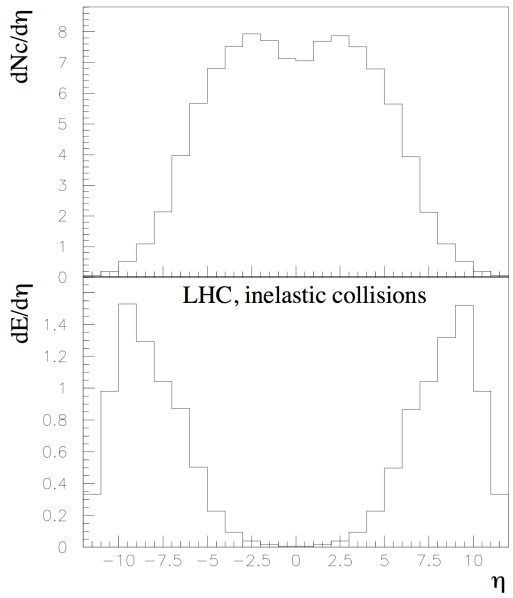

Source: TOTEM COLLABORATION, 2008, p.3.

3 MONTE CARLO SIMULATION

Monte Carlo (MC) event generators simulate high energy collision processes based on a procedure using random number generation and probability statistics, which implement diverse models and options of beam particles.

There are different choices of physics parameters in the MC generator. A set of parameters is called *tune*. In order to yield a reasonable comparison to data, the MC parameters are adjusted to describe the measurement. The tunes available differ in PDF sets or the underlying event (UE) parameters.

In this analysis several MC event generators are used. The simulation of inclusive dijet events was performed with PYTHIA6 (version 6.422) (42), PYTHIA8 (version 8.153) (43) and HERWIG6 (44). Diffractive dijet events were simulated with the POMWIG (45) and PYTHIA8. These models are briefly descibed below.

- **PYTHIA:** PYTHIA is a general purpose event generator. The hadronisation model used by PYTHIA is the Lund String model (46) and is common to the inclusive and single-diffractive models. PYTHIA has a prescription to model the UE using multiple parton iteractions (MPI). The UE and MPI framework is tuned using data.

  The UE was simulated in PYTHIA6 with tune Z2 (47), based on UE data measured with CDF at the Tevatron.

  PYTHIA8 is the successor of PYTHIA6 and employs an improved MPI model. This generator includes low and high mass soft diffraction in pp and $p\bar{p}$ collisions. It uses the Pomeron approach pioneered by Ingelman and Schlein (31), factorising the single-diffractive cross section into a Pomeron flux and a Pomeron PDF. The UE was simulated in PYTHIA8 with tunes 4C, CUETP8M1 and CUETP8S1 (48). The latter improved the UE tune including CDF and CMS data at different centre-of-mass energies. In the following this model is referred as the PYTHIA8 inclusive diffraction model.

  Additionally, PYTHIA8 version 8.223 implements a model to simulate hard diffractive events based on a direct application of diffractive parton distribution functions where it is possible to distinguish between two alternative scenarios. The first is based solely on the Pomeron flux and PDF. In the second an additional requirement is imposed: it does not allow any further MPIs to occur between the two incoming hadrons. Thereby the model introduces a dynamical rapidity gap survival probability that explicitly breaks factorization without introducing any new parameters (49). The former is referred as MPI-unchecked (*unsuppressed*) and the latter as MPI-checked (*suppressed*) hard diffraction. This model was generated with underlying event tune CUETP8M1 and it is referred as PYTHIA8 DYNAMIC GAP.

Table 2 - Cross sections for Pomeron and Reggeon exchange contributions in POMWIG in the kinematical region defined by $p_T > 40$ GeV, $|\eta| < 4.4$, $0.03 < |t| < 1.0$ GeV^2 and $\xi < 0.1$.

$\sigma_{\mathrm{p}\mathbb{P}}$:	256 nb
$\sigma_{\mathrm{p}\mathbb{R}}$:	31 nb

Source: The author, 2017.

- **HERWIG:** HERWIG6 is similar in fashion to PYTHIA but uses angular ordering in the generation of the parton shower and different hadronisation and MPI models.
- **POMWIG:** POMWIG implements Pomeron and Reggeon exchange in HERWIG6. It is based on the Ingelman-Schlein approach and considers the diffractive reaction as a two-step process: one proton exchanges a Pomeron with fractional momentum ξ and then the Pomeron interacts with the other proton. This generator combines Pomeron fluxes and diffractive PDFs, largely determined from HERA data, with the HERWIG6 event generator to produce complete hadronic final states.

All the simulations used diffractive parton distribution functions (dPDFs) from a fit to deep inelastic scattering data (H1 fit B (7)). POMWIG uses an NLO (Next-to-Leading Order) dPDF fit from Ref. (7) while PYTHIA8 uses a dPDF fit at LO (Leading Order). When using POMWIG a constant factor of 0.077 was applied to account for the effects of soft rescattering that leads to the suppression of the diffractive cross section, i.e. the rapidity gap survival probability. This value was chosen to give a good agreement with the data. Both Pomeron and Reggeon exchange contributions were simulated in POMWIG. Table 2 summarizes the values of the cross sections of both contributions, in the kinematical region requiring two jets with $p_T > 40$ GeV and $|\eta| < 4.4$, with $0.03 < |t| < 1.0$ GeV^2 and $\xi < 0.1$. The subleading Pomeron-Pomeron contribution corresponds to roughly 6.8 nb in this kinematical region. Events were generated with minimum hard scattering transverse momentum of 30 GeV, and maximum proton fractional momentum loss of 0.2, corresponding to cross sections of 5200 nb and 525 nb respectively for the Pomeron and Reggeon contributions. These values, as those in Table 2, do not include the correction due to the rapidity gap survival probability. Reggeon exchange is not simulated in PYTHIA8.

Figure 19 shows the single-diffractive dijet cross section as a function of t and ξ for events with at least two jets with $p_T > 40$ GeV simulated with POMWIG and PYTHIA8 DYNAMIC GAP. POMWIG is shown with no correction for the rapidity gap survival probability. PYTHIA8 DYNAMIC GAP is shown for two choices of the dPDF fit, at LO

Figure 19 - Diffractive dijet cross section as a function of t (left) and ξ (right) for events with at least two jets with $p_T > 40$ GeV.

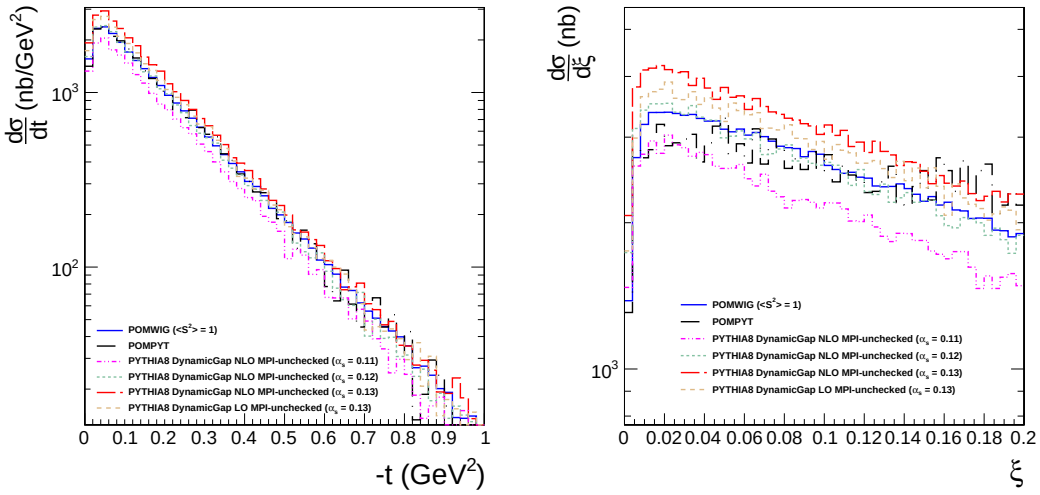

Legend: The plots compare the generated cross section obtained with POMWIG and PYTHIA8 DYNAMIC GAP (DG) MPI-unchecked. POMWIG is shown with no correction for the rapidity gap survival probability. PYTHIA8 DG is shown for different dPDF choices, at LO and NLO.
Source: The author, 2017.

and NLO, MPI-unchecked (unsuppressed). It is also presented with different values for the coupling constant α_s. The default generator setting ($\alpha_s = 0.13$) is used from now on.

Figure 20 shows the single-diffractive dijet cross section as a function of t and ξ for events with at least two jets with $p_T > 40$ GeV simulated with POMWIG and PYTHIA8. POMWIG is shown with a correction for the rapidity gap survival probability of 7.7%. PYTHIA8 is shown with the inclusive diffraction model and tunes 4C and CUETP8M1. The results from the PYTHIA8 DYNAMIC GAP model are also shown for two choices of the dPDF fit, at LO and NLO, MPI-checked.

All generated events were processed through the simulation of the CMS detector, based on GEANT4 (50), and reconstructed in the same manner as the data. The proton path from the interaction point to the TOTEM RPs was simulated by means of a parameterisation of the LHC optics (51). The acceptance and resolution of the TOTEM RP detectors were parameterised as a function of ξ and t using results of a dedicated simulation of the TOTEM apparatus (17); this is discussed in more detail in Sect. 3.1. All samples were generated without pileup.

Figures 21, 22 and 23 show the proton acceptance in $\log(\xi)$ vs $\log(|t|)$ simulated with POMWIG, PYTHIA8 4C and PYTHIA8 CUETP8M1, respectively. These figures show a common kinematically allowed region for t and ξ values, which are in agreement with TOTEM studies (52).

To further improve the description of the data, the diffractive generators were reweighted as a function of β, the fraction of the Pomeron momentum carried by the

Figure 20 - Diffractive dijet cross section as a function of t (left) and ξ (right) for events with at least two jets with $p_T > 40$ GeV.

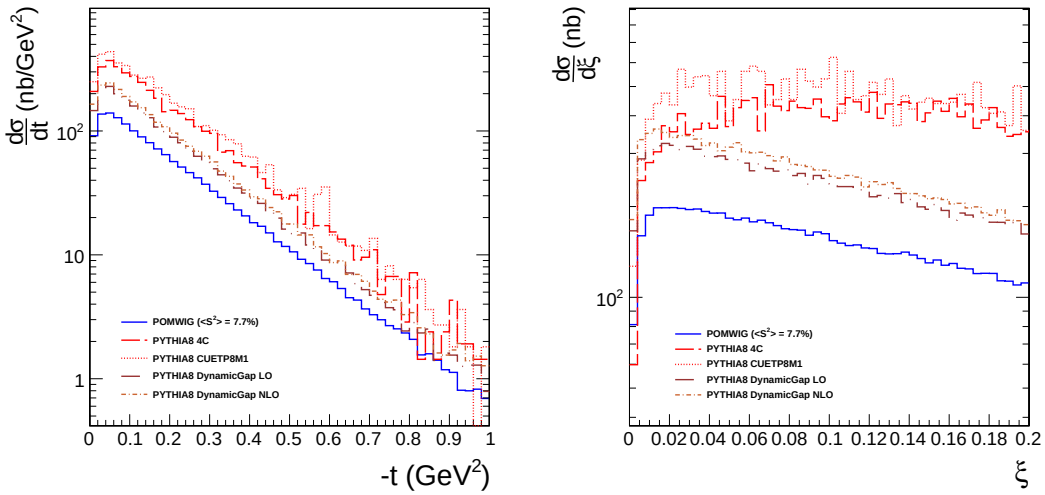

Legend: The plots compare the generated cross section obtained with POMWIG, PYTHIA8 4C, PYTHIA8 CUETP8M1 and PYTHIA8 DYNAMIC GAP (DG) MPI-checked. POMWIG is shown with a correction of $\langle S^2 \rangle = 7.7\%$ for the rapidity gap survival probability. PYTHIA8 DG is shown for two dPDF choices, at LO and NLO.
Source: The author, 2017.

Figure 21 - $\log(\xi)$ vs $\log(|t|)$ acceptance for sector 45 (left) and sector 56 (right) with POMWIG.

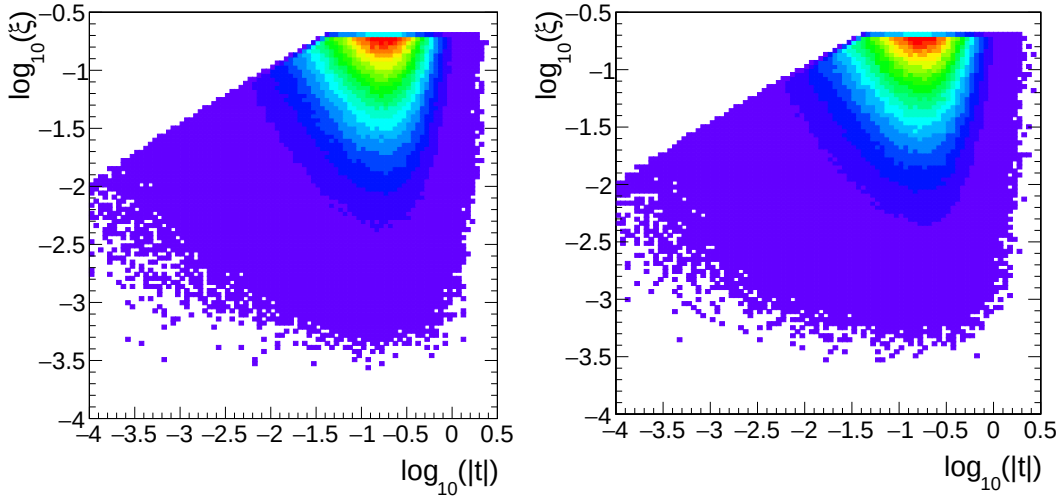

Source: The author, 2017.

Figure 22 - $\log(\xi)$ vs $\log(|t|)$ acceptance for sector 45 (left) and sector 56 (right) with PYTHIA8 4C.

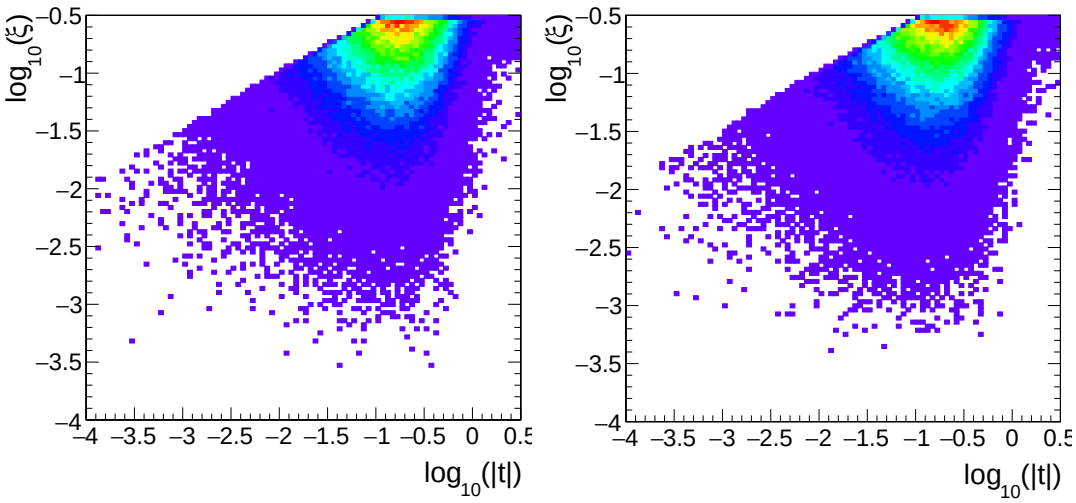

Source: The author, 2017.

Figure 23 - $\log(\xi)$ vs $\log(|t|)$ acceptance for sector 45 (left) and sector 56 (right) with PYTHIA8 CUETP8M1.

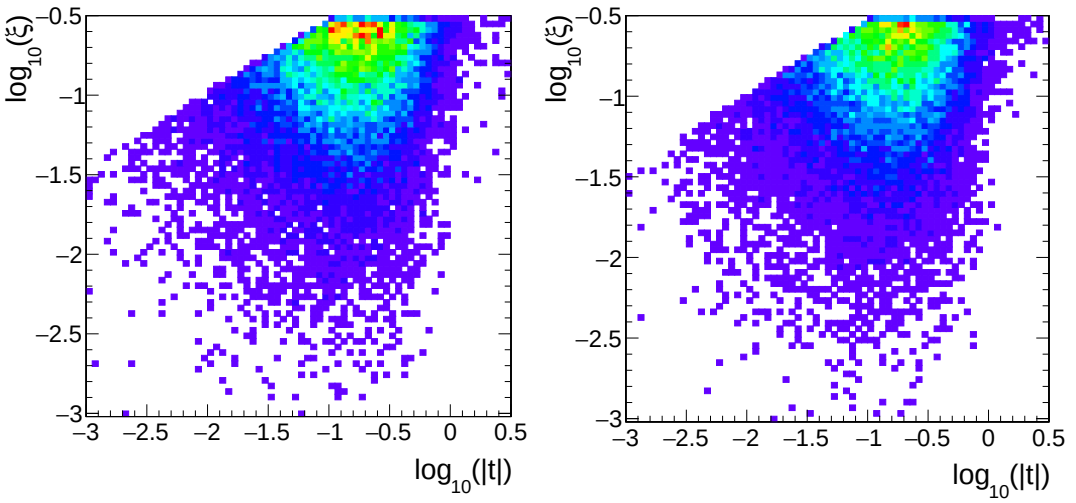

Source: The author, 2017.

Figure 24 - Ratio between data and POMWIG yields as a function of β, after all selection cuts; the MC includes the rapidity survival probability.

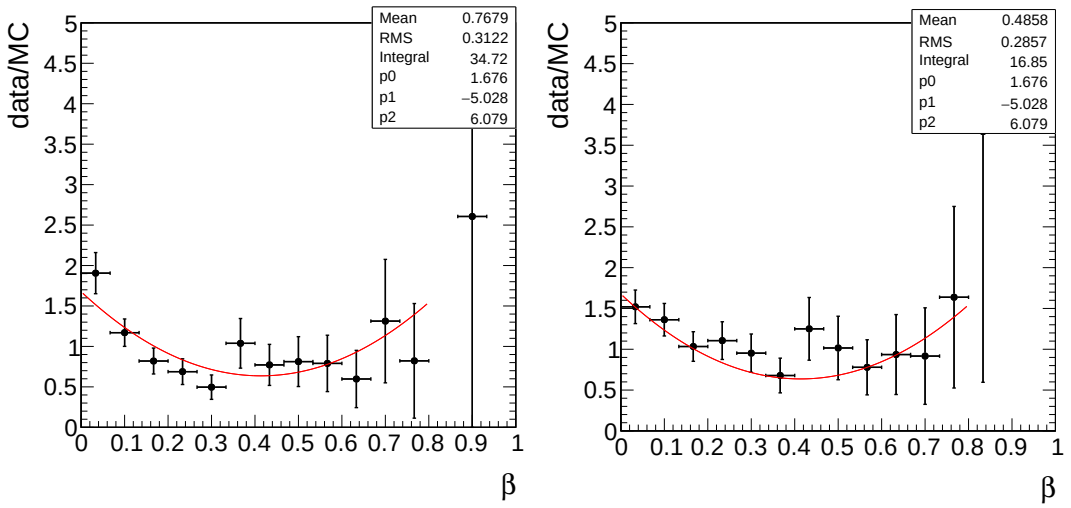

Legend: The left panel shows the results from the events in which the proton is detected in sector 45 and the right panel for the events with the proton in sector 56. The red line represents the result of a second-order polynomial fit to the points.
Source: The author, 2017.

interacting parton ($\beta = x/\xi$). Figure 24 shows the ratio between the data and POMWIG as a function of this variable; the fit to this distribution combined between the two sectors 45 and 56, indicated by the continuous line, was used to generate the weights; the same procedure was used with PYTHIA8.

As the beam spot is not correctly simulated as consistent with data (see Figure 25), a correction is also included in the MC as a weight, calculated as the ratio between the data and MC probabilities. Corrections to account for the trigger efficiency (see Fig. 36) and proton acceptance (Sect. 3.1) were also included in the MC.

3.1 **Roman Pot detectors acceptance and resolution**

In order to obtain a realistic simulation of the proton traversing the Roman Pot detectors, the folowing steps were performed:

- **Beam Smearing:** Most Monte Carlo generators assume that incident particles of nominal energy approach each other along the z axis and collide at the interaction point. This is not the actual situation. In reality there are two bunches colliding under a certain crossing angle. Within a bunch, particles do not have identical energy (energy smearing) and they are not all collinear (angular smearing). The bunches have non-zero dimensions and therefore the collision may take place at

Figure 25 - Distribution of the z primary vertex position.

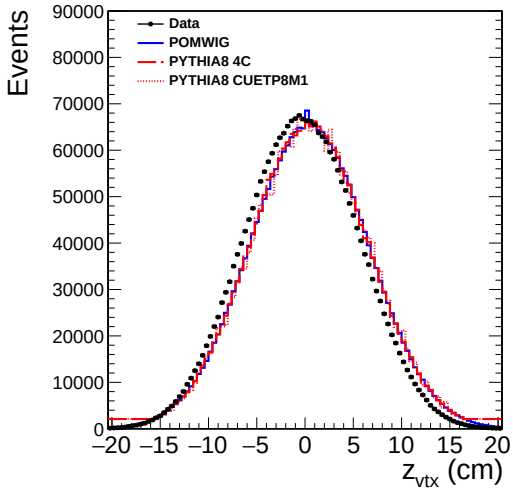

Legend: The data is compared with the diffractive MC, POMWIG and PYTHIA8.
Source: The author, 2017.

various points (vertex smearing).

The beam divergence can be determined by analysing the elastic scattering data, e.g. by the method detailed in Section 5.1.4 in (53). In the vertical plane, where detector resolution effects can be neglected, the beam divergence is derived from the variance of the difference between the scattering angles reconstructed in the left (sector 45) and the right (sector 56) arms. In the horizontal plane, where detector resolution effects are sizeable, a different approach is taken. The beam divergence, is derived from the variance of the horizontal vertex positions by scaling by the value of β^* (53):

$$\sigma(\theta_x^*) = \frac{\sigma(x^*)\sqrt{2}}{\beta^*}, \tag{12}$$

where $\sigma(x^*)$ is the standard deviation of reconstructed vertices.

The parameters applied to the Monte Carlo events to account for the beam smearing for $\beta^* = 90$ m are: $\sigma_{\theta_x} = 2.66$ μrad, $\sigma_{\theta_y} = 2.2$ μrad, $\sigma_\xi = 1 \times 10^{-4}$, $\sigma_{v_x} = 1.69 \times 10^{-4}$ m, $\sigma_{v_y} = 1.4 \times 10^{-4}$ m and $\sigma_{v_z} = 0.07$ m.

- **Proton Transport:** The acceptance of the RP system depends on the beam optics configuration and on the distance of the RPs from the beam. As mentioned earlier, the simulation of the TOTEM RPs acceptance was implemented in the diffractive MC by a parameterisation as a function of the kinematics of generator level protons, such as the vertex position, the scattering angles at the vertex (θ_x^* and θ_y^*), ξ and t.

- **Reconstruction of t and ξ:** The reconstructed distributions of t and ξ can be

obtained directly using a resolution function or indirectly from the scattering angles θ_x^* and θ_y^*. The parametrisations of the resolution in both cases were obtained based on an analysis of elastic and diffractive scattering data (17). They include real detector effects, optics and beam conditions. For the first case, t and ξ are smeared directly:

$$\xi_{rec} = \xi_{gen} + \sigma_\xi \qquad t_{rec} = t_{gen} + \sigma_t, \tag{13}$$

where

$$\begin{aligned} \sigma_\xi &= 0.00714986 - 0.0408903\ \xi_{gen} + 0.0965813\ \xi_{gen}^2 \\ \sigma_t &= 0.233365\ t_{gen} - 0.0975751\ t_{gen}^2 \end{aligned} \tag{14}$$

for sector 45 and

$$\begin{aligned} \sigma_\xi &= 0.00720615 - 0.0418783\ \xi_{gen} + 0.0999515\ \xi_{gen}^2 \\ \sigma_t &= 0.233365\ t_{gen} - 0.0975751\ t_{gen}^2 \end{aligned} \tag{15}$$

for sector 56.

Alternatively, the scattering angles θ_x^* and θ_y^*, calculated by:

$$\theta_x^* = \theta^* \cos(\phi^*) \qquad \theta_y^* = \theta^* \sin(\phi^*). \tag{16}$$

They were smeared by 25.10 μrad and 2.43 μrad respectively. The correlation between ξ and θ_x^* was taken into account (17) and the resulting value of ξ was calculated by:

$$\xi' = 324\Delta\theta_x + \xi \tag{17}$$

where $\Delta\theta_x = \theta_x' - \theta_x^*$ (θ_x' is the smeared scattering angle).

The t value is then calculated by $t' = |p_i - p_f'|^2$, where p_f' is the final four-momentum re-calculated with the smeared scattering angles, θ_x' and θ_y':

$$\begin{aligned} &\theta' = \sqrt{\theta_x'^2 + \theta_y'^2} \qquad \phi' = \arctan\left(\frac{\theta_y'}{\theta_x'}\right) \\ &p_z' = \pm(1-\xi')p_i \qquad p_T' = p_z' \tan(\theta') \qquad p_x' = p_T' \cos(\phi') \qquad p_y' = p_T' \sin(\phi') \end{aligned} \quad . \tag{18}$$

Figures 26 and 27 show the difference between these two smearing methods for events in sector 45 and 56 respectively. It is used as a systematic check.

Figure 26 - Distributions of t, ξ, θ_x^* and θ_y^* for the selected events in sector 45.

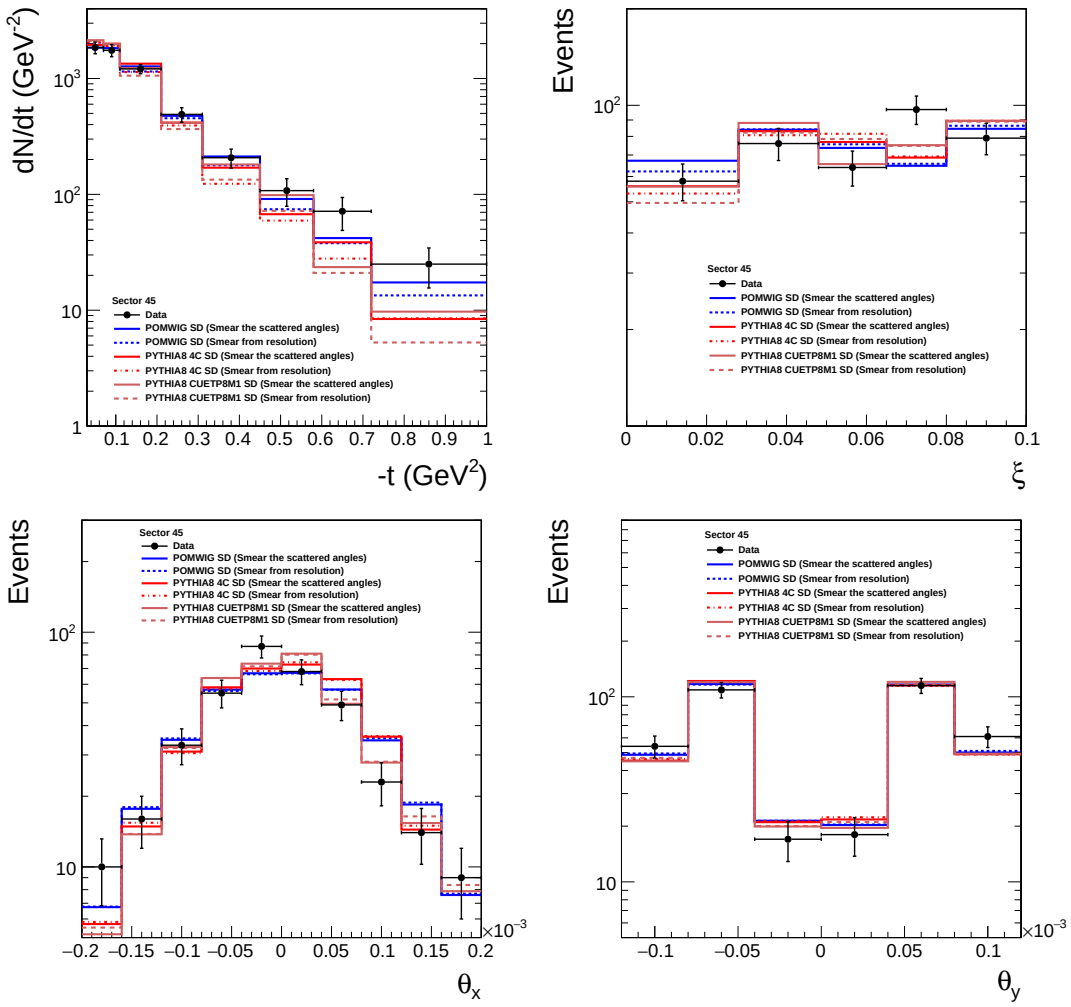

Legend: The figure also shows the distributions from POMWIG, PYTHIA8 4C and PYTHIA8 CUETP8M1. The solid lines indicate the variables reconstructed indirectly by smearing the scattering angles while the dashed ones indicate the distributions by the smearing the variables t and ξ. The distributions are normalised to the number of events in the data.

Source: The author, 2017.

Figure 27 - Distributions of t, ξ, θ_x^* and θ_y^* for the selected events in sector 56.

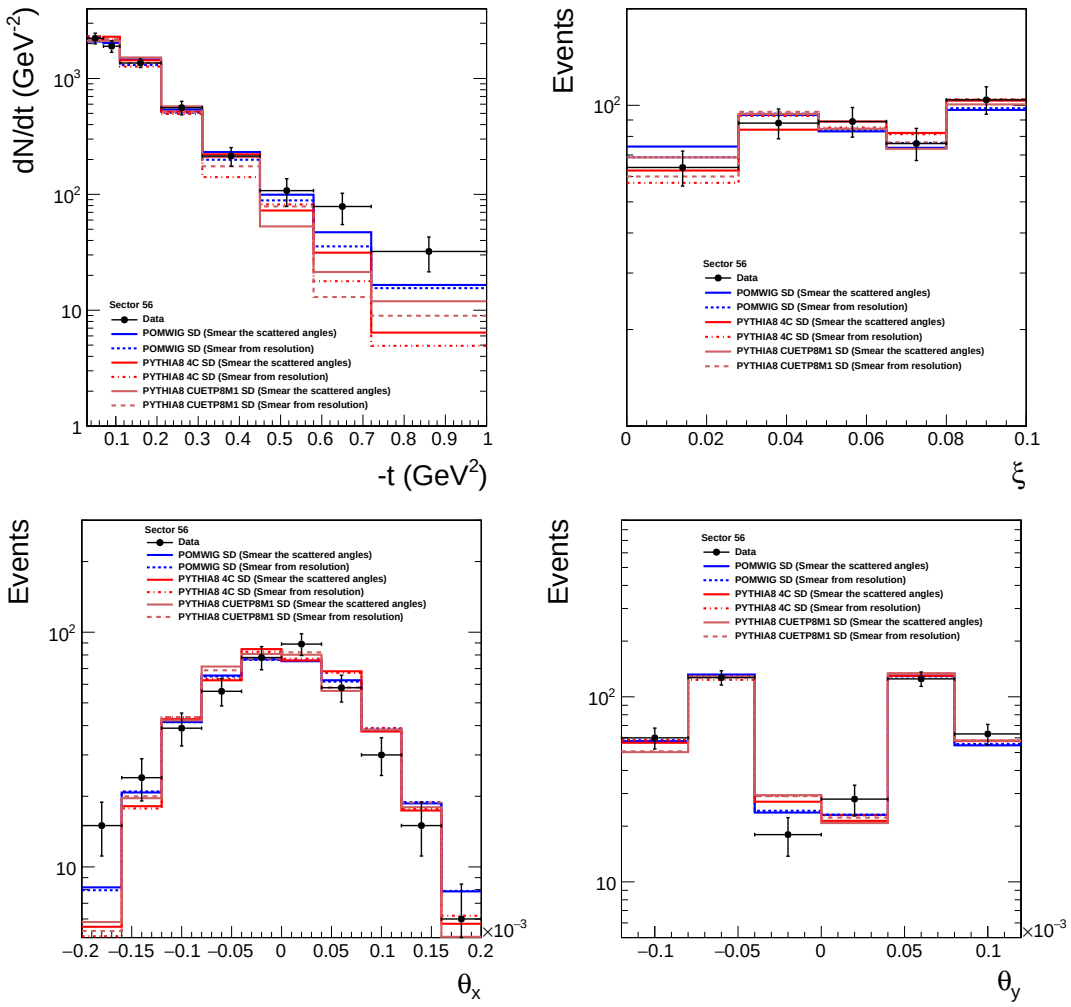

Legend: The figure also shows the distributions from POMWIG, PYTHIA8 4C and PYTHIA8 CUETP8M1. The solid lines indicate the variables reconstructed indirectly by smearing the scattering angles while the dashed ones indicate the distributions by the smearing the variables t and ξ. The distributions are normalised to the number of events in the data.

Source: The author, 2017.

Table 3 - Correction factors related to the proton reconstruction.

	Sector 45	**Sector 56**
top-top	1.060	1.067
bot-bot	1.063	1.0661

Legend: They are estimated for events with a proton traversing the two top (top-top) or two bottom (bottom-bottom) RPs on each side of the IP.
Source: TOTEM COLLABORATION, 2017, p.5.

The reconstructed distributions of t and ξ are strongly correlated due to the scattering angles, so the latter was taken as the nominal in the analysis.

- **Proton reconstruction inefficiency:** Track reconstruction may fail due to several reasons: intrinsic detection inefficiency of each silicon sensor, proton interaction with the material of the RP and the simultaneous presence of a beam-halo particle or "pileup" due to multiple interactions in the same bunch crossing. Moreover, detectors in the Roman Pot have the strips oriented in two directions and, while this allows for a good rejection of inclined background tracks, the possibility of identifying more than one proton track almost parallel to the beam direction is very limited (17). These uncorrelated inefficiencies of single RPs are evaluated directly from elastic scattering data (54). To account for the proton reconstruction inefficiency an extra normalisation factor is applied, corresponding to $\sim 6\%$ (see Tab. 3). The correction factors applied to the MC are defined by the inverse of the values shown in Tab. 3.

After applying all efficiency corrections, smearing effects and the proton parameterisation to the diffractive MC, a complete simulation of the single-diffractive production process is obtained. Figure 28 shows the hit positions of protons traversing the RPs with the above parameterisation.

Figure 29 shows the Roman Pot acceptance and selection efficiency as a function of t, ξ, θ_x^* and θ_y^* for events with a proton in sector 56, using the parametrisation described above. Fig. 29 also shows the results from an independent simulation of the RP detectors, based on GEANT4. In this case CMS detectors are not simulated. Figure 30 shows the ratio of the acceptances obtained with the parametrised procedure and with the RP detector simulation, as a function of θ_x^* and ξ. No selection is performed based on CMS information as it is not available in the latter. A discrepancy is observed at the low-ξ region. A correction is applied to the MC based on the values shown in Fig. 30. Figures 31 and 32 show the RP acceptance values after the correction is applied.

Figure 33 compares the RP acceptance separately for events with a proton traversing the two top RPs (top-top) and the two bottom RPs (bottom-bottom).

Figure 28 - Roman Pot hit position for MC events with a proton in the RP acceptance in sector 45 (left panel) and sector 56 (right panel).

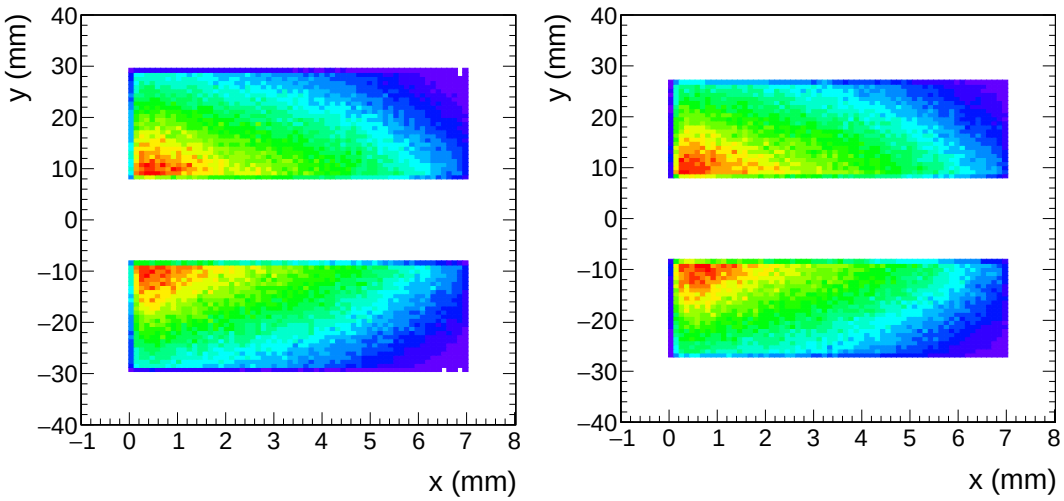

Source: The author, 2017.

Figure 29 - Roman Pot acceptance versus t, ξ, θ_x^* and θ_y^* for events with a proton in sector 56.

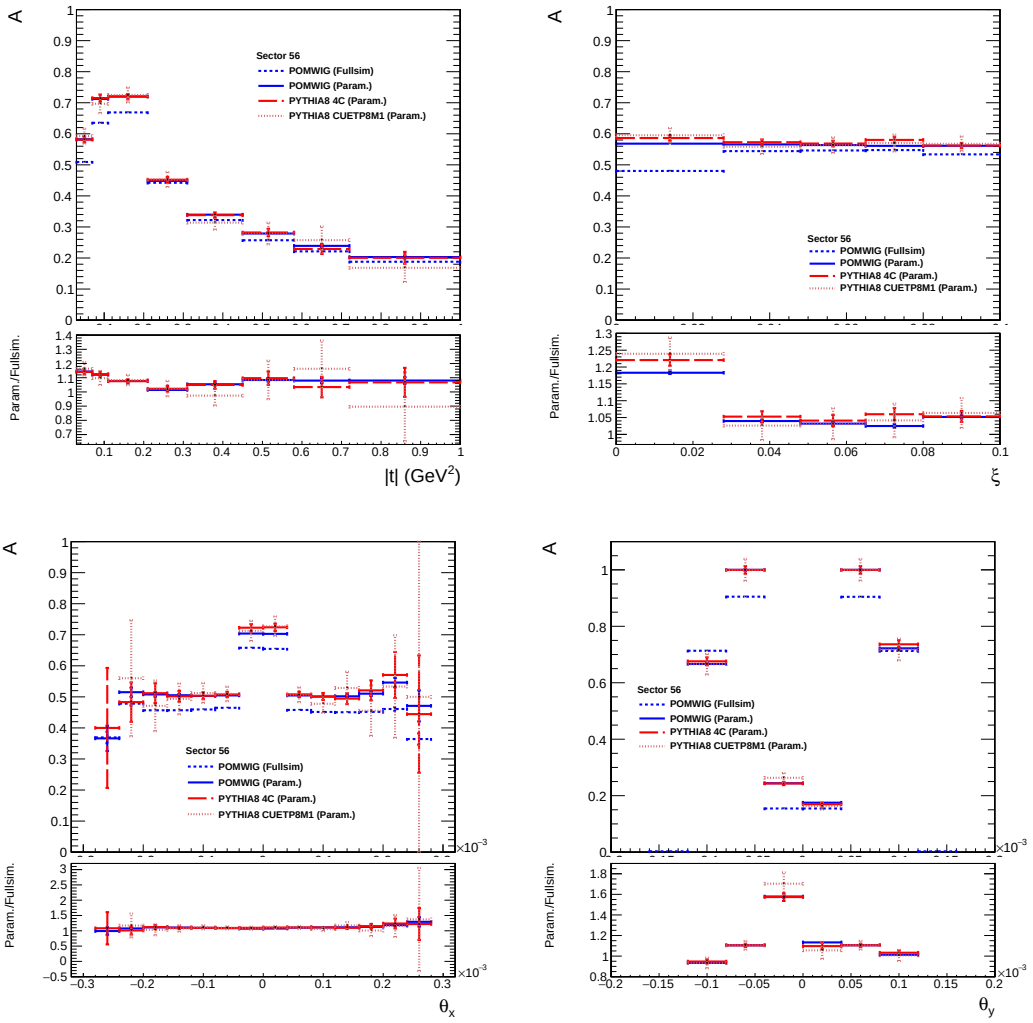

Legend: The parametrised simulation is shown with Pomwig, Pythia8 4C and Pythia8 Cuetp8m1. The distributions are compared to a simulation of the RP detectors performed with Pomwig, shown as the dashed-blue histogram.

Source: The author, 2017.

Figure 30 - Ratio of the RP acceptances using the parametrised simulation and the RP detector simulation as a function of θ_x^* and ξ.

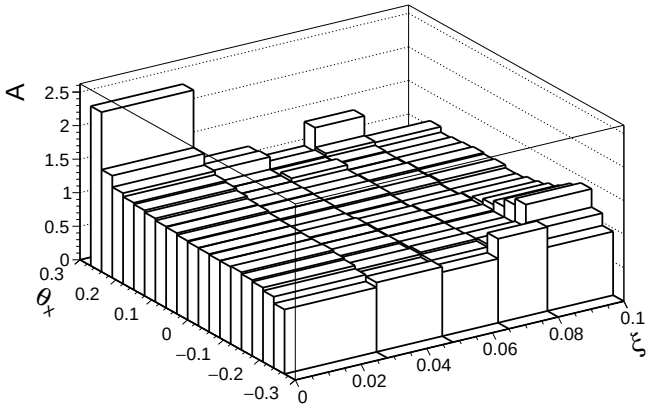

Source: The author, 2017.

Figure 31 - Roman Pot acceptance versus t, ξ, θ_x^* and θ_y^* for events with a proton in sector 56, after the correction described in the text.

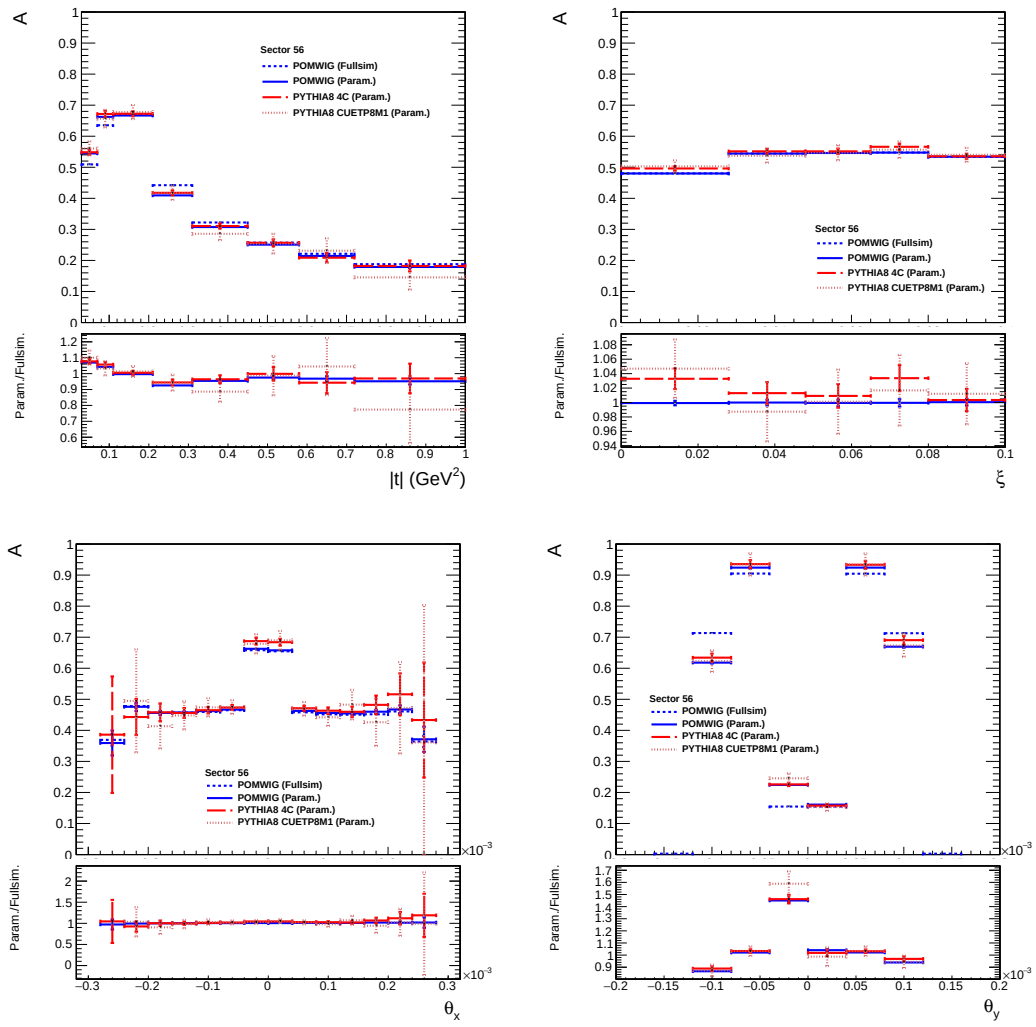

Legend: The parametrised simulation is shown with Pomwig, Pythia8 4C and Pythia8 Cuetp8m1. The distributions are compared to a simulation of the RP detectors performed with Pomwig, shown as the dashed-blue histogram.

Source: The author, 2017.

Figure 32 - Ratio of the RP acceptances using the parametrised simulation and the RP detector simulation as a function of θ_x^* and ξ, after the correction described in the text.

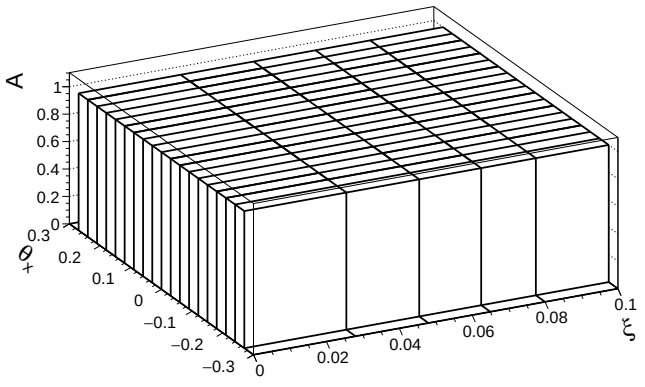

Source: The author, 2017.

Figure 33 - Roman Pot acceptance versus t, ξ, θ_x^* and θ_y^* for events with a proton traversing the top and bottom RPs, with the parametrised simulation and the full RP detector simulation.

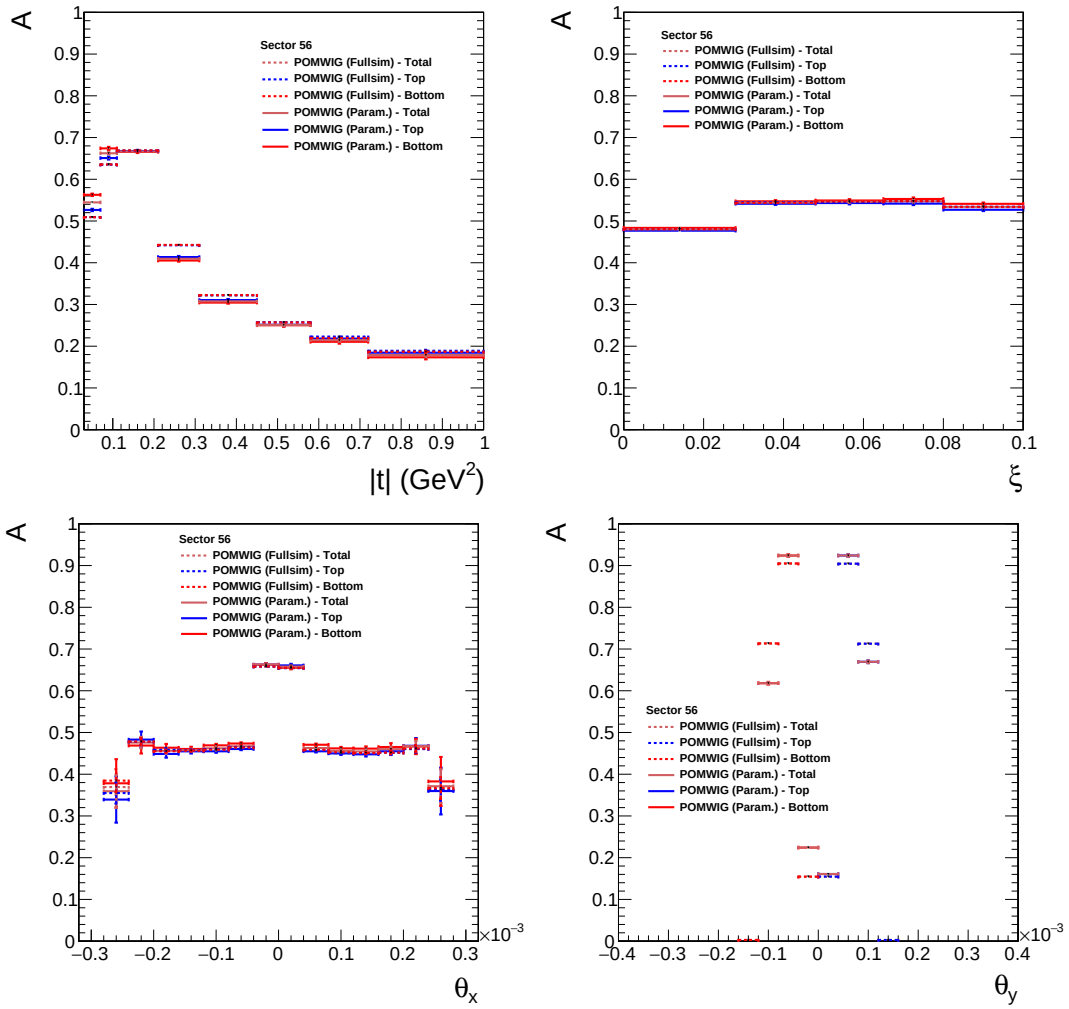

Source: The author, 2017.

4 DATA ANALYSIS

This thesis presents the first measurement of hard diffraction with a leading proton using the CMS and TOTEM detectors. Figure 34 shows a schematic diagram of the diffractive reaction pp $\rightarrow$ Xp with X including two high-p_T jets. Diffractive dijet production is characterised by the presence of a high momentum proton that escapes undetected by CMS and the system X, which contains high-p_T jets, separated from the proton by a large rapidity gap. Experimentally, the X system is measured with the CMS detectors, while the scatterred proton is measured using the RP detectors from TOTEM.

The proton is scattered at low angles, has low fractional momentum loss ξ, and low absolute value of the 4-momentum transfer squared t. It therefore does not leave the beam-pipe and can only be detected by using the TOTEM RP detectors. The latter make it possible to directly measure ξ (hereafter referred to as ξ_{TOTEM}), as well as $t = (p_i - p_f)^2$, where p_i and p_f are the four-momenta of the incoming and outgoing protons, respectively.

Conversely, if CMS-only information is used, as in Ref. (18), the fractional momentum loss can only be estimated from the energies and longitudinal momenta of the particles measured in CMS:

$$\xi^{\pm}_{\mathrm{CMS}} = \frac{\sum(E^i \pm p^i_z)}{\sqrt{s}}, \tag{19}$$

where the positive (negative) sign corresponds to the scattered proton moving towards the positive (negative) z direction. In this case, t cannot be measured.

This chapter presents the analysis for the measurement of the cross section as a function of t and ξ of the diffractive process shown in Figure 34. The ratio of the single-diffractive to inclusive dijet yields is presented as function of x, the momentum fraction of the parton initiating the hard scattering calculated as:

$$x^{\pm} = \frac{(E \pm p_z)^{Jet1} + (E \pm p_z)^{Jet2}}{\sqrt{s}} \tag{20}$$

where the positive (negative) sign refers to the incoming proton in the positive (negative) z direction.

4.1 Data Samples

The data were collected in July 2012 during a dedicated run with low probability ($\sim$ 4%) of overlapping pp interactions in the same bunch crossing (pileup) and a non-standard $\beta^* = 90$ m optics configuration, where β^* is the value of the amplitude function

Figure 34 - Schematic diagram of diffractive dijet production. The diagram shows an example of the gg→ jet jet process; the qq and gq initial states also contribute.

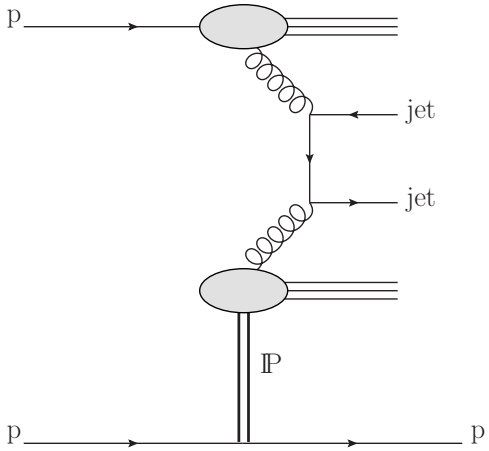

Source: The author, 2017.

of the beam at the interaction point.

These data correspond to an integrated luminosity of $\mathcal{L} = 37.5\ \mathrm{nb}^{-1}$ calculated by scaling the luminosity measured by CMS with that measured by TOTEM. The luminosity normalization is determined by requiring the same cross-section integral for elastic scattering events between $|t| = 0.027$ and $0.083\ \mathrm{GeV}^2$ as for data set 1 from (55), where the luminosity-independent calibration was applied, for exactly the same data taking period as for the dijet trigger data set.

The CMS orbit-counter reset signal delivered to the TOTEM electronics at the start of the run assures the time synchronisation of the two experiments. Events are combined offline by requiring that both the CMS and TOTEM reconstructed events have the same LHC orbit and bunch numbers. The number of merged events as a function of the lumi section is presented in Figure 35 for the two runs used in this analysis, 198902 and 198903. The merging efficiency, the fraction between merged events and those triggered with the CMS jet trigger, is found to be 87% and 91% for runs 198902 and 198903 respectively. The integrated luminosity is corrected for the time the CMS and TOTEM data acquisition systems were not collecting data simultaneously. The combined data samples used in the analysis are listed in Table 4.

To calculate the efficiency of the trigger used in this analysis (Section 4.2), the minimum-bias (events selected with a loose trigger intended to select inelastic collisions with as little bias as possible) combined sample was used, for which the details are given in Table 5.

In order to estimate the pileup and beam-halo background in the data, a zero-bias (events from randomly selected non-empty LHC bunch crossings) combined sample was used, as explained in Section 4.3. The details of the samples used are given in Table 6.

Figure 35 - Number of merged events as a function of the lumi section.

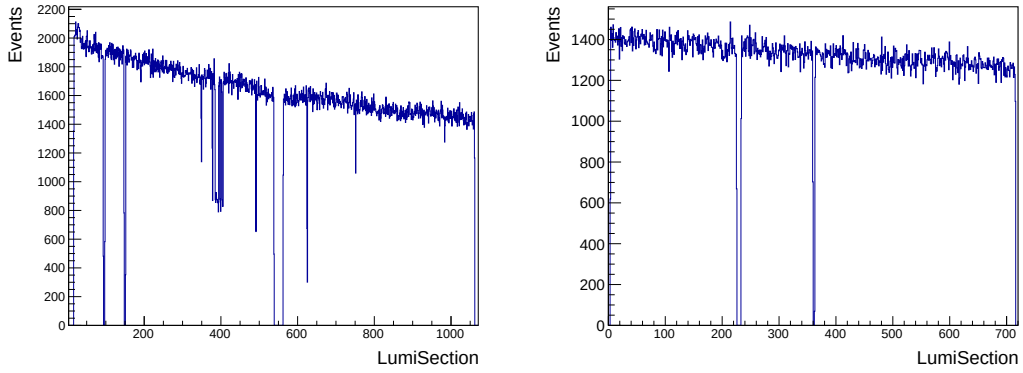

Legend: The left panel shows the number of events for run 198902 and the right panel for run 198903.
Source: The author, 2017.

Table 4 - Merged CMS+TOTEM samples for dijet events at 8 TeV.

TOTEM Run	**CMS Run**	**Sample**	**Number of Events**	**L** (nb^{-1})	**Eff**	**L*Eff** (nb^{-1})
8369/8371	198902	/LP_Jets1/Run2012C-22Jan2013-v1/RECO	814568	31.87	87%	27.73
8369/8371	198902	/LP_Jets2/Run2012C-22Jan2013-v1/RECO	815514			
8372	198903	/LP_Jets1/Run2012C-22Jan2013-v1/RECO	466934	17.40	91%	15.83
8372	198903	/LP_Jets2/Run2012C-22Jan2013-v1/RECO	466929			

Legend: The Table shows the run numbers for each experiment, the sample name, the number of events, luminosity and common data taken efficiency.
Source: The author, 2017.

Table 5 - Merged CMS+TOTEM samples for minimum-bias events at 8 TeV.

TOTEM Run	**CMS Run**	**Sample**	**Number of Events**
8369/8371	198902	/LP_MinBias1/Run2012C-22Jan2013-v1/RECO	5229241
8372	198903	/LP_MinBias1/Run2012C-22Jan2013-v1/RECO	4371295

Legend: The Table shows the run numbers for each experiment, the sample name and the number of events.
Source: The author, 2017.

Table 6 - Merged CMS+TOTEM samples for zero-bias events at 8 TeV.

TOTEM Run	**CMS Run**	**Sample**	**Number of Events**
8369/8371	198902	/LP_ZeroBias/Run2012C-22Jan2013-v1/RECO	2630208
8372	198903	/LP_ZeroBias/Run2012C-22Jan2013-v1/RECO	1796192

Legend: The Table shows the run numbers for each experiment, the sample name and the number of events.
Source: The author, 2017.

Figure 36 - Efficiency of the "HLT_L1DoubleJet20" trigger as a function of the transverse momentum of the second jet.

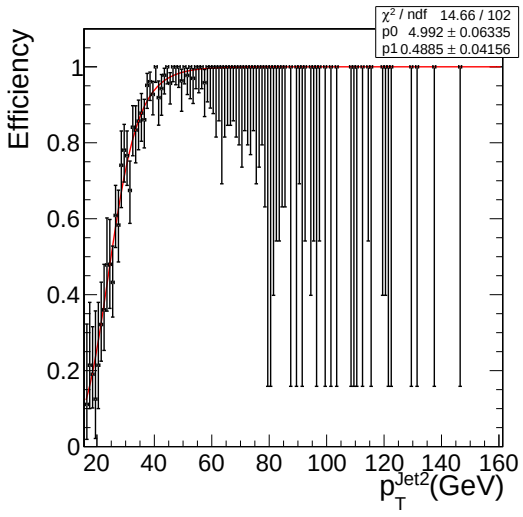

Legend: The red line represents the result of a fit to the data points.
Source: The author, 2017.

4.2 **Event selection**

At the trigger level, dijet events were selected by requiring at least two jets with $p_T > 20$ GeV. Only the hardware trigger level (L1) was used to select events simultaneously by CMS and TOTEM. The efficiency of the trigger was estimated by using events selected with a minimum-bias trigger and a leading jet with $p_T \geq 40$ GeV. The trigger efficiency, i.e. the fraction of events with at least two jet satisfying the "HLT_L1DoubleJet20" conditions is shown in Fig. 36 as a function of the second leading jet p_T. The efficiency is greater than 94% for $p_T > 40$ GeV. The fit to this distribution, indicated by the continuous line and Eq. 21, was used to obtain a correction factor to the Monte Carlo. The systematic uncertainty to account for the trigger efficiency is calculated as the maximum difference when varying the fit parameters as shown in Fig. 37.

$$f(p_T^{Jet2}) = \frac{1}{e^{\frac{p0-\sqrt{p_T^{Jet2}}}{p1}} + 1} \tag{21}$$

Offline, the selection required at least two jets with $p_T \geq 40$ GeV and $|\eta| < 4.4$. Jets were reconstructed with the anti-k_t inclusive jet finding algorithm (56) with a distance parameter of $R = 0.5$. The jet clustering algorithm was used to reconstruct jets from particle flow (PF) objects (57), which are particle candidates obtained by combining the information of the tracking system and of the calorimeters in an optimal way. The reconstructed jet energy was corrected by using the latest CMS Jet Energy Corrections

Figure 37 - Variation of the trigger efficiency fit parameters within uncertainties.

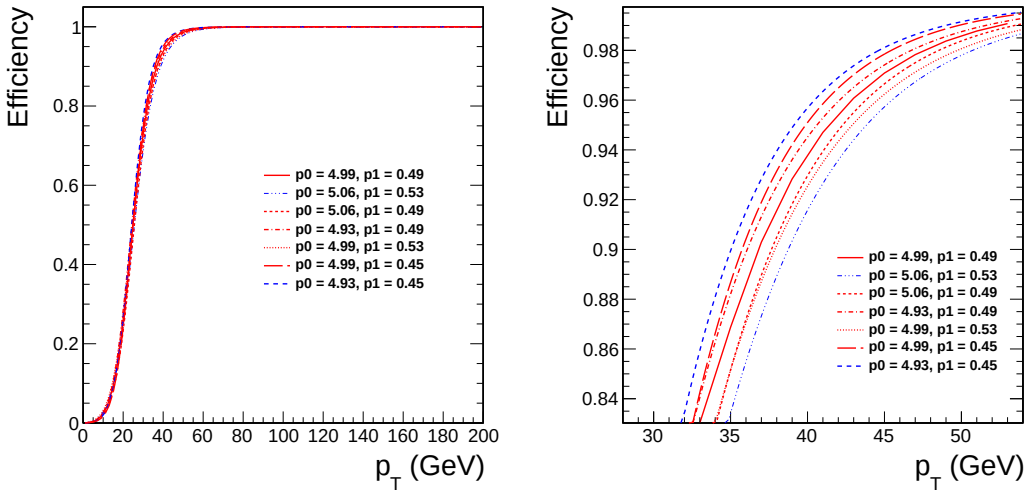

Legend: The figure at the right shows a close-up of the turn-on curve.
Source: The author, 2017.

(JEC) for the low-pileup period at 8 TeV (58).

In addition, the selection required at least one well reconstructed vertex with greater than four degrees of freedom in the vertex fit and a reconstructed proton track in the Roman Pot stations.

Events with protons in the RP stations in both sides are rejected if the kinematics is consistent with those from elastic scattering. Elastic scattering events, which are present in the data sample due to pileup, are identified by requiring two proton tracks in opposite directions, in a diagonal configuration: the protons traverse the two top RPs in sector 45 and the two bottom RPs in sector 56, or vice versa. In addition, the horizontal and vertical scattering angles of the two tracks are required to match within uncertainties. The horizontal scattering angle is reconstructed as $\theta_x^* = \dfrac{1}{dL_x/dz}\left(\dfrac{\Delta x_{\mathrm{RP}}^{\mathrm{F,N}}}{\Delta z_{\mathrm{RP}}^{\mathrm{F,N}}} - x^*\dfrac{dv_x}{dz}\right)$, where $x_{\mathrm{RP}}^{\mathrm{F,N}}$ are the horizontal track positions in the near and far RPs with respect to the IP and $z_{\mathrm{RP}}^{\mathrm{F,N}}$ are the RP positions; x^* is the reconstructed horizontal vertex position calculated as $x^* = x_{\mathrm{RP}}^{\mathrm{F}}/v_x$, where $v_x = -1.865760089$ and $\dfrac{dv_x}{dz} = 0.055513006\ \mathrm{m}^{-1}$. The horizontal scattering angles are required to match within five standard deviations, given by $\sigma\left(\Delta\theta_x^* \times dL_x/dz\right) \approx 4.89\ \mu$rad when the two tracks are detected in the two top RPs in sector 45 and the two bottom RPs in sector 56 and $\sigma\left(\Delta\theta_x^* \times dL_x/dz\right) \approx 5.69\ \mu$rad in the opposite diagonal. The vertical scattering angle in elastic scattering events is reconstructed as $\theta_y^* = \left(\dfrac{y_{\mathrm{RP}}^{\mathrm{F}}}{L_{y,\mathrm{F}}} + \dfrac{y_{\mathrm{RP}}^{\mathrm{N}}}{L_{y,\mathrm{N}}}\right)/2$ where $L_{y,\mathrm{F}} = 263.143819469$ m and $L_{y,\mathrm{N}} = 237.668241862$ m. The vertical scattering angles are required to match within five standard deviations, given by $\sigma\left(\Delta\theta_y^*\right) \approx 3.22\ \mu$rad. Finally, the horizontal vertex position values, reconstruted as $x^* = x_{\mathrm{RP}}^{\mathrm{F}}/v_x$ from the tracks detected on either side of the IP, are required to be within

Table 7 - Thresholds used for PF objects.

Object	η **Range**	**Threshold**
Gamma	Barrel	$E > 0.9$ GeV
	Endcap	$E > 2.5$ GeV
	Transition	$E > 2.5$ GeV
Neutral Hadron	Barrel	$E > 1.4$ GeV
	Endcap	$E > 2.7$ GeV
	Transition	$E > 3.8$ GeV
Gamma HF	Transition	$E > 3.5$ GeV
	Forward	$E > 3.5$ GeV
Hadron HF	Transition	$E > 4$ GeV
	Forward	$E > 4$ GeV

Source: The author, 2017.

five standard deviations of the vertex distributions, given by $\sigma(x^*) \approx 0.15 - 0.16$ mm. The applied cuts are similar to those described in Refs. (54; 59).

The reconstruction of ξ_{CMS} (Eq. 19) is estimated from the PF objects that passed threshold cuts listed in Table 7. The threshold values were found using zero-bias data. The details are given in Appendix A.

For signal events one expects $\xi_{\mathrm{CMS}} = \xi_{\mathrm{TOTEM}}$, but since the CMS detector has limited response as well as pseudorapidity coverage to $|\eta| < 5$, one has that $\xi_{\mathrm{CMS}} \leq \xi_{\mathrm{TOTEM}}$, and hence $\xi_{\mathrm{CMS}} - \xi_{\mathrm{TOTEM}} \leq 0$. This cut was also imposed in the selection to suppress the contribution of pileup and beam-halo events in which the proton is uncorrelated with the hadronic final state X measured in the CMS detector.

Proton track candidates were selected if the corresponding hit coordinates on the RP stations satisfy the following fiducial cuts: $0 < x < 7$ mm and $8.4 < |y| < 27$ mm, where x and y indicate the horizontal and vertical coordinates of the hit in the RP detectors with respect to the beam reference frame.

The reconstructed proton track was selected if it traverses the two top or the two bottom RPs on a given side. In addition, the kinematic cuts $0.03 < |t| < 1.0$ GeV^2 and $\xi_{\mathrm{TOTEM}} < 0.1$ were applied. Figure 38 shows the hit positions in each RP detector after the full event selection has been applied.

The RP alignment for the 8 TeV data set follows the standard three-step procedure (17): beam-based alignment prior to the run (as for LHC collimators) followed by two off-line methods. First, track-based alignment for relative positions among RPs, and second, alignment with elastic events for absolute position with respect to the beam. For more details see Section 5.1.2 in Ref. (54).

Table 8 shows the number os events passing each selection. The number of events with the proton in sector 45 (56) after all cuts is 374 (421).

Figure 39 shows the p_T and η of the jets and the distributions as a function of

Figure 38 - Roman Pot hit position in sector 45 (left panel) and sector 56 (right panel) for data events after all selection cuts.

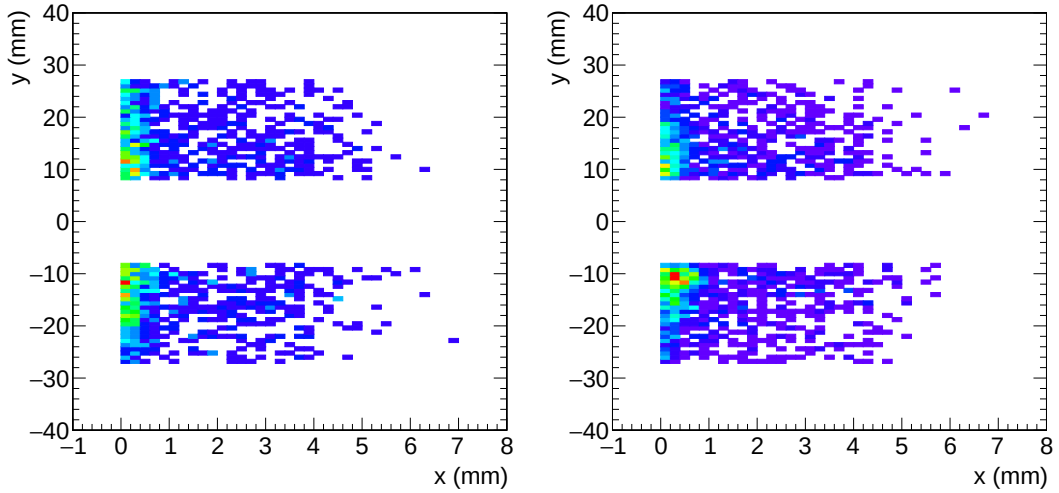

Source: The author, 2017.

Table 8 - Number of events after each selection.

Selection	**Sector 45**	**Sector 56**
Dijet ($p_T > 40$ GeV, $\|\eta\| < 4.4$)	429712	
Elastic scattering veto	407135	
Reconstructed proton	9580	
RP and fiducial cuts	2148	3052
$0.03 < \|t\| < 1.0$ GeV^2, $0 < \xi_{\text{TOTEM}} < 0.1$	1402	1815
$\xi_{\text{CMS}} - \xi_{\text{TOTEM}} \leq 0$	374	421

Source: The author, 2017.

x, the fraction of the proton momentum carried by the interacting parton, defined as in Eq. 20, with CMS-only information. The Monte Carlo predictions for inclusive dijet production are also shown, normalised to the number of events in the data.

Figures 40 and 41 show the p_T and η distributions of the jets, as well the distributions of x, t, ξ, β, θ_x^* and θ_y^* for the selected events in which the proton is detected in sector 45 and 56.

The mass of the system X defined as $M_X = \sqrt{s\xi}$, and the dijet invariant mass, M_{jj}, are shown in Figures 42 and 43. The dijet mass fraction $R_{jj} = M_{jj}/M_X$ is also shown.

4.3 Background

The relevant background in this analysis is that due to the overlap of a proton-proton collision and additional beam-halo particles measured at the RP stations (particles around the beam core that are distant enough from the beam axis to hit the RPs), or alternatively outgoing protons from additional pileup interactions in the same bunch crossing.

As mentioned earlier, pileup events were not simulated in the MC, but they are included in the data sample. Two different methods have been developed yielding consistent results. They are explained in the following.

1. **Zero-Bias method:**

   In this case the zero-bias data sample is used (Table 6), mixed with the diffractive and non-diffractive MC to describe the background events. To provide an estimate of the beam-halo and soft pileup backgrounds, from this sample, events were selected without the requirement of a vertex. Such events are denoted by ZB in the following.

   Two methods were used. They differ in the way the data is mixed with the MC. In the first method, each MC event (both POMWIG and PYTHIA6) was associated to an event taken randomly from the full ZB sample, which may or may not contain a proton measured in the RP detectors. Around 1k ZB events with a proton are mixed to the MC. The results using this method are shown in Appendix D.

   In order to improve the effective statistics in the method, a sub-sample is chosen from the full ZB data sample containing only events with a proton. Following the same procedure described before each MC event was associated to an event taken randomly from the ZB sub-sample, which always has a proton. In this case around 1M ZB events with a proton are effectively mixed to the MC. Consistent results are obtained with a better resolution due to the increased statistics.

Figure 39 - Distributions of jet p_T, η and x for events before the diffractive selection.

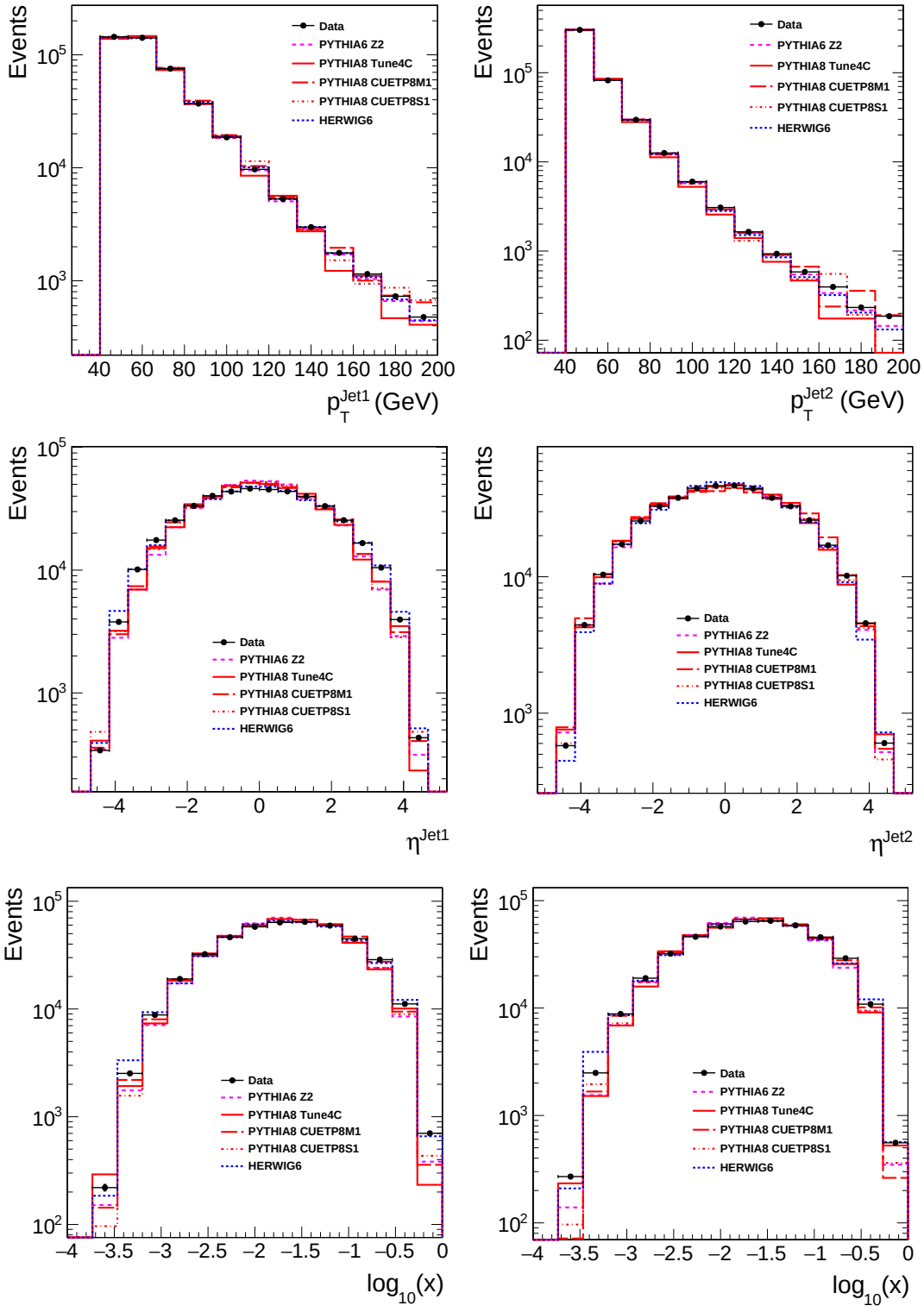

Legend: The HERWIG6, PYTHIA6 and PYTHIA8 Monte Carlo are also shown, normalised to the number of events in the data.
Source: The author, 2017.

Figure 40 - Distributions of jet p_T, η, $\Delta\eta$ and $\Delta\phi$, as well as x, θ_x^*, θ_y^*, t, ξ and β for the selected events in which the proton is detected in sector 45.

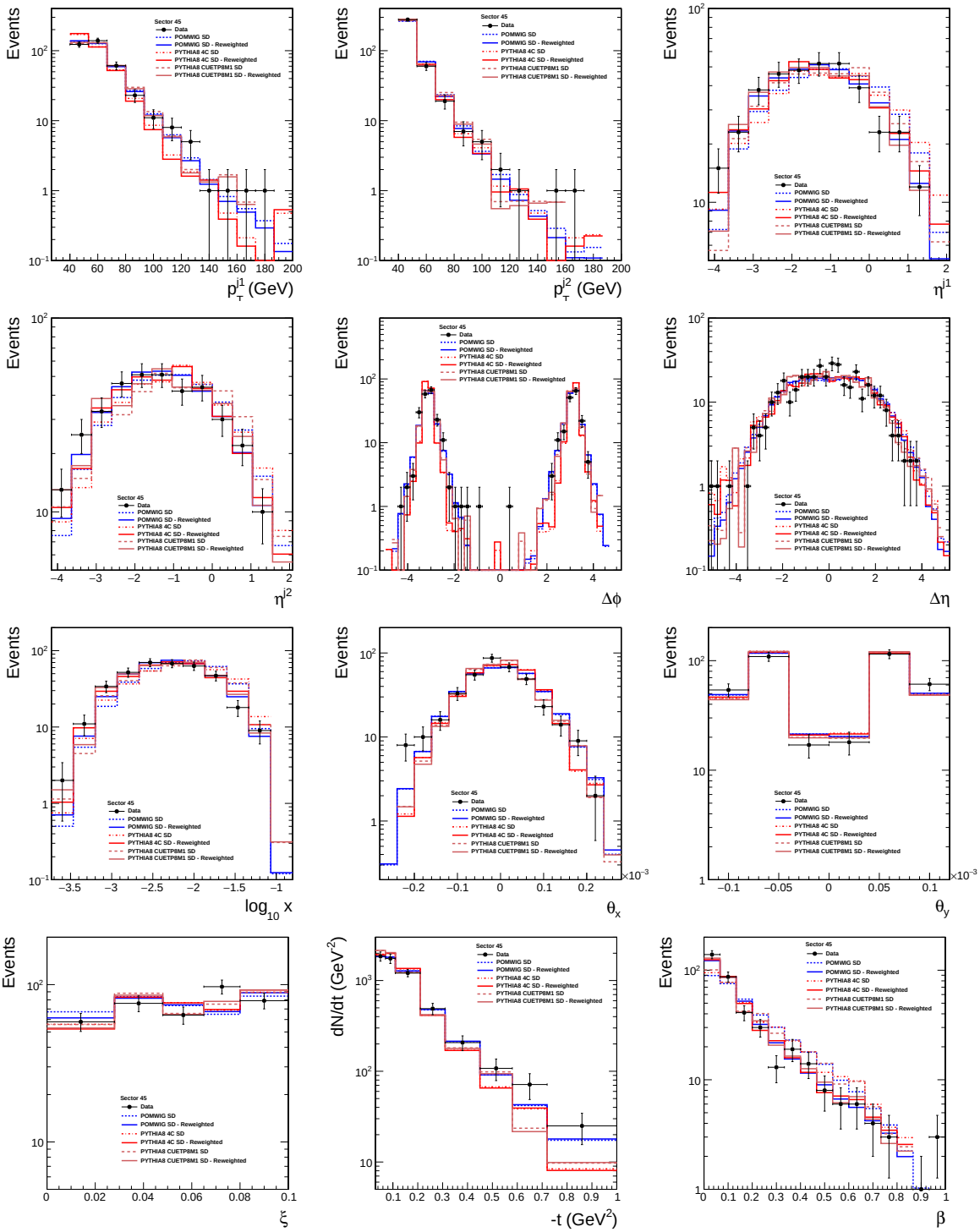

Legend: The solid lines show the effect of the correction factors applied to POMWIG and PYTHIA8. The Monte Carlo is normalised to the number of events in the data.

Source: The author, 2017.

Figure 41 - Distributions of jet p_T, η, $\Delta\eta$ and $\Delta\phi$, as well as x, θ_x^*, θ_y^*, t, ξ and β for the selected events in which the proton is detected in sector 56.

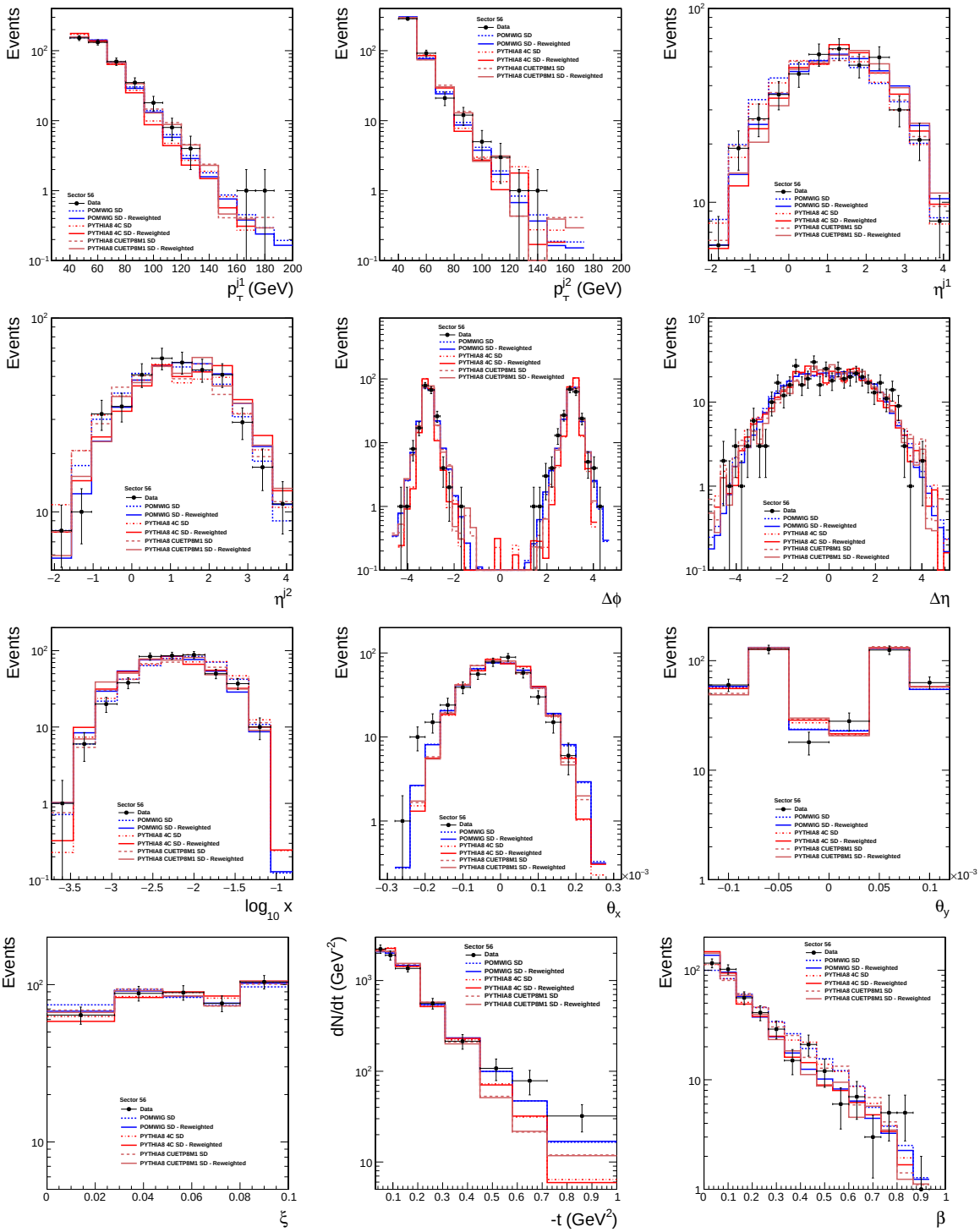

Legend: The solid lines show the effect of the correction factors applied to POMWIG and PYTHIA8. The Monte Carlo is normalised to the number of events in the data.

Source: The author, 2017.

Figure 42 - Distributions of the dijet invariant mass M_{jj}, mass of the system X, M_X, and the dijet mass fraction R_{jj}, for the selected events with the proton detected in sector 45.

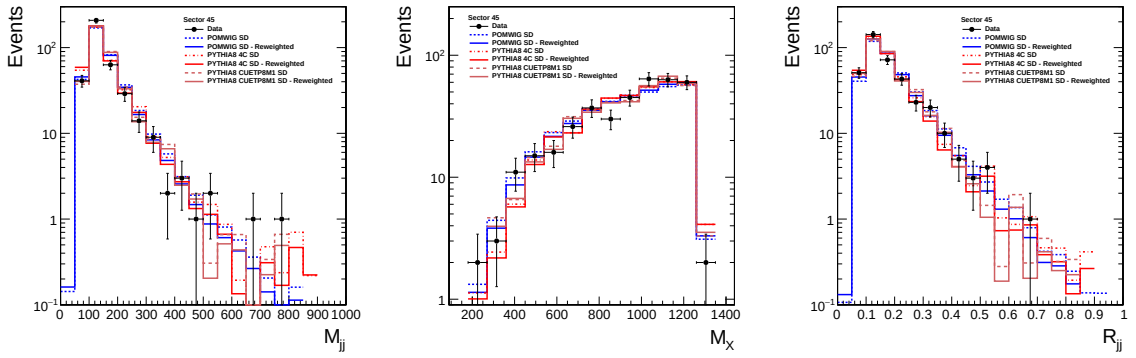

Legend: The solid lines show the distributions with the correction factors applied to POMWIG, PYTHIA8 4C and PYTHIA8 CUETP8M1. The Monte Carlo distributions are normalised to the number of events in the data.
Source: The author, 2017.

Figure 43 - Distributions of the dijet invariant mass M_{jj}, mass of the system X, M_X, and the dijet mass fraction R_{jj}, for the selected events with the proton detected in sector 56.

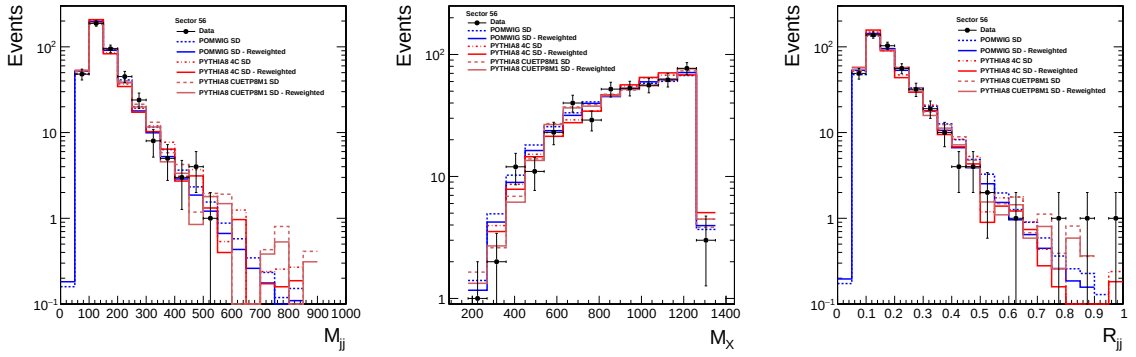

Legend: The solid lines show the distributions with the correction factors applied to POMWIG, PYTHIA8 4C and PYTHIA8 CUETP8M1. The Monte Carlo distributions are normalised to the number of events in the data.
Source: The author, 2017.

Figure 44 - Distribution of $\xi_{\mathrm{CMS}} - \xi_{\mathrm{TOTEM}}$ for events with a proton detected in sector 45 (left panel) and sector 56 (right panel).

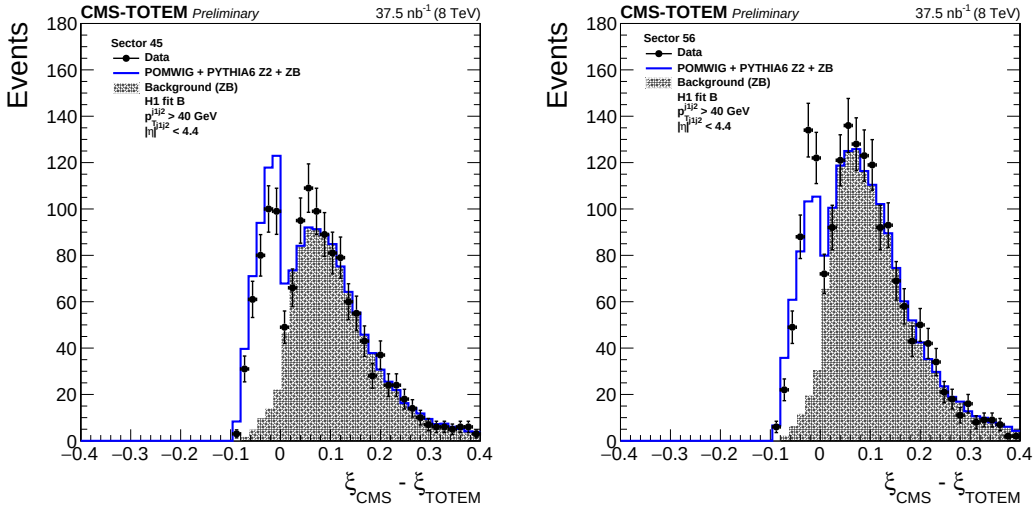

Legend: The data are indicated by full circles. The blue histogram is the mixture of POMWIG, PYTHIA and ZB data events described in the text. An event with the proton measured in the RPs contributes to the white histogram (signal) if it originates from the MC sample, or to the hatched histogram (background) if it originates from the ZB sample.
Source: The author, 2017.

The POMWIG sample was normalised as discussed in Sect. 3. The mixture MC+ZB was then passed through the selection procedure illustrated in Sect. 4.2, except for the cut $\xi_{\mathrm{CMS}} - \xi_{\mathrm{TOTEM}} \leq 0$, which was not applied.

An event with a proton in the RPs is considered as signal if it originates from the MC sample, or as background if it originates from the ZB sample. Should an event have a proton in both MC and ZB sample, the proton with smallest ξ is chosen. The probability of such combination is however small and none of these events pass all selection cuts. The background is estimated separately for top-top and bottom-bottom RPs and the combination of these is used in the analysis. Figure 44 shows the distribution of $\xi_{\mathrm{CMS}} - \xi_{\mathrm{TOTEM}}$ for the data compared to the MC+ZB mixture. The requirement $\xi_{\mathrm{CMS}} - \xi_{\mathrm{TOTEM}} \leq 0$ selects the signal events and rejects the kinematically forbidden region populated by the background events (hatched histogram). The background contribution is normalised in the $\xi_{\mathrm{CMS}} - \xi_{\mathrm{TOTEM}}$ region from 0.048 to 0.4. The remaining contamination of background in the signal region was estimated to be 13.3% for sector 45 and 15.7% for sector 56.

Figure 45 shows the distribution of ξ_{TOTEM}, for the data and the MC+ZB sample, before the $\xi_{\mathrm{CMS}} - \xi_{\mathrm{TOTEM}} \leq 0$ cut. Figure 46 shows the distribution of ξ_{TOTEM} after the $\xi_{\mathrm{CMS}} - \xi_{\mathrm{TOTEM}} \leq 0$ cut. The residual background after the $\xi_{\mathrm{CMS}} - \xi_{\mathrm{TOTEM}}$ cut is concentrated at values of ξ_{TOTEM} larger than about 0.05.

Figure 45 - Distribution of ξ_{TOTEM} for sector 45 (left) and sector 56 (right).

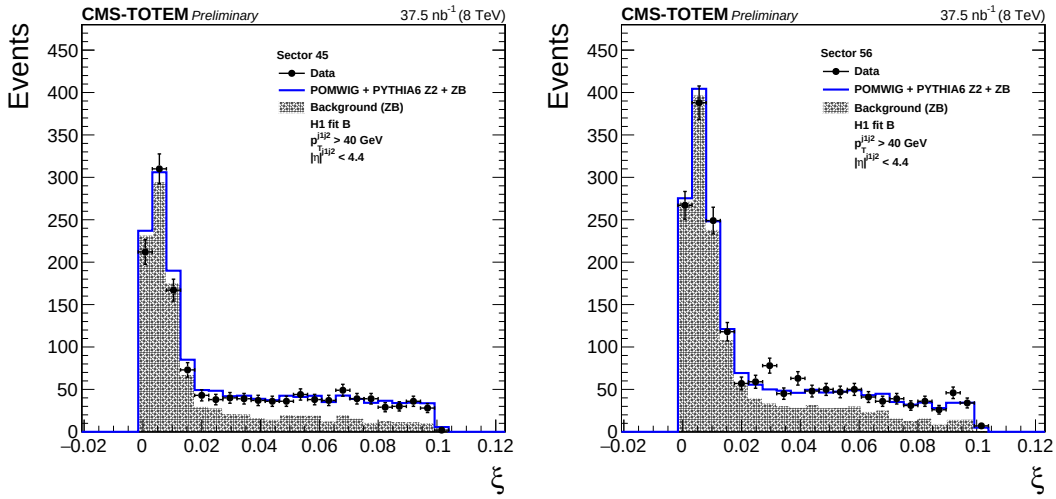

Legend: The data are indicated by full circles. The blue histogram is the mixture of Pomwig, Pythia and ZB data events described in the text. An event with the proton measured in the RPs contributes to the white histogram (signal) if it originates from the MC sample, or to the hatched histogram (background) if it originates from the ZB sample.
Source: The author, 2017.

Figure 46 - Distribution of ξ_{TOTEM} after the $\xi_{\mathrm{CMS}} - \xi_{\mathrm{TOTEM}}$ cut for sector 45 (left) and sector 56 (right).

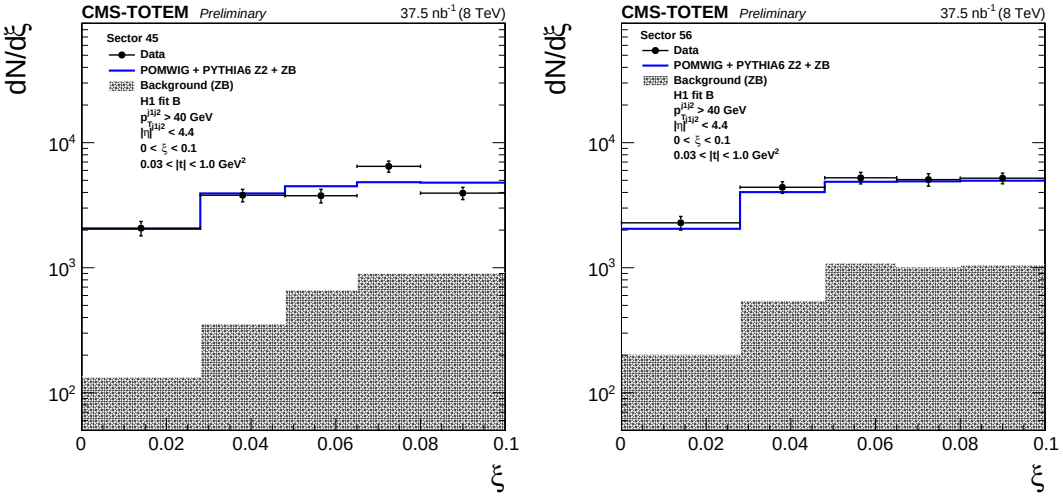

Legend: The data are indicated by full circles. The blue histogram is the mixture of Pomwig, Pythia and ZB data events described in the text. An event with the proton measured in the RPs contributes to the white histogram (signal) if it originates from the MC sample, or to the hatched histogram (background) if it originates from the ZB sample.
Source: The author, 2017.

Figure 47 - Distribution of t after the $\xi_{\mathrm{CMS}} - \xi_{\mathrm{TOTEM}}$ cut for sector 45 (left) and sector 56 (right).

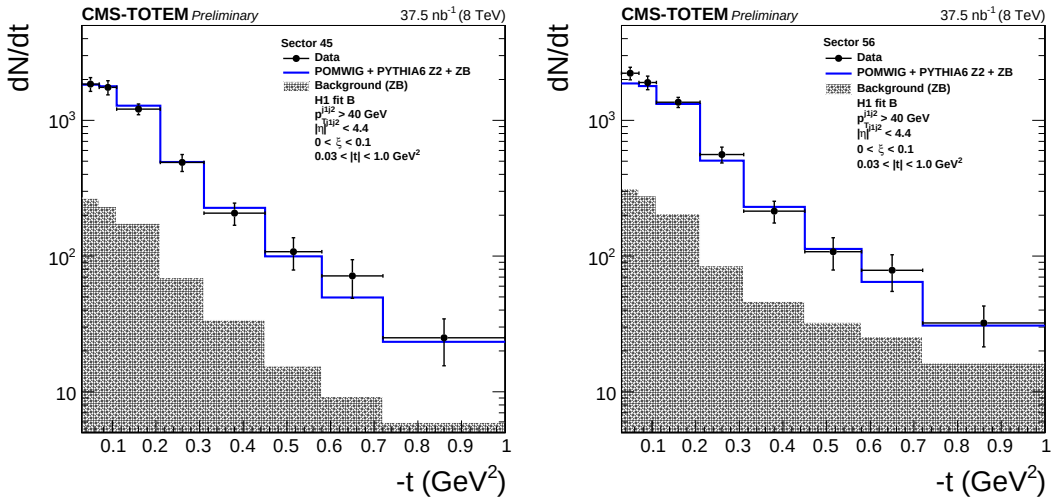

Legend: The data are indicated by full circles. The blue histogram is the mixture of POMWIG, PYTHIA and ZB data events described in the text. An event with the proton measured in the RPs contributes to the white histogram (signal) if it originates from the MC sample, or to the hatched histogram (background) if it originates from the ZB sample.
Source: The author, 2017.

Figure 47 shows the distributions as a function of t, also after the $\xi_{\mathrm{CMS}} - \xi_{\mathrm{TOTEM}} \leq 0$ cut.

2. **HERA method:**

This method, used by the ZEUS Collaboration (8), relies on the data to estimate the beam-halo and pileup background contribution. First, ξ_{CMS} is calculated from a random event passing the dijet selection. A second event is used to obtain a value of ξ_{TOTEM} if it has passed all selection criteria (see Sect. 4.2) and in addition satisfies the condition $\xi_{\mathrm{CMS}} > 0.12$. This requirement selects mostly events with a proton from background. These two values are used to plot the $\xi_{\mathrm{CMS}} - \xi_{\mathrm{TOTEM}}$ distribution, normalised to the data in the background-dominated region. Figure 48 shows the resulting background distribution compared to the data.

Figure 49 shows the distribution of the background as a function of ξ (red line) compared with the data.

The $\xi_{\mathrm{CMS}} - \xi_{\mathrm{TOTEM}} \leq 0$ requirement selects the signal events and rejects the kinematically forbidden region populated by the background events. The remaining contamination of background in the signal region was estimated to be $\sim 18.7\%$ for sector 45 and $\sim 18.8\%$ for sector 56. Figures 50 and 51 show the distributions of ξ and t after this cut.

Figure 48 - Distribution of $\xi_{\mathrm{CMS}} - \xi_{\mathrm{TOTEM}}$ for sector 45 (left) and 56 (right).

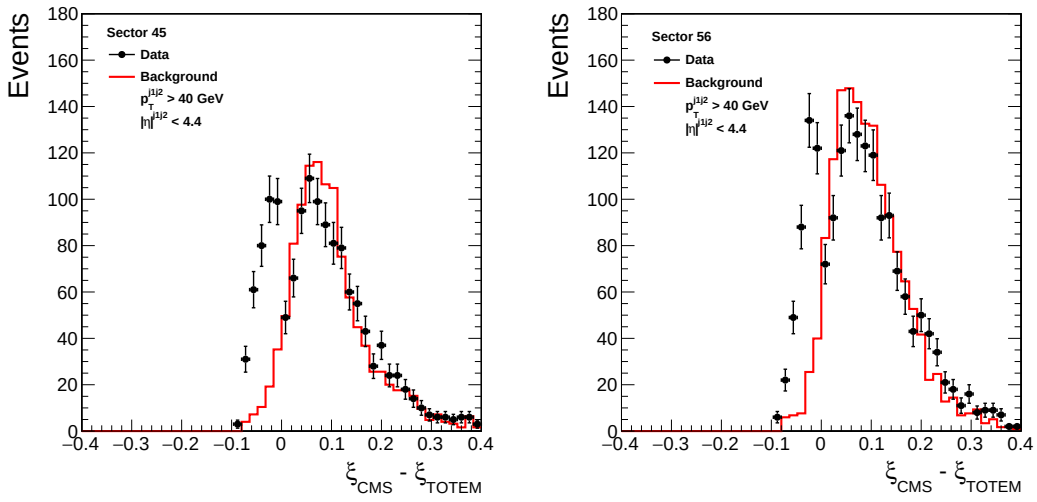

Legend: The data are indicated by full circles. Red histograms represent the background estimated from the data sample as explained in the text.
Source: The author, 2017.

Figure 49 - Distribution of ξ for sector 45 (left) and 56 (right).

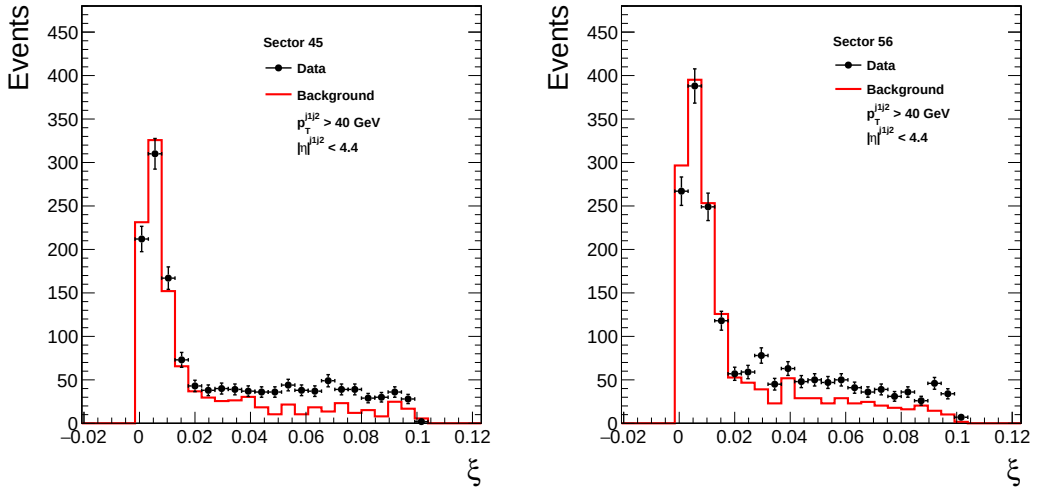

Legend: The data are indicated by full circles. Red histograms represent the background estimated from the data sample.
Source: The author, 2017.

Figure 50 - Distribution of ξ after the $\xi_{\text{CMS}} - \xi_{\text{TOTEM}} \leq 0$ cut for sector 45 (left) and sector 56 (right).

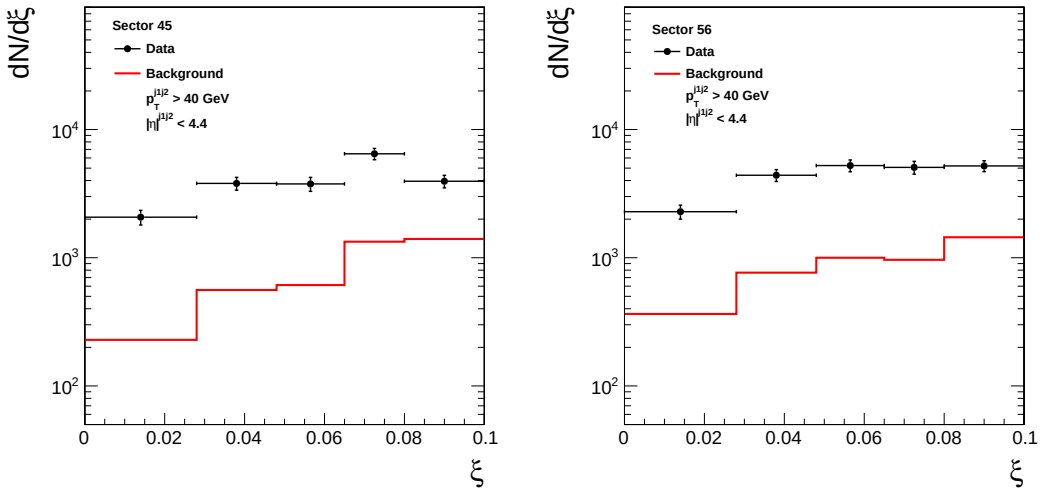

Legend: The data are indicated by full circles. Red histograms represent the background estimated from the data sample.
Source: The author, 2017.

Figure 51 - Distribution of t after the $\xi_{\text{CMS}} - \xi_{\text{TOTEM}} \leq 0$ cut for sector 45 (left) and sector 56 (right).

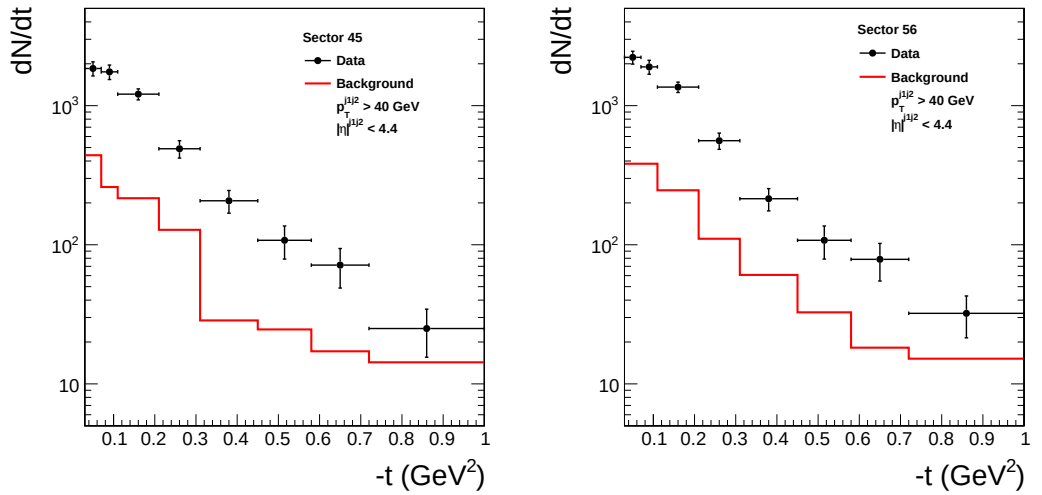

Legend: The data are indicated by full circles. Red histograms represent the background estimated from the data sample.
Source: The author, 2017.

Figure 52 - Distribution of $\xi_{\mathrm{CMS}} - \xi_{\mathrm{TOTEM}}$ for events in sector 45 (left) and sector 56 (right), for top and bottom configurations.

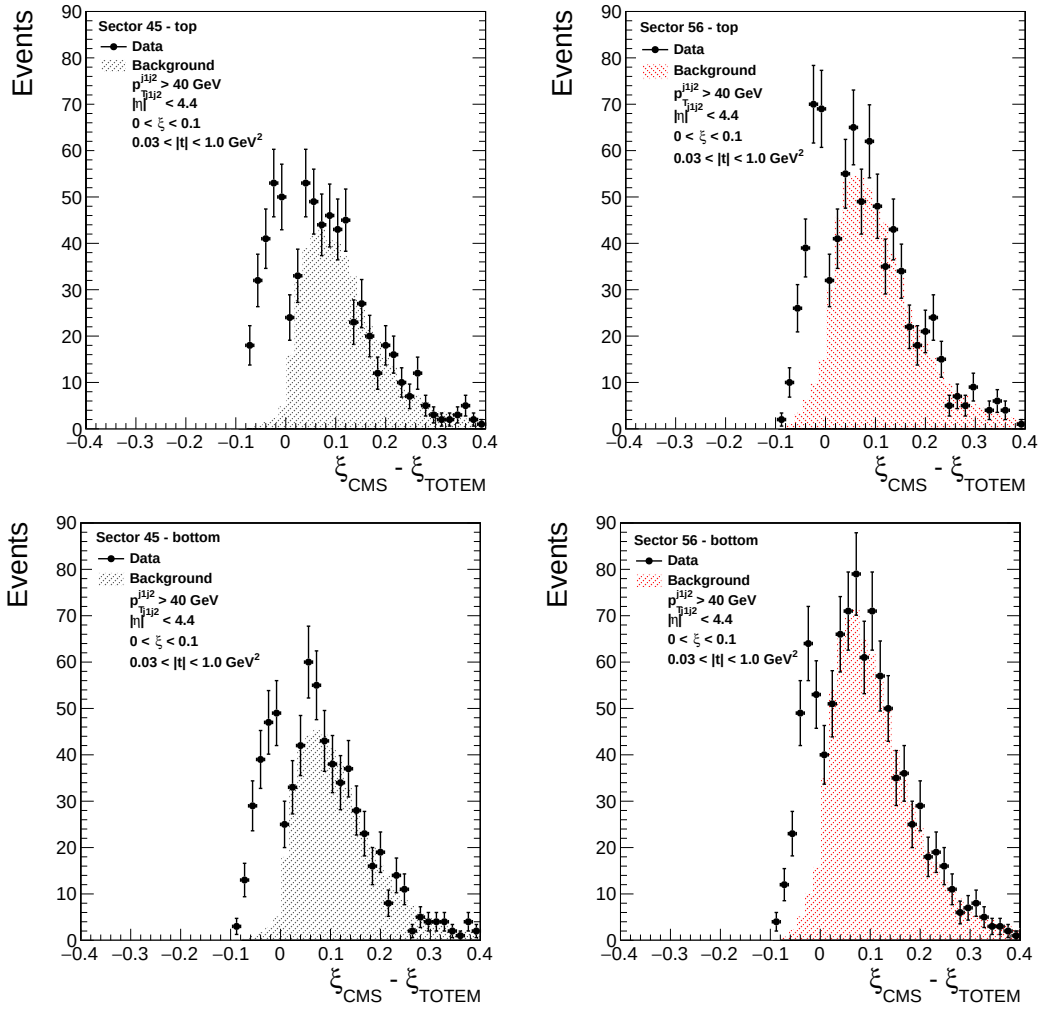

Legend: The data are indicated by full circles. The red and gray histograms represent the background in each case.
Source: The author, 2017.

Both methods provide a good description of the background. The ZB method is used in the analysis.

As mentioned above the background is estimated separately for the top-top and bottom-bottom configurations. The distributions of $\xi_{\mathrm{CMS}} - \xi_{\mathrm{TOTEM}}$ for each of them are shown in Figure 52.

Figure 53 shows the x and y position of tracks in the RP stations separately for events selected as top-top and bottom-bottom. These distributions do not include the requirement of $\xi_{\mathrm{CMS}} - \xi_{\mathrm{TOTEM}} \leq 0$ and are compared with the background estimates for each configuration. Figure 54 shows the x and y position of tracks in the RPs after the $\xi_{\mathrm{CMS}} - \xi_{\mathrm{TOTEM}}$ cut.

Figure 55 shows the distributions of t and ξ after all selection criteria, including

Figure 53 - Distribution of x (left panel) and y (right panel) position of tracks in the RP stations.

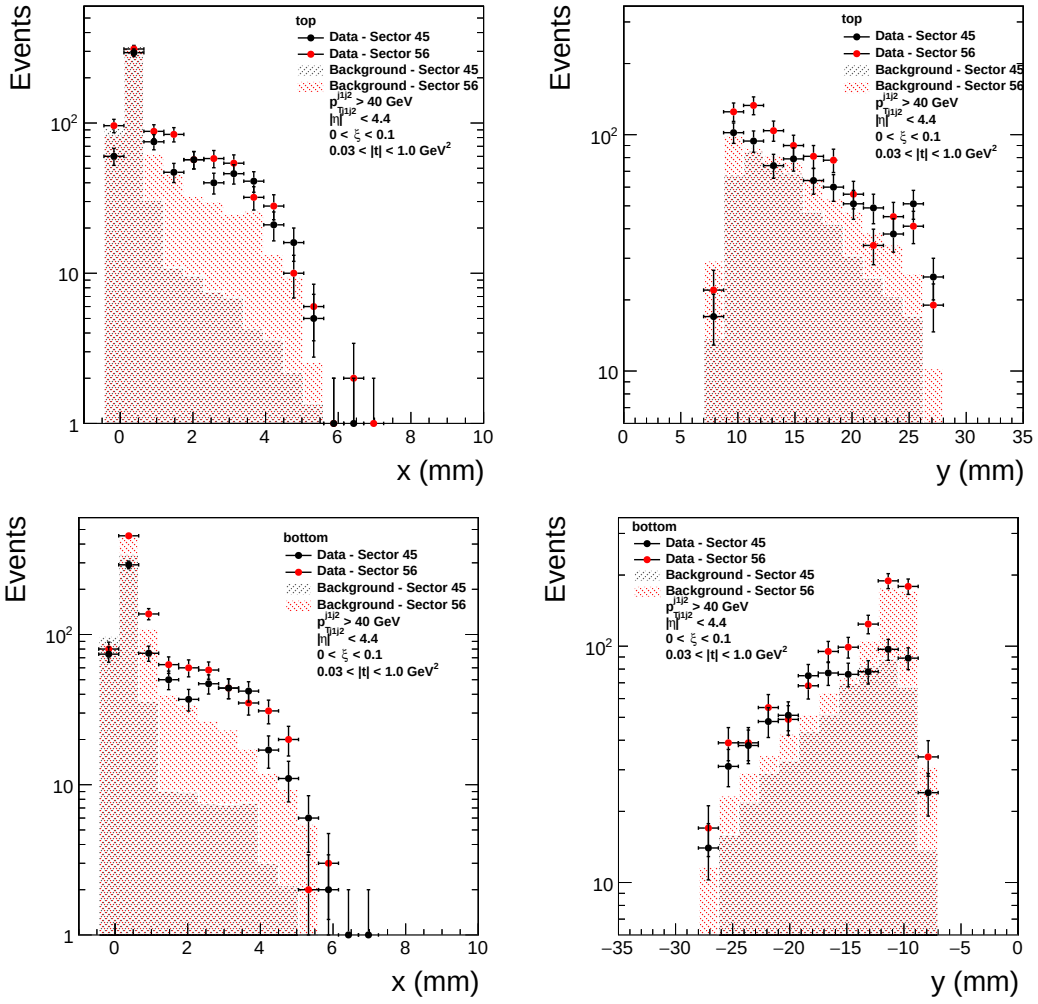

Legend: The events are selected before the $\xi_{\mathrm{CMS}} - \xi_{\mathrm{TOTEM}}$ cut, for top and bottom configurations. The data are indicated by full circles. The red and gray histograms represent the background in each case.

Source: The author, 2017.

Figure 54 - Distribution of x (left panel) and y (right panel) position of tracks in the RP stations.

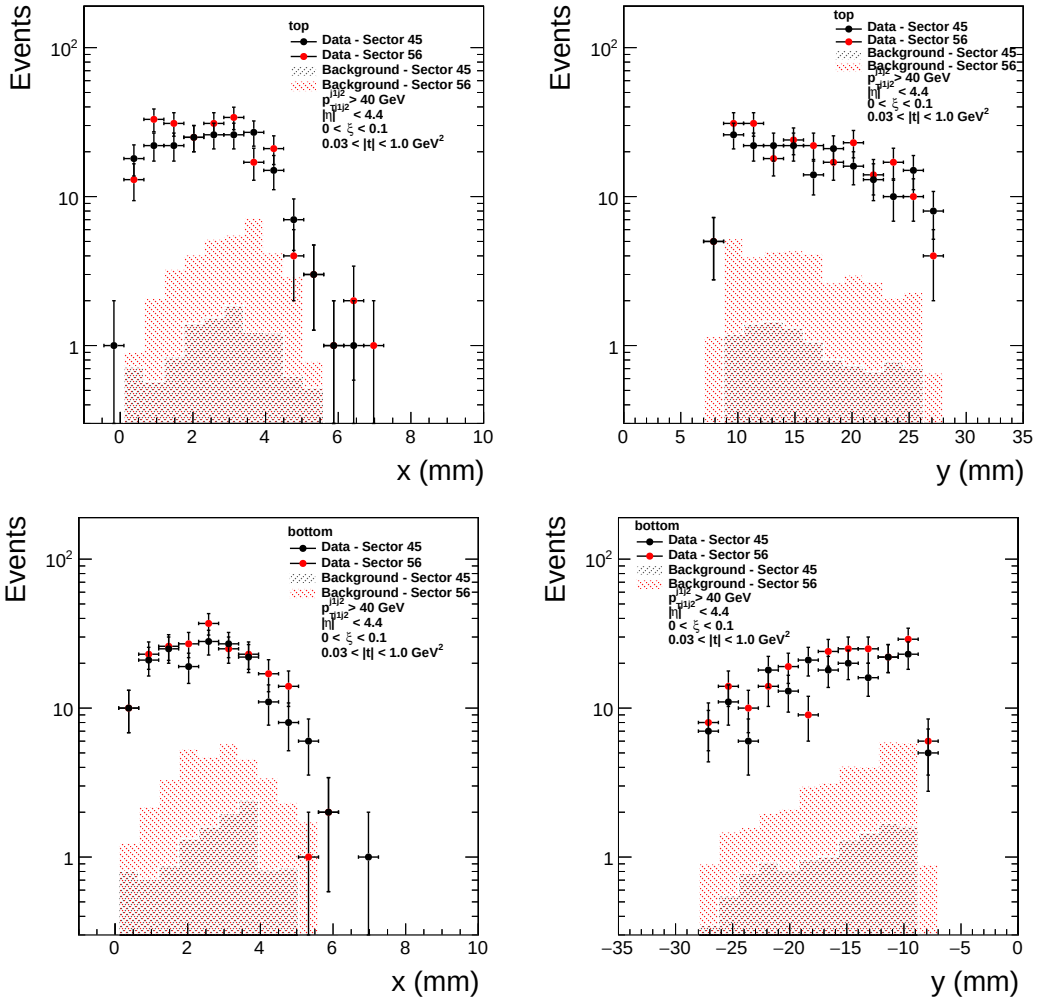

Legend: The events are shown after the selection including the $\xi_{\mathrm{CMS}} - \xi_{\mathrm{TOTEM}}$ cut, for top and bottom configurations. The data are indicated by full circles. The red and gray histograms represent the background in each case.

Source: The author, 2017.

Figure 55 - Distribution of t (left panel) and ξ (right panel).

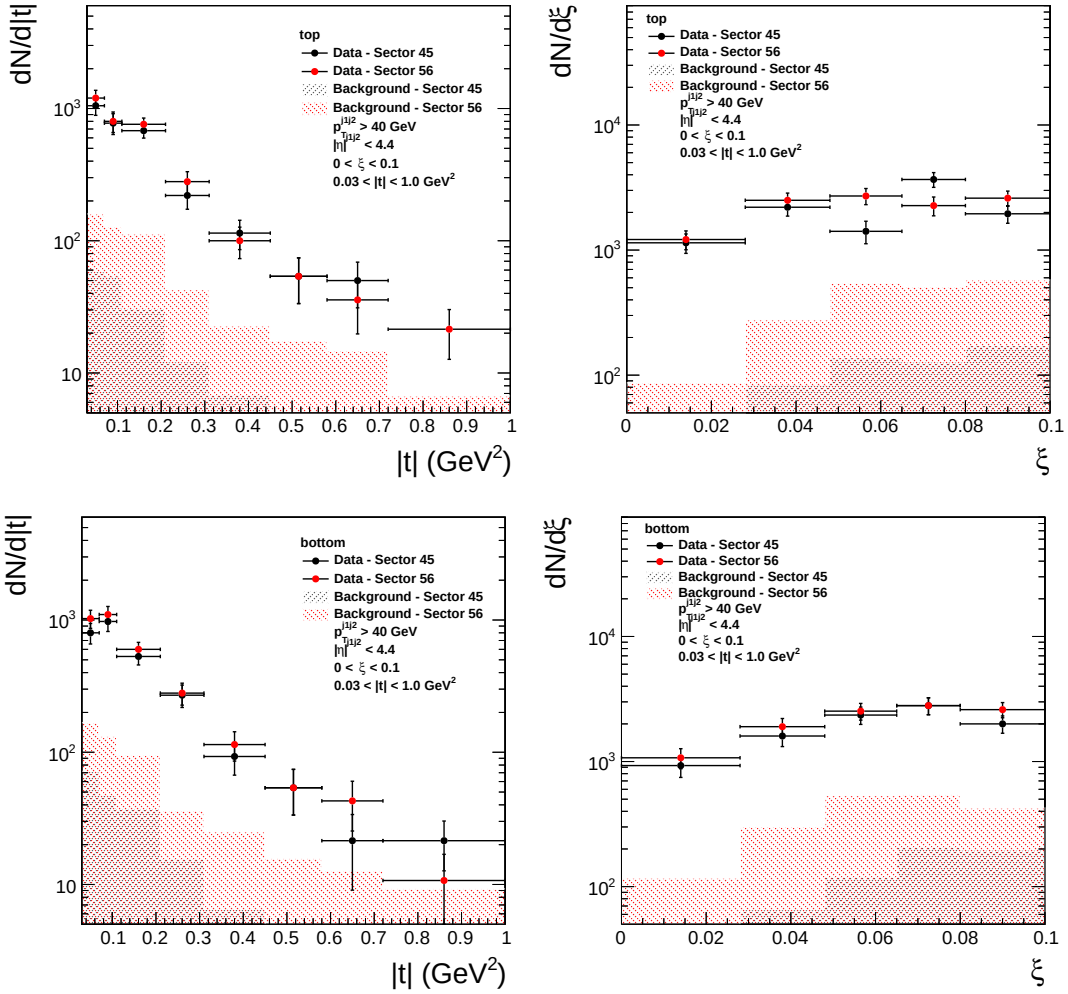

Legend: The events are shown after the selection including the $\xi_{\mathrm{CMS}} - \xi_{\mathrm{TOTEM}}$ cut, for top and bottom configurations. The data are indicated by full circles. The red and gray histograms represent the background in each case.
Source: The author, 2017.

the $\xi_{\mathrm{CMS}} - \xi_{\mathrm{TOTEM}}$ cut. The distributions are compared with the background estimated for each configuration.

4.4 **Unfolding**

A central part in the measurement is the correction from the reconstruction level to the truth level by accounting for the finite resolution of the detector. This procedure is called unfolding and is performed constructing the detector response in the form of a response matrix. The response matrix connects the true signal to the measured signal in the detector. The correlation given by the response matrix is then used to recover the

true signal. The relation between the measured distribution m and the truth distribution t is thus given by:

$$m = Rt \tag{22}$$

where R is the response matrix.

Unfolding aims to find the truth distribution by matrix inversion. There are several methods of unfolding which yield consistent results.

D'Agostini method with early stopping (60) is used in the analysis and implemented through the RooUnfold package. It corrects the data in every iteration starting from a MC prediction of the true histogram. The iteration converges to the unregularized Maximum Likelihood Estimate (61). Regularization is achieved by stopping the iteration prematurely before convergence.

The response matrix or smearing matrix corresponds to the probability $P(m_j|t_i)$, that having a certain generated value t_i, the observed one will be m_j. The response matrices to perform the unfolding in the single-diffractive events are shown in Figures 56, 57 and 58, calculated with POMWIG, PYTHIA8 4C and PYTHIA8 CUETP8M1 repectively. Reponse matrices of the inclusive dijet data are shown in Figures 59, 60, 61 and 62, calculated with PYTHIA6, HERWIG6, PYTHIA8 4C and PYTHIA8 CUETP8M1 respectively.

The regularisation parameter that represents the number of iterations must be chosen based on an objective criterion. In this analysis this number is obtained from the relative change of χ^2 for an iteration compared to the previous one. The χ^2 value is calculated comparing the unfolded MC distribution with its true distribution. This is done with the diffractive MC as shown in Figures 63 and 64 and with the inclusive MC as shown in Figure 65. The number of iterations for each distribution is chosen when the relative change of χ^2 is 5%, represented by the red solid line. The unfolded distributions also were obtained with the number of iterations when the relative change of χ^2 is 2%, represented by the red dashed line. The difference between the unfolded distributions with the two choices of regularisation parameter is taken as a systematic uncertainty.

The test to check if the regularisation parameter is correct is performed calculating the values of $\chi^2_{unfolded}$ and $\chi^2_{smeared}$, where the former refers to the comparison between the unfolded data distributions and the true distributions from the MC, while the latter refers to the χ^2 value calulated by comparing the MC detector level distributions to the data. The test consist to obtain values of $\chi^2_{unfolded} < \chi^2_{smeared}$. This means that the agreement between the data and the model cannot become worse after unfolding. Figures 66 and 67 show the $\chi^2_{unfolded}$ values per iteration for single-diffractive events and Figure 68 for inclusive events, the solid lines represent the values of $\chi^2_{smeared}$. For $N_{iter} > 3$ almost all the distributions are in agreement with the condition above.

Regularisation introduces a bias towards the MC spectrum, and therefore must be

Figure 56 - Response matrix for t, ξ and $\log(x)$ with POMWIG.

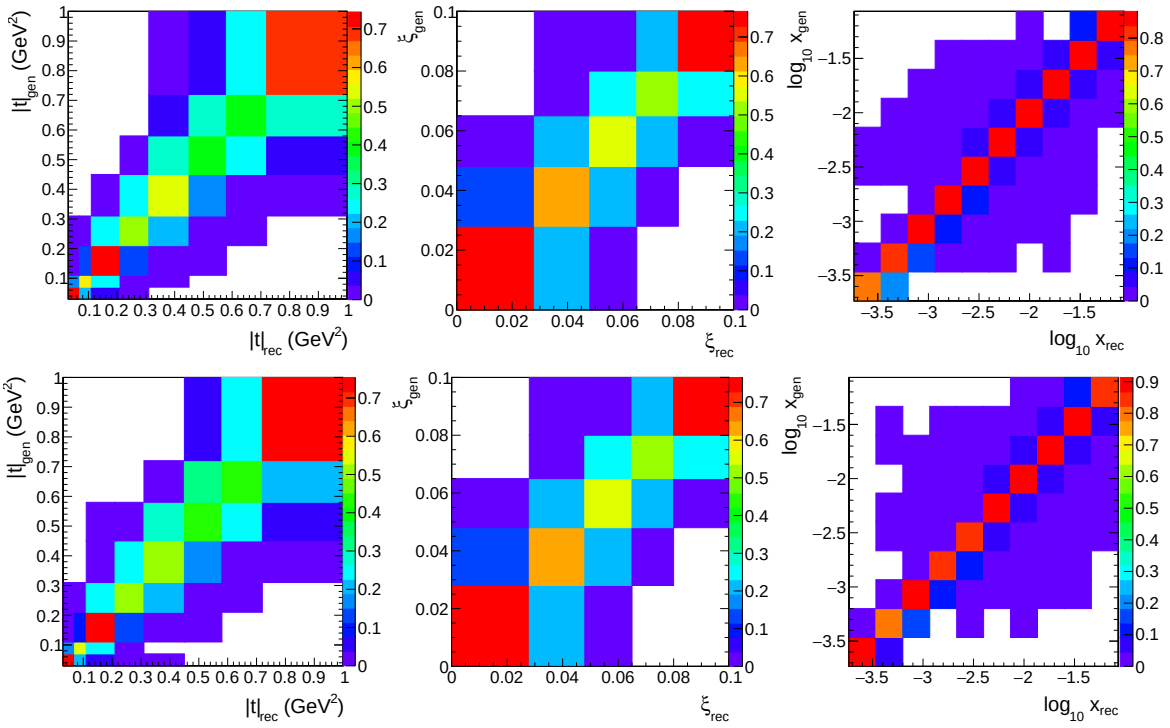

Legend: The plots are shown for events in which the proton is detected in sector 45 (top) and sector 56 (bottom). The matrices are normalized to represent the probability to obtain a true value in each bin.

Source: The author, 2017.

Figure 57 - Response matrix for t, ξ and $\log(x)$ with PYTHIA8 4C.

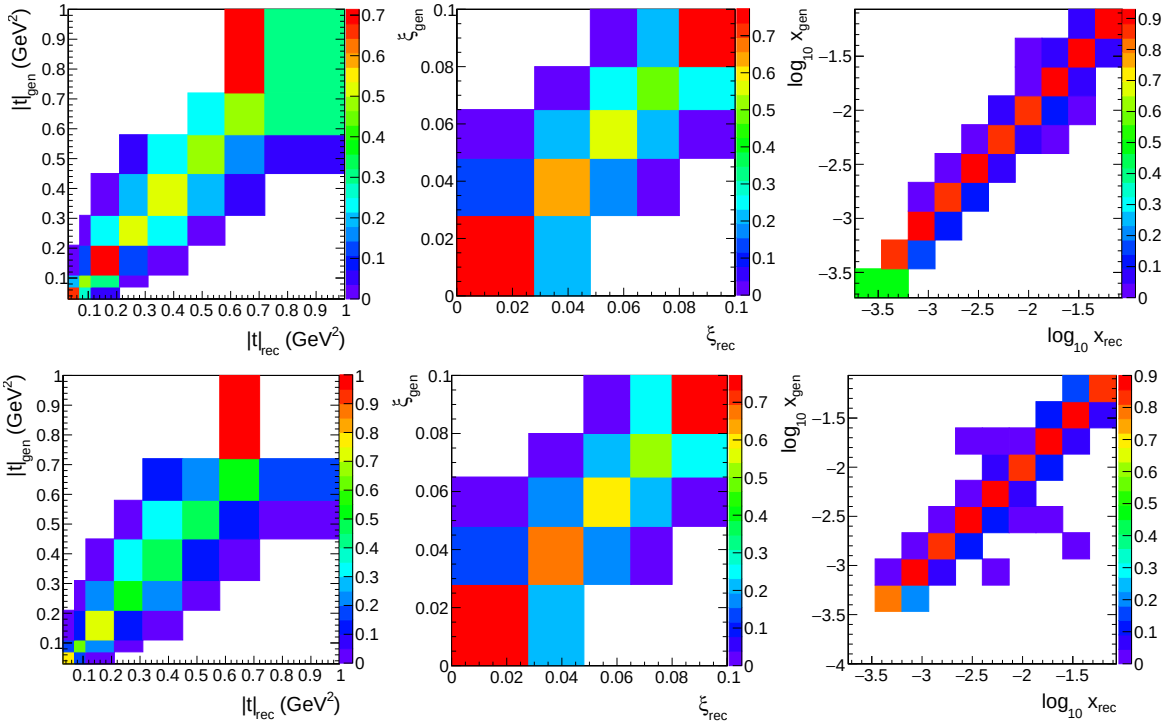

Legend: The plots are shown for events in which the proton is detected in sector 45 (top) and sector 56 (bottom). The matrices are normalized to represent the probability to obtain a true value in each bin.

Source: The author, 2017.

Figure 58 - Response matrix for t, ξ and $\log(x)$ with PYTHIA8 CUETP8M1.

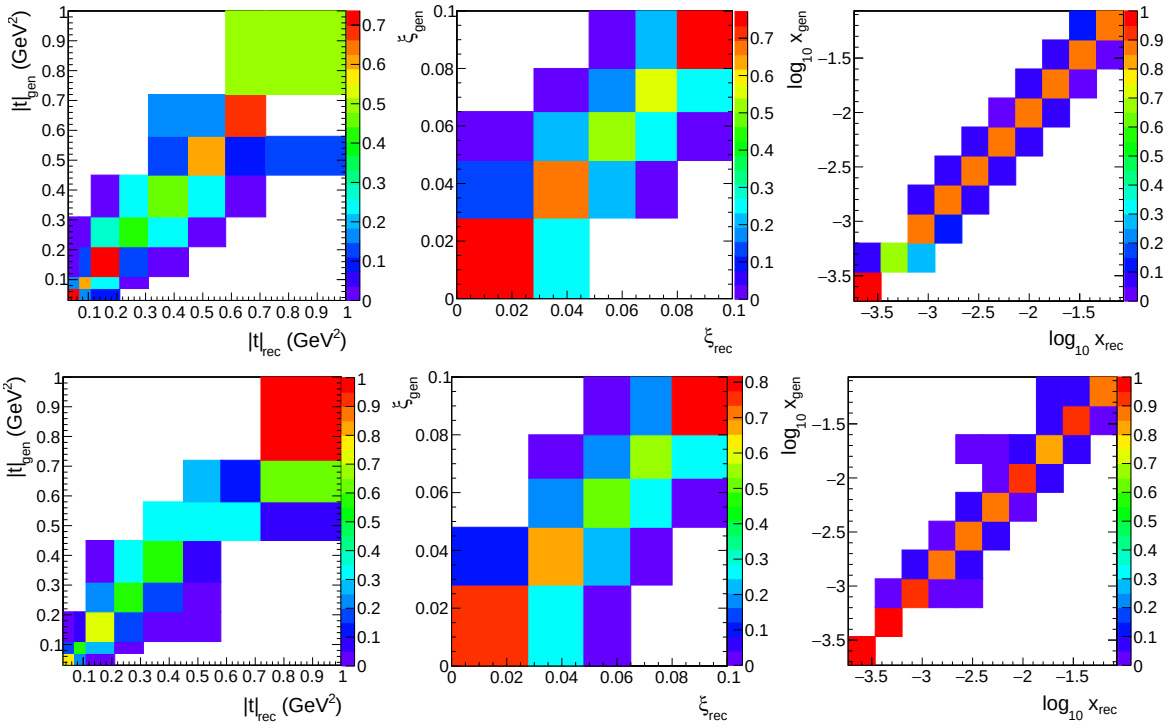

Legend: The plots are shown for events in which the proton is detected in sector 45 (top) and sector 56 (bottom). The matrices are normalized to represent the probability to obtain a true value in each bin.
Source: The author, 2017.

Figure 59 - Response matrix for $\log(x)$ with PYTHIA6.

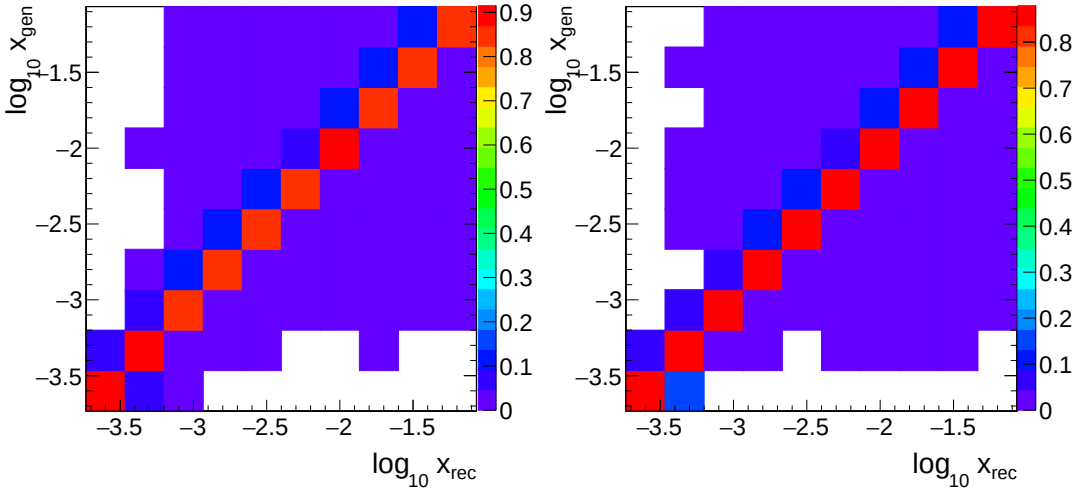

Legend: The left panel refers to the interacting parton longitudinal momentum towards the positive z direction and the right panel towards the negative z direction. The matrices are normalized to represent the probability to obtain a true value in each bin.
Source: The author, 2017.

Figure 60 - Response matrix for $\log(x)$ with HERWIG6.

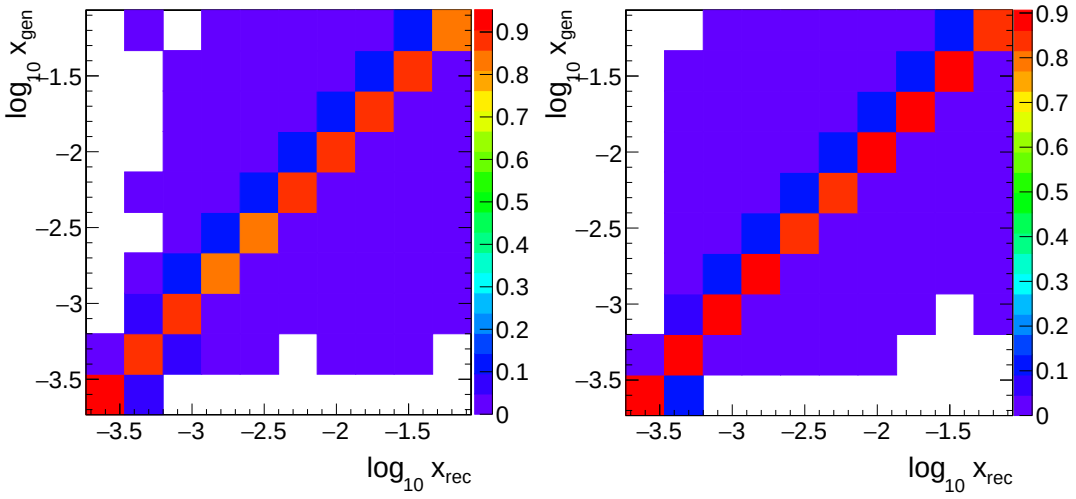

Legend: The left panel refers to the interacting parton longitudinal momentum towards the positive z direction and the right panel towards the negative z direction. The matrices are normalized to represent the probability to obtain a true value in each bin.
Source: The author, 2017.

Figure 61 - Response matrix for $\log(x)$ with PYTHIA8 4C.

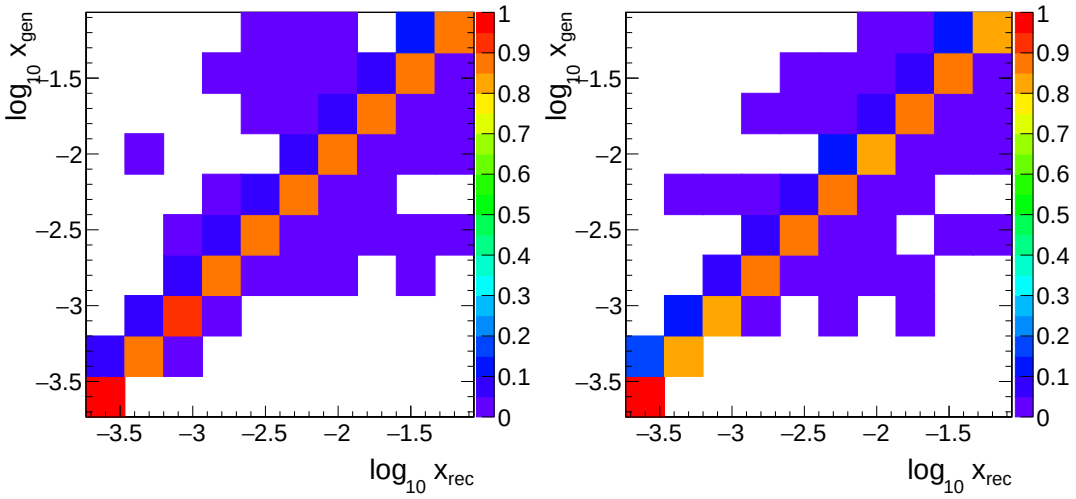

Legend: The left panel refers to the interacting parton longitudinal momentum towards the positive z direction and the right panel towards the negative z direction. The matrices are normalized to represent the probability to obtain a true value in each bin.
Source: The author, 2017.

Figure 62 - Response matrix for $\log(x)$ with PYTHIA8 CUETP8M1.

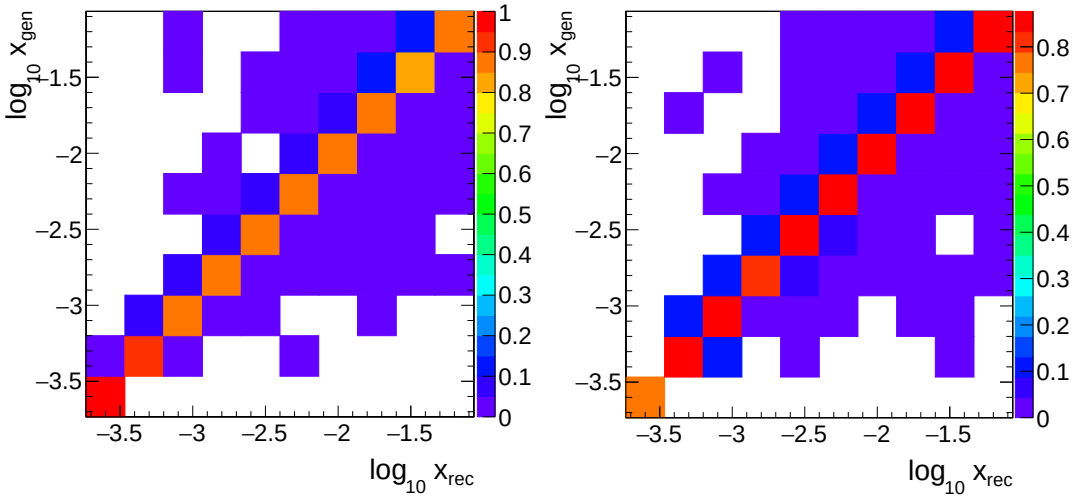

Legend: The left panel refers to the interacting parton longitudinal momentum towards the positive z direction and the right panel towards the negative z direction. The matrices are normalized to represent the probability to obtain a true value in each bin.
Source: The author, 2017.

Figure 63 - Relative change of χ^2 distribution.

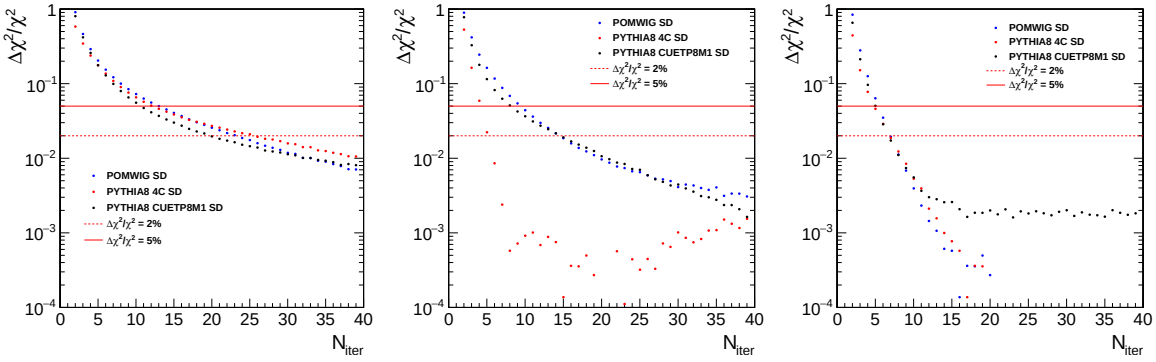

Legend: χ^2 is compared to the previous number of iterations $(\chi^2_{N_{iter}} - \chi^2_{N_{iter}-1})/\chi^2_{N_{iter}}$ for the t (left), ξ (central) and $\log(x)$ (right) distributions for events in sector 45. Blue points represent the values for the unfolded distribution with POMWIG, the red ones with PYTHIA8 4C and the black ones with PYTHIA8 CUETP8M1. The solid red line indicates $\Delta\chi^2/\chi^2 = 5\%$ and the red dashed line $\Delta\chi^2/\chi^2 = 2\%$.
Source: The author, 2017.

Figure 64 - Relative change of χ^2 distribution.

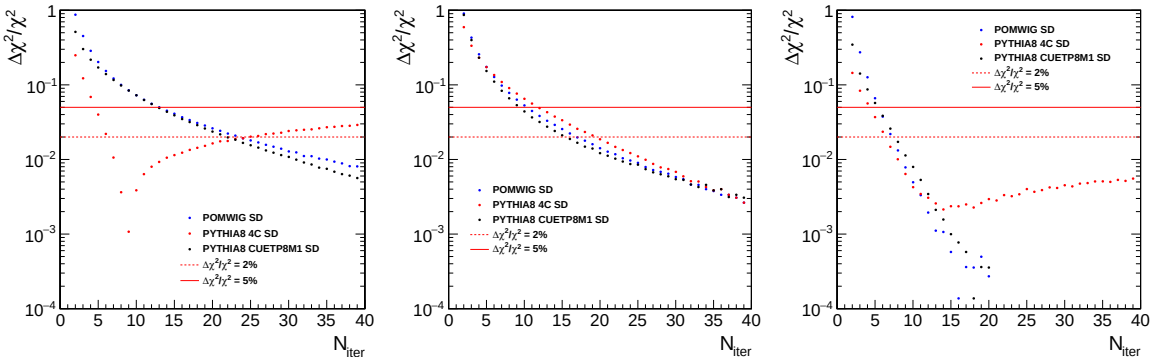

Legend: χ^2 is compared to the previous number of iterations $(\chi^2_{N_{iter}} - \chi^2_{N_{iter}-1})/\chi^2_{N_{iter}}$ for the t (left), ξ (central) and $\log(x)$ (right) distributions for events in sector 56. Blue points represent values for the unfolded distribution with POMWIG, the red ones with PYTHIA8 4C and the black ones with PYTHIA8 CUETP8M1. The solid red line indicates $\Delta\chi^2/\chi^2 = 5\%$ and the red dashed line $\Delta\chi^2/\chi^2 = 2\%$.
Source: The author, 2017.

Figure 65 - Relative change of χ^2 distribution.

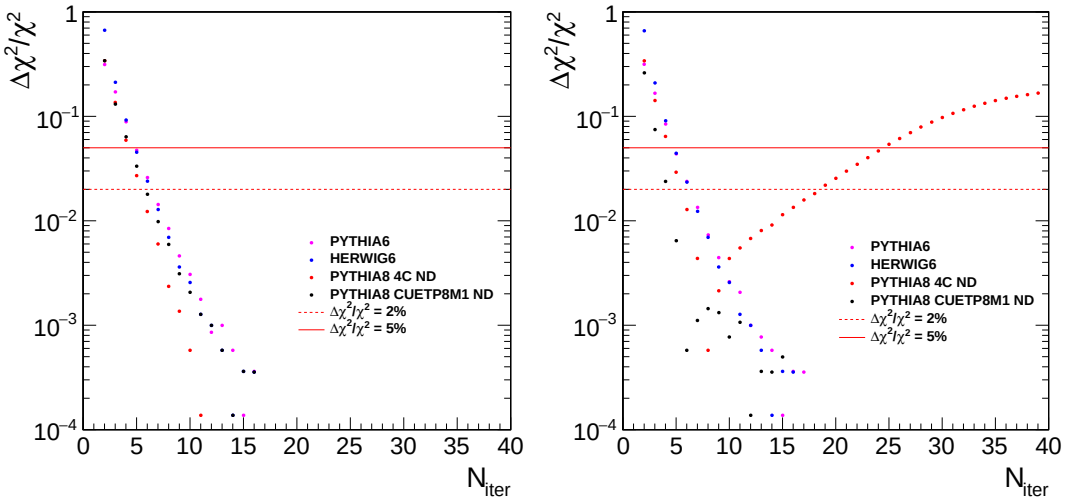

Legend: χ^2 compared to the previous number of iterations $(\chi^2_{N_{iter}} - \chi^2_{N_{iter}-1})/\chi^2_{N_{iter}}$ for the $\log(x)$ distribution. The left panel refers to the interacting parton longitudinal momentum towards the positive z direction and the right panel towards the negative z direction. Magenta points represent the unfolded distribution with PYTHIA6, the blue points represent the unfolded distribution with HERWIG6, the red ones with PYTHIA8 4C and the black ones with PYTHIA8 CUETP8M1. The solid red line indicates $\Delta\chi^2/\chi^2 = 5\%$ and the red dashed line $\Delta\chi^2/\chi^2 = 2\%$.
Source: The author, 2017.

Figure 66 - $\chi^2_{unfolded}$ values per iteration for the t (left), ξ (central) and $\log(x)$ (right) distributions for events in sector 45.

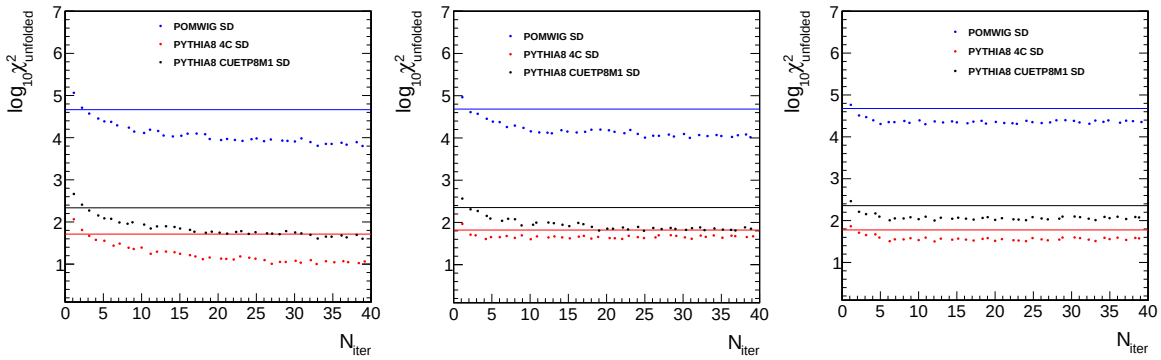

Legend: Blue points represent the values for the unfolded distributions with Pomwig and the blue solid line its corresponding $\chi^2_{smeared}$ value. Red points and red solid line represent the values with Pythia8 4C and the black proints and black solid line for Pythia8 Cuetp8m1.
Source: The author, 2017.

Figure 67 - $\chi^2_{unfolded}$ values per iteration for the t (left), ξ (central) and $\log(x)$ (right) distributions for events in sector 56.

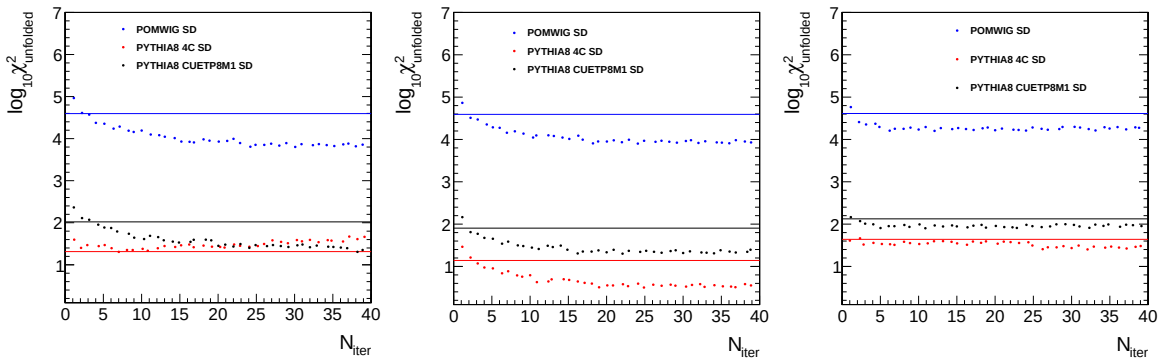

Legend: Blue points represent the values for the unfolded distributions with Pomwig and the blue solid line its corresponding $\chi^2_{smeared}$ value. Red points and red solid line represent the values with Pythia8 4C and the black proints and black solid line for Pythia8 Cuetp8m1.
Source: The author, 2017.

Figure 68 - $\chi^2_{unfolded}$ values per iteration for the $\log(x)$ distribution.

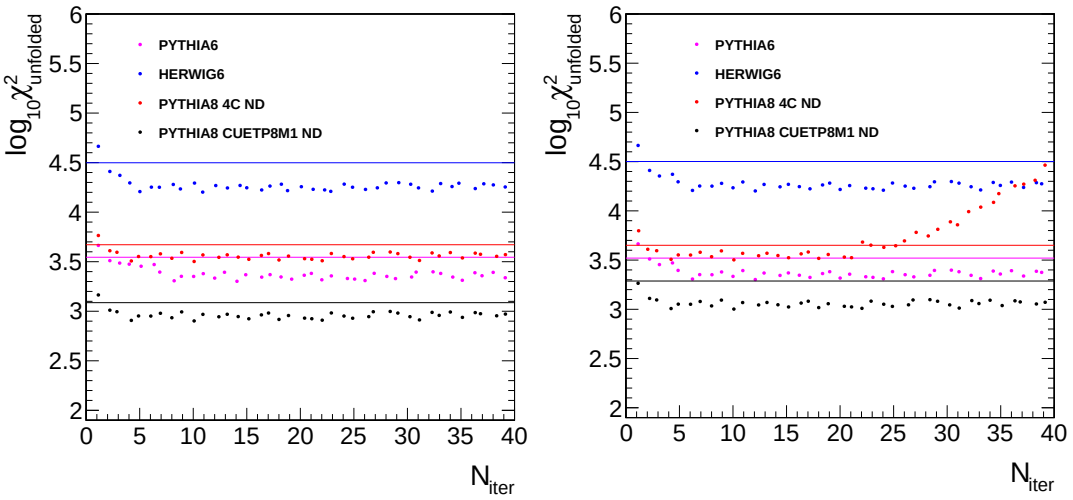

Legend: The left panel refers to the interacting parton longitudinal momentum towards the positive z direction and the right panel towards the negative z direction. Magenta points represent the values for the unfolded distributions with PYTHIA6 and the magenta solid line its corresponding $\chi^2_{smeared}$ value, the blue points and the blue solid line for HERWIG6, red points and red solid line represent the values with PYTHIA8 4C and the black proints and black solid line for PYTHIA8 CUETP8M1.
Source: The author, 2017.

taken into account in the uncertainties. This is estimated by unfolding the detector level distributions generated using a model, MC1, with a second model, MC2. The size of the bias is calculated comparing the unfolded MC1 and the true distribution from MC1. This is done using the combinations between all the MC models in the analysis as is shown in the Figures 69 and 70. The maximum difference is used as a systematic uncertainty.

Figure 69 - Unfolding bias for events in sector 45.

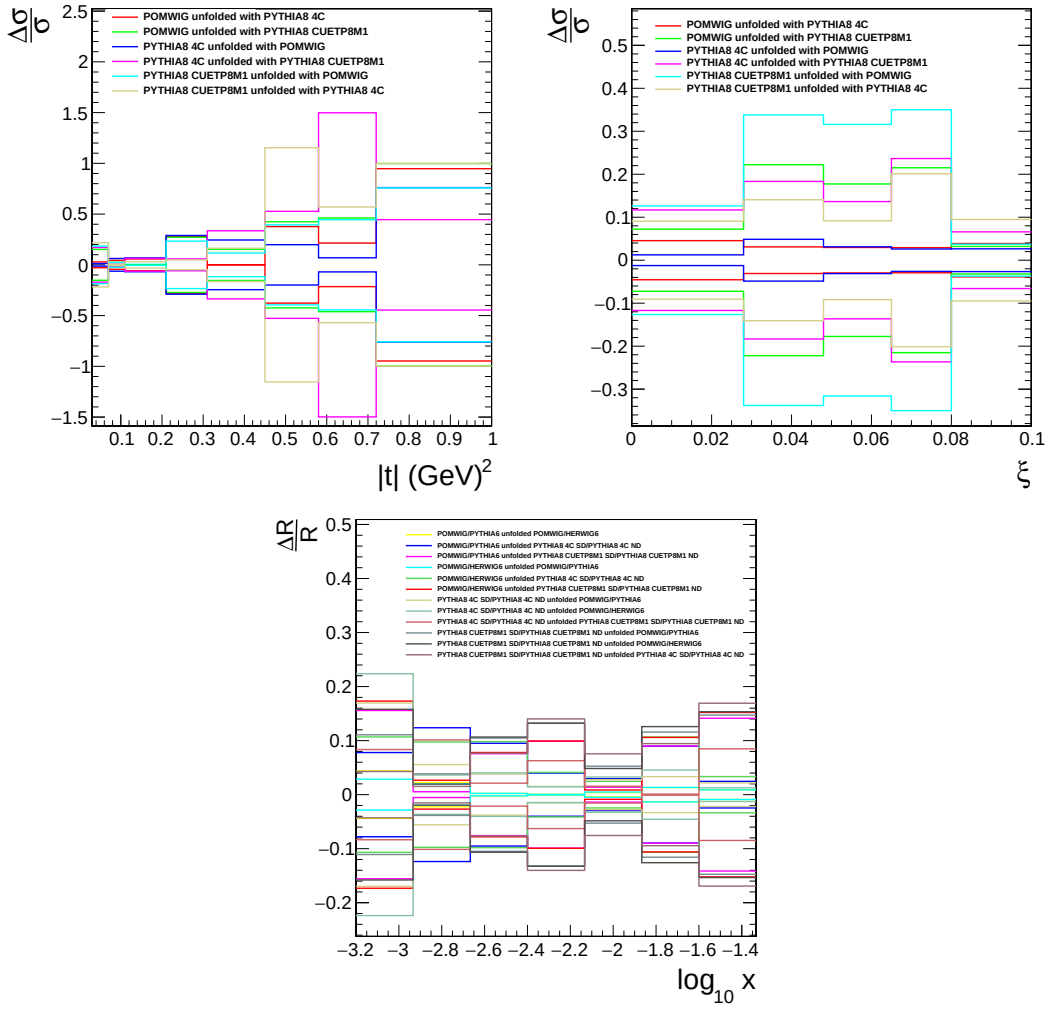

Legend: Top: Unfolding bias of the cross section as a function of t (left), ξ (right). Bottom: Unfolding bias of the ratio of diffractive and inclusive cross sections as a function of $\log(x)$. The relative variations are shown with respect to the value in each bin.

Source: The author, 2017.

Figure 70 - Unfolding bias for events in sector 56.

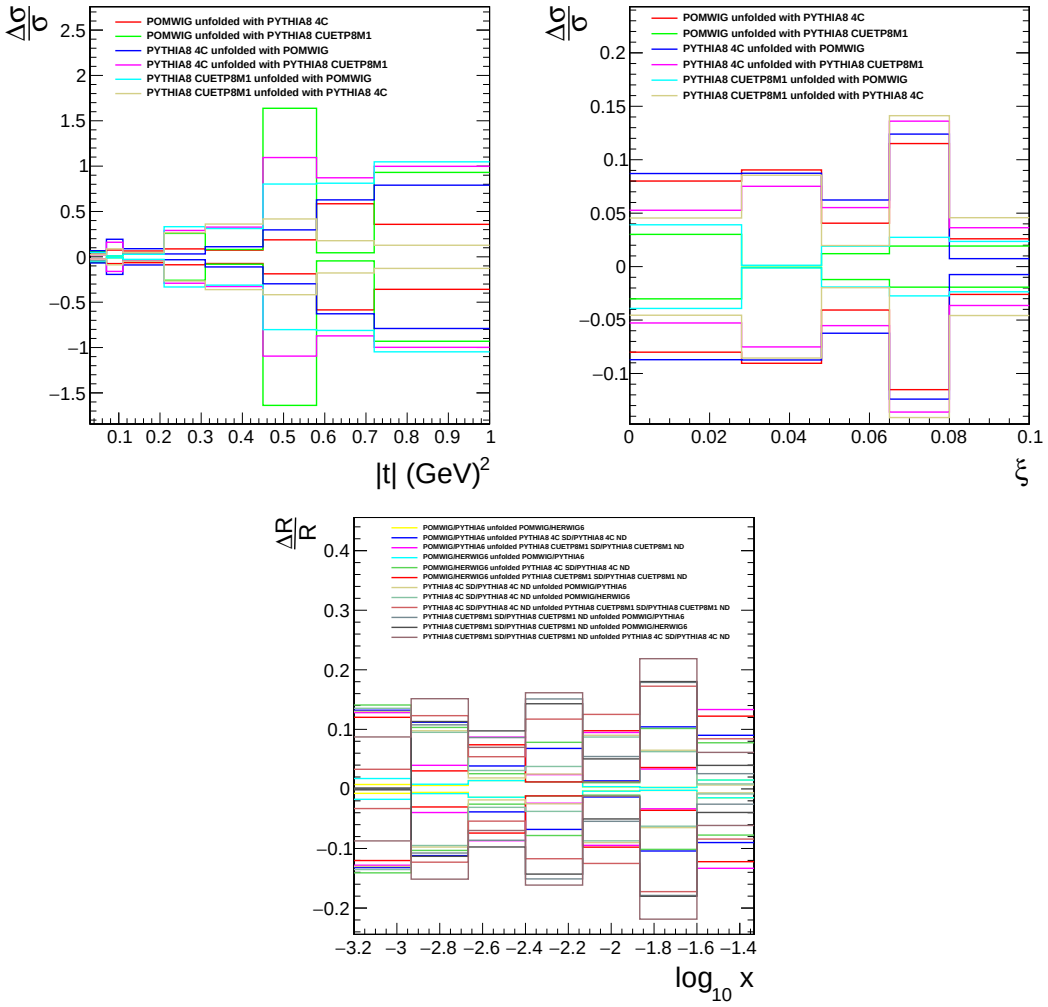

Legend: Top: Unfolding bias of the cross section as a function of t (left), ξ (right). Bottom: Unfolding bias of the ratio of diffractive and inclusive cross sections as a function of $\log(x)$. The relative variations are shown with respect to the value in each bin.

Source: The author, 2017.

5 RESULTS

This chapter presents the measurement of the cross sections $d\sigma/dt$, $d\sigma/d\xi$ and the ratio $R(x)$ of the diffractive and inclusive dijet cross sections, as well as the integrated cross section in the kinematic region defined by $\xi < 0.1$, $0.03 < |t| < 1$ GeV^2, for jets with $p_T > 40$ GeV and $|\eta| < 4.4$.

5.1 Systematic uncertainties

The systematic uncertainties were estimated by varying the cuts and modifying the analysis procedure. The following checks were performed:

- **Trigger efficiency:** The uncertainty due to the trigger efficiency was calculated by varying the fit parameters within uncertainties (see Sect. 4.2).
- **Calorimenter Energy Scale:** The uncertainty due to the calorimeter energy-scale was estimated by changing the energy of the particle-flow objects by ±10%.
- **Jet Energy Scale:** The energy of the reconstructed jets was varied according to the jet energy-scale uncertainty following the procedure described in Ref. (58).
- **Background:** Half the difference between the results of the two methods used to estimate the background (see Sect. 4.3) was taken as a systematic uncertainty.
- **RP acceptance:** The sensitivity to the size of the fiducial region for the impact position of the proton in the RPs was estimated by modifying its vertical boundaries by 200 μm and by reducing the horizontal cut by 1 mm to $0 < x < 6$ mm. Half the difference of the results was used as a systematic uncertainty. The uncertainties obtained when modifying the vertical and horizontal boundaries were added in quadrature.
- **Beam-divergence:** The reconstructed variables t and ξ were calculated by two smearing methods, directly, using a resolution function depending on each of these variables, or indirectly from the scattering angles θ_x^* and θ_y^*. Half the difference of the effect on the acceptance between the two methods was taken as a systematic uncertainty.
- **Horizontal dispersion:** The reconstructed ξ value depends on the optical functions describing the transport of the protons from the interaction vertex to the Roman Pot stations, in particular the horizontal dispersion. This uncertainty is calculated

scaling the value of ξ by $\pm 10\%$. This value corresponds to a conservative limit of the horizontal dispersion variation with respect to the nominal optics.

- **t-slope:** The sensitivity to the MC modeling of the exponential t-slope was quantified by changing its value in POMWIG by that measured from the data. Half the difference between the results was used as an uncertainty.

- **β-reweighting:** Half the difference in the results when removing the reweighting as a function of β in POMWIG was added as an uncertainty.

- **Acceptance and unfolding:** Half the maximum difference when the acceptance is recomputed with POMWIG, PYTHIA8 4C and PYTHIA8 CUETP8M1 for the single-diffractive cross sections and with PYTHIA6 Z2, PYTHIA8 4C, PYTHIA8 CUETP8M1 and PYTHIA8 CUETP8S1 for the inclusive dijet cross sections is taken as an additional uncertainty.

- **Unfolding regularisation:** The regularisation parameter used in the unfolding, given by the number of iterations in the D'Agostini iterative method (60) used in this analysis (see Sect. 4.4), was optimized by calculating the relative χ^2 variation between iterations. The value was chosen such that the χ^2 variation was below 5%. The number of iterations when the relative variation of χ^2 was below 2% was also calculated and half the difference from the nominal was taken as a systematic uncertainty.

- **Unfolding bias:** The MC sample, including all detector effects, is unfolded with a different model. The difference between the results with those at the particle level is an estimate of the bias introduced in the unfolding procedure (see Sect. 4.4). Half the maximum difference obtained when repeating the procedure with all MC combinations using POMWIG, PYTHIA8 4C and PYTHIA8 CUETP8M1 for the single-diffractive cross sections and PYTHIA6 Z2, PYTHIA8 4C, PYTHIA8 CUETP8M1 and PYTHIA8 CUETP8S1 for the inclusive dijet cross sections is taken as a systematic uncertainty.

- **Sector difference:** Half the difference in the results found by using events with the scattered proton in sector 45 only and in sector 56 only was taken as an additional uncertainty.

- **Luminosity:** The uncertainty on the integrated luminosity was taken as 4%, measured using a dedicated sample collected by TOTEM during the same data taking period (54).

The total systematic uncertainty was calculated as the quadratic sum of the individual contributions. The tables below summarize the effect of each contribution to the

Table 9 - Individual contributions of the different systematic effects to the measurement of the t and ξ cross sections for single-diffractive dijet production in the kinematic region of $p_T > 40$ GeV, $|\eta| < 4.4$, $\xi < 0.1$ and $0.03 < |t| < 1$ GeV^2.

Uncertainty source	$\Delta\sigma$(nb)		
	Sector 45	**Sector 56**	**Sectors average**
Trigger efficiency	±0.51	±0.51	±0.51
Jet energy scale	+1.92/-1.86	+1.95/-2.02	+1.95/-1.92
Calorimeter energy scale	+0.26/-0.32	+0.46/-0.39	+0.34/-0.37
Background	±0.21	±0.47	±0.33
RPs acceptance	±0.14	±0.16	±0.14
Beam divergence	±0.38	±0.31	±0.35
Horizontal dispersion	+1.66/-2.37	+2.61/-2.74	+2.12/-2.57
t-slope	±0.11	±0.11	±0.10
β-reweighting	±0.19	±0.14	±0.15
Acceptance and unfolding	±0.61	±0.31	±0.26
Unfolding regularisation	±0.09	±0.03	±0.06
Unfolding Bias	±1.22	±0.16	±0.63
Sector difference	±0.13	±0.13	±0.13
Total	+3.0/-3.4	+3.4/-3.5	+3.1/-3.4

Legend: The values correspond to the absolute variation of the cross section. The nominal values are $\sigma = 22.5 \pm 1.3$ nb and $\sigma = 22.8 \pm 1.5$ nb for sector 45 and 56 respectively. The total uncertainty is the quadratic sum of the individual contributions.
Source: The author, 2017.

measurements.

Table 9 summarises the effect of each contribution to the integrated single-diffractive cross section in t and ξ. Tables 10 and 11 present the effect of each contribution to the single-diffractive and inclusive dijet cross sections versus x, separately for sector 45 and sector 56, and the average between them.

The effect of the uncertainties on the ratio of the single-diffractive and inclusive dijet cross sections as a function of x is presented in Table 12. The ratio $R(x)$ is defined by:

$$R(x) = \frac{\sigma_{\mathrm{jj}}^{\mathrm{pX}}(x)/\Delta\xi}{\sigma_{\mathrm{jj}}(x)}, \tag{23}$$

where $\Delta\xi = 0.1$.

Figures 71 and 72 show the relative variations for each contribution to the t and ξ distributions, as well as for the ratio $R(x)$ as a function of $\log(x)$.

Table 10 - Individual contributions of the different systematic effects to the measurement of the inclusive dijet cross section, in the kinematic region of $p_T > 40$ GeV, $|\eta| < 4.4$ and $-3.2 \leq \log_{10} x \leq -1.3$.

Uncertainty source	$\Delta\sigma_{\text{jj}}$(nb)		
	Plus side	**Minus Side**	**Sectors average**
Trigger efficiency	±228.5	±229.8	±229.2
Jet energy scale	+693.9/-651.4	+703.8/-662.1	+698.9/-656.8
Calorimeter energy scale	±95.0	±94.2	±95.6
Acceptance and unfolding	±90.6	±101.0	±95.8
Unfolding bias	±167.5	±142.5	±155
Total	+760.9/-722.4	+766.5/-728.4	+763.7/-725.4

Legend: The values correspond to the absolute variation of the cross section. The nominal values are $\sigma = 10568.4 \pm 20.6$ nb and $\sigma = 10630.2 \pm 20.7$ nb when x refers to the incoming proton in the positive and negative z direction respectively. The total uncertainty is the quadratic sum of the individual contributions.
Source: The author, 2017.

Table 11 - Individual contributions of the different systematic effects to the measurement of the single-diffractive dijet cross section as a function of x in the kinematic region of $p_T > 40$ GeV, $|\eta| < 4.4$, $\xi < 0.1$, $0.03 < |t| < 1$ GeV^2 and $-3.2 \leq \log_{10} x \leq -1.3$.

Uncertainty source	$\Delta\sigma_{\text{jj}}^{pX}$(nb)		
	Sector 45	**Sector 56**	**Sectors average**
Trigger efficiency	±0.52	±0.54	±0.53
Jet energy scale	+1.80/-1.61	+1.71/-1.77	+1.83/-1.61
Calorimeter energy scale	+0.26/-0.32	+0.39/-0.33	+0.24/-0.41
Background	±0.71	±0.17	±0.48
RPs acceptance	±0.12	±0.16	±0.13
Beam divergence	±0.41	±0.36	±0.42
Horizontal dispersion	+1.54/-2.19	+2.43/-2.76	+1.91/-2.55
t-slope	±0.35	±0.35	±0.31
β-reweighting	±0.20	±0.19	±0.20
Acceptance and unfolding	±0.68	±0.08	±0.32
Unfolding regularisation	±0.01	±0.33	±0.17
Unfolding Bias	±1.15	±0.26	±0.71
Sector difference	±0.64	±0.64	±0.64
Total	+3.0/-3.3	+3.2/-3.5	+3.0/-3.3

Legend: The values correspond to the absolute variation of the cross section. The nominal values are $\sigma = 21.5 \pm 1.2$ nb and $\sigma = 22.8 \pm 1.4$ nb for sector 45 and 56 respectively. The total uncertainty is the quadratic sum of the individual contributions.
Source: The author, 2017.

Table 12 - Individual contributions of the different systematic effects to the measurement of the ratio of the single-diffractive and inclusive dijet cross sections in the region of $p_T > 40$ GeV, $|\eta| < 4.4$, $\xi < 0.1$, $0.03 < |t| < 1$ GeV^2 and $-3.2 \leq \log_{10} x \leq -1.3$.

Uncertainty source	ΔR		
	Sector 45	**Sector 56**	**Sectors average**
Trigger efficiency	±0.00005	±0.00004	±0.00005
Jet energy scale	+0.00034/-0.00028	+0.00017/-0.00035	+0.00030/-0.00028
Calorimeter energy scale	+0.00024/-0.00030	+0.00037/-0.00031	+0.00027/-0.00034
Background	±0.00068	±0.00016	±0.00044
RPs acceptance	±0.00012	±0.00015	±0.00012
Beam divergence	±0.00039	±0.00034	±0.00038
Horizontal dispersion	+0.00146/-0.00207	+0.00229/-0.00260	+0.00183/-0.00237
t-slope	±0.00033	±0.00033	±0.00031
β-reweighting	±0.00019	±0.00018	±0.00018
Acceptance and unfolding	±0.00047	±0.00025	±0.00017
Unfolding regularisation	±0.00001	±0.00031	±0.00006
Unfolding Bias	±0.00080	±0.00035	±0.00030
Sector difference	±0.00055	±0.00055	±0.00055
Total	+0.0021/-0.0025	+0.0025/-0.0028	+0.0021/-0.0026

Legend: The values correspond to the absolute variation of the ratio R. The nominal values are $R = 0.020 \pm 0.001$ and $R = 0.021 \pm 0.001$ for sector 45 and 56 respectively. The total uncertainty is the quadratic sum of the individual contributions.

Source: The author, 2017.

Figure 71 - Relative variation of each systematic uncertainty for events in sector 45.

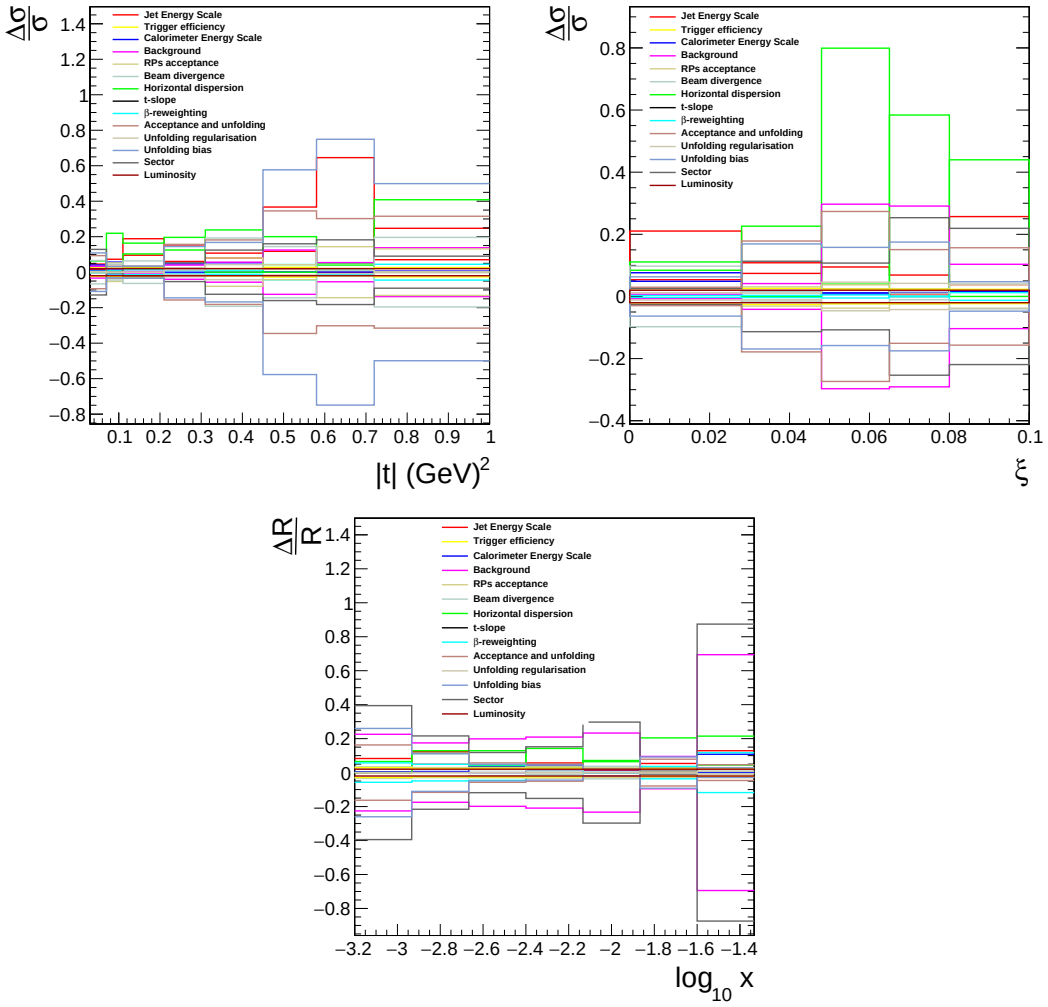

Legend: Top: Relative variation to the single-diffractive cross section as a function of t (left) and ξ (right). Bottom: Relative variation to the ratio of diffractive and inclusive cross sections as a function of $\log(x)$.

Source: The author, 2017.

Figure 72 - Relative variation of each systematic uncertainty for events in sector 56.

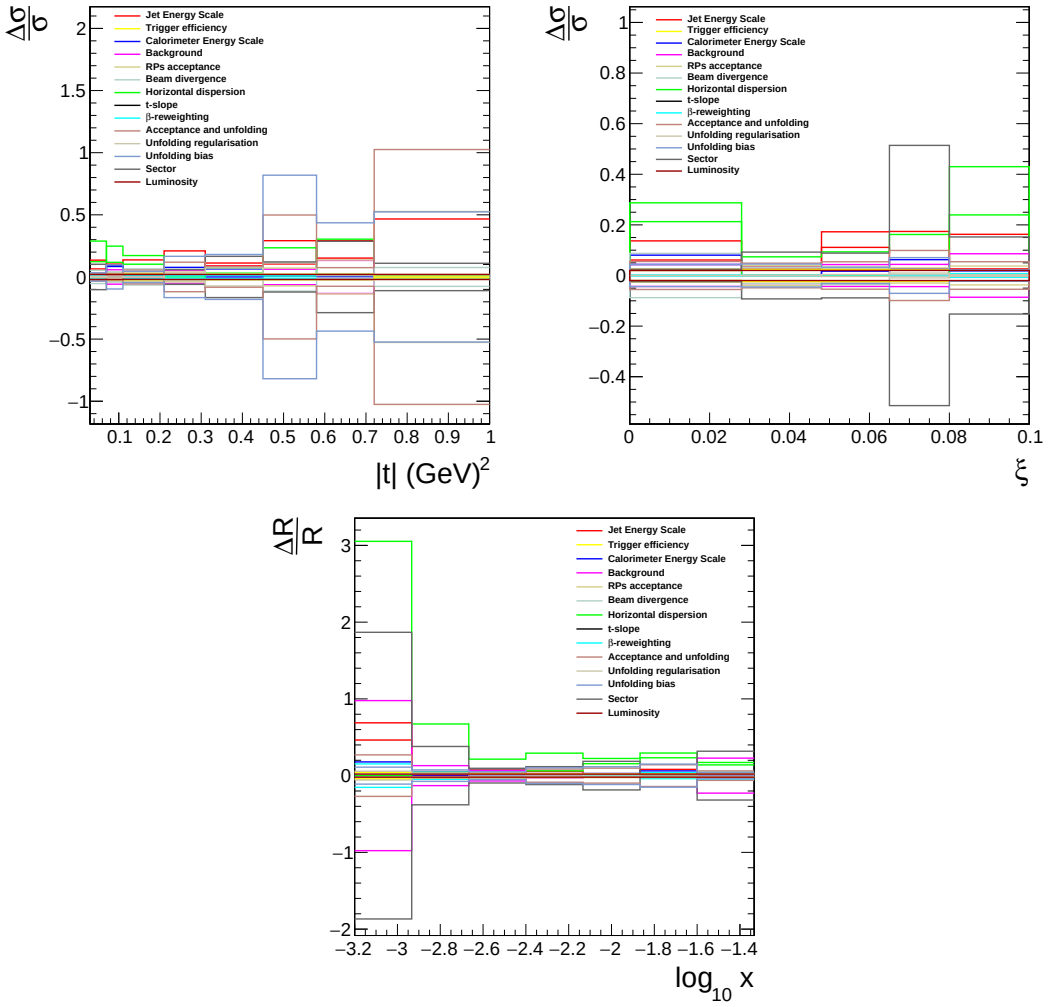

Legend: Top: Relative variation to the single-diffractive cross section as a function of t (left) and ξ (right). Bottom: Relative variation to the ratio of diffractive and inclusive cross sections as a function of $\log(x)$.

Source: The author, 2017.

5.2 Extraction of the cross section as a function of t and ξ

The differential cross sections for dijet production in bins of t and ξ were evaluated as:

$$\frac{d\sigma_{jj}}{dt} = \mathcal{U}\left\{\frac{N^i_{jj}}{\mathcal{L}A^i\Delta t^i}\right\} \qquad \frac{d\sigma_{jj}}{d\xi} = \mathcal{U}\left\{\frac{N^i_{jj}}{\mathcal{L}A^i\Delta \xi^i}\right\}, \tag{24}$$

where N^i_{jj} is the measured number of dijet events in the i-th bin, Δt^i and $\Delta\xi^i$ are the bin widths and $\mathcal{L}$ is the integrated luminosity. The factors A^i include the effects of the geometrical acceptance and efficiency of the apparatus. Unfolding corrections, represented by the symbol $\mathcal{U}$ in eq. 24, are applied to account for the finite resolution of the reconstructed variables used in the analysis. They are evaluated with POMWIG, PYTHIA8 4C and PYTHIA8 CUETP8M1. The average between the results is taken as the nominal value in the analysis.

The measured cross sections were obtained by unfolding the data using the D'Agostini iterative method with early stopping (60), implemented in the ROOUNFOLD package (62). In this method the regularisation parameter is the number of iterations used, which was optimized to obtain a relative χ^2 variation between iterations lower than 5% as described in Sec. 4.4.

The resulting cross sections as a function of t and ξ, for sectors 45 and 56 separately are shown in Figure 73. The data are compared to POMWIG, PYTHIA8 4C, PYTHIA8 CUETP8M1 and PYTHIA8 DYNAMIC GAP (DG). POMWIG is shown for two values of the suppresion of the diffractive cross section, i.e. the rapidity gap survival probability, represented by $\langle S^2\rangle$. When $\langle S^2\rangle = 1$, no correction is applied. The resulting cross sections are higher than the data by roughly an order of magnitude, in agreement with the Tevatron results (5; 6). POMWIG is also shown with the correction of $\langle S^2\rangle = 7.7\%$, which gives a good description of the data. POMWIG is shown in Fig. 73 as the sum of the Pomeron (pIP), Reggeon (pIR) and Pomeron-Pomeron (IPIP) exchange contributions while PYTHIA8 includes only the Pomeron (pIP) contribution. PYTHIA8 4C and PYTHIA8 CUETP8M1 show cross sections higher than the data by up to a factor of two. PYTHIA8 DYNAMIC GAP shows overall a good agreement with the data. No correction is applied to the normalisation of the PYTHIA8 samples.

The ratio of the data yields and the POMWIG predictions is shown in the bottom of the left and right panels of Fig. 73. No correction is applied for the rapidity gap survival probability ($\langle S^2\rangle = 1$).

The systematic uncertainties are also shown in the figures. Table 9 summarises the effect of each contribution to the integrated single-diffractive cross section. The average and maximum bin-by-bin variations for each contibution are shown in Appendix E.

Figure 73 - Differential cross section as a function of t (top) and ξ (bottom) for single-diffractive dijet production.

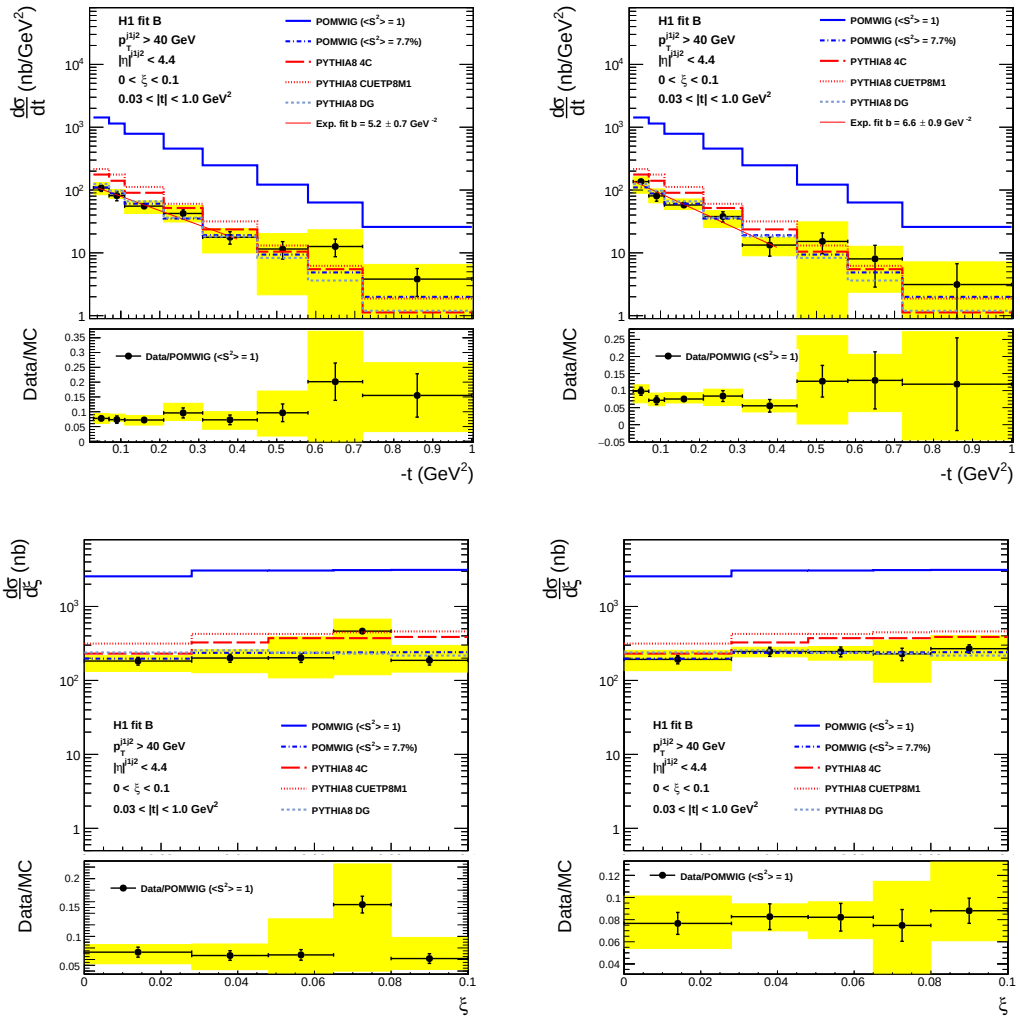

Legend: The data are compared to the predictions of Pomwig, Pythia8 4C, Pythia8 Cuetp8m1 and Pythia8 Dynamic Gap (DG). Pomwig is shown with no correction for the rapidity gap survival probability ($\langle S^2 \rangle = 1$) and with a correction of $\langle S^2 \rangle = 7.7\%$. The left panels show the results from the events in which the proton is detected in sector 45 and the right panels for the events with the proton in sector 56. The yellow band indicates the systematic uncertainty.

Source: The author, 2017.

Table 13 - Individual contributions of the different systematic effects to the measurement of the slope of the t distributions.

Uncertainty source	**Sector 45**		**Sector 56**		**Sectors Average**	
	Slope(GeV^{-2})	**Variation**	**Slope**(GeV^{-2})	**Variation**	**Slope**(GeV^{-2})	**Variation**
Trigger efficiency	5.35/5.34	±0.007	6.67/6.68	±0.002	6.00/6.00	±0.003
Jet energy scale	5.02/5.60	+0.23/-0.35	6.38/6.53	+0.22/-0.07	5.61/6.03	+0.21/-0.21
Calorimeter energy scale	5.10/5.16	+0.15/-0.09	6.78/6.61	+0.18/-0.01	5.82/5.80	+0.001/-0.02
Background	5.81	±0.28	6.97	±0.18	6.39	±0.29
RPs acceptance	5.43 - 5.35 - 5.32	±0.11	5.74 - 6.64 - 6.70	±0.10	6.05 - 5.94 - 5.95	±0.15
Beam divergence	3.98	±0.63	5.74	±0.43	4.83	±0.50
Horizontal dispersion	5.77/5.18	+0.53/-0.07	5.72/7.31	+0.88/-0.71	5.75/6.06	+0.07/-0.24
t-slope	5.34	±0.05	6.43	±0.09	5.80	±0.01
β-reweighting	5.31	±0.01	6.48	±0.03	5.82	±0.01
Acceptance and unfolding	5.76/4.95	±0.41	7.06/6.30	±0.38	6.17/5.75	±0.21
Unfolding regularisation	5.40	±0.08	6.90	±0.15	6.05	±0.11
Unfolding bias	5.10	±0.08	6.13	±0.37	5.42	±0.15
Sector difference	6.60 - 5.25	±0.68	6.60 - 5.25	±0.68	6.60 - 5.25	±0.68
Total		+1.2/-1.1		+1.4/-1.2		+1.0/-1.0

Source: The author, 2017.

The differential cross section as a function of t is well described by an exponential function for $|t|$ values up to $0.4-0.5$ GeV^2. A fit is performed with parametrisation given by $d\sigma/dt \propto \exp^{-b|t|}$, with $b = 5.2 \pm 0.7$ GeV^{-2} and $b = 6.6 \pm 0.9$ GeV^{-2}, respectively for events in which the proton is detected in sectors 45 and 56. The slope values for the MC are, $b = 5.39 \pm 0.03$ GeV^{-2} for POMWIG, $b = 6.11 \pm 0.12$ GeV^{-2} for PYTHIA8 4C, $b = 6.01 \pm 0.16$ GeV^{-2} for PYTHIA8 CUETP8M1 and $b = 5.88 \pm 0.48$ GeV^{-2} for PYTHIA8 DYNAMIC GAP (DG).

Figure 74 presents the result for the two sectors taken together. The resulting exponential slope of the cross section as a function of t is:

$$b = 5.8 \pm 0.5\,(\mathrm{stat}) \pm 1.0\,(\mathrm{syst})\ \mathrm{GeV}^{-2}, \tag{25}$$

where the systematic uncertainties include the contributions discussed in Section 5.1 and presented in Table 13.

The value of the cross section for single-diffractive dijet production calculated in the full kinematic region given by $p_T > 40$ GeV, $|\eta| < 4.4$, $\xi < 0.1$ and $0.03 < |t| < 1$ GeV^2 is:

$$\sigma_{\mathrm{jj}}^{\mathrm{pX}} = 22.6 \pm 1.0\,(\mathrm{stat})\,^{+3.1}_{-3.4}\,(\mathrm{syst}) \pm 0.9\,(\mathrm{lumi})\,\mathrm{nb}. \tag{26}$$

The ratio of the data yields and the POMWIG predictions is shown in the bottom of the left and right panels of Fig. 74; no correction is applied for the rapidity gap survival probability ($\langle S^2 \rangle = 1$). Within the uncertainties, no dependence on t and ξ is observed. The PYTHIA8 DYNAMIC GAP cross section in the same kinematic region is given by 23.7 nb, compatible with the result from Eq. 26.

The overall suppression factor can be obtained from the integrated cross section

Figure 74 - Differential cross section as a function of t (left) and as a function of ξ (right) for single-diffractive dijet production.

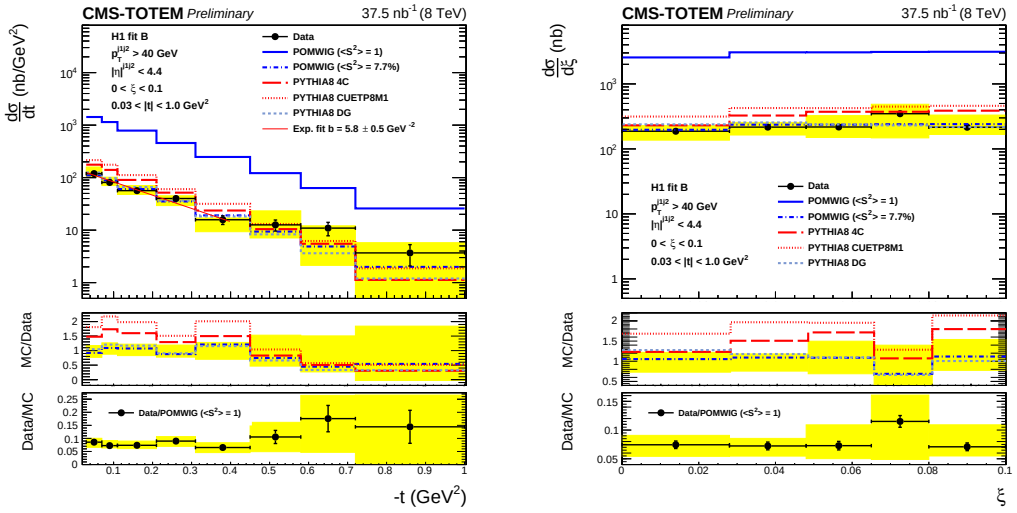

Legend: The data are compared to the predictions from POMWIG, PYTHIA8 4C, PYTHIA8 CUETP8M1 and PYTHIA8 DYNAMIC GAP (DG). POMWIG is shown with no correction for the rapidity gap survival probability ($\langle S^2 \rangle = 1$) and with a correction of $\langle S^2 \rangle = 7.7\%$. The yellow band indicates the total systematic uncertainty. The average of the results for events in which the proton is detected in either side of the interaction point is shown.
Source: The author, 2017.

in eq. 26 and the corresponding value from POMWIG and the PYTHIA8 hard diffraction model, when the DYNAMIC GAP framework is not applied (MPI-unchecked). This factor can be understood as an estimate of the suppression factor from the H1 dPDFs used in POMWIG and PYTHIA8.

The single-diffractive dijet cross section in the MC was calculated in the kinematic region defined above. Pomeron (p$\mathbb{P}$), Reggeon (p$\mathbb{R}$) and Pomeron-Pomeron ($\mathbb{P}\mathbb{P}$) contributions were included in POMWIG, with cross section values given by $\sigma_{\mathrm{p}\mathbb{P}} = 256$ nb, $\sigma_{\mathrm{p}\mathbb{R}} = 31$ nb and $\sigma_{\mathbb{P}\mathbb{P}} = 6.8$ nb respectively. In PYTHIA8 only the Pomeron-proton contribution is included, with cross section given by $\sigma_{\mathrm{p}\mathbb{P}} = 280$ nb. Reggeon exchange is not simulated in PYTHIA8. The overall data suppression with respect to the MC is given by:

$$\begin{aligned} \text{POMWIG}: &\quad \mathcal{S} = 0.077 \pm 0.003\,(\text{stat})\,^{+0.010}_{-0.012}\,(\text{syst}) \pm 0.003\,(\text{lumi}) \\ \text{PYTHIA8}: &\quad \mathcal{S} = 0.081 \pm 0.003\,(\text{stat})\,^{+0.011}_{-0.012}\,(\text{syst}) \pm 0.003\,(\text{lumi}). \end{aligned} \tag{27}$$

We do not include any uncertainty to account for the model dependence in the Monte Carlo reference value used to extract the suppression factor. POMWIG uses an LO matrix-element calculation. The cross section is expected to increase when using an NLO calculation, hence decreasing the value of $\mathcal{S}$ (18). The PYTHIA8 DYNAMIC GAP model

Figure 75 - Differential cross section as a function of t (left) and ξ (right) for single-diffractive dijet production when the results of the two sectors are averaged.

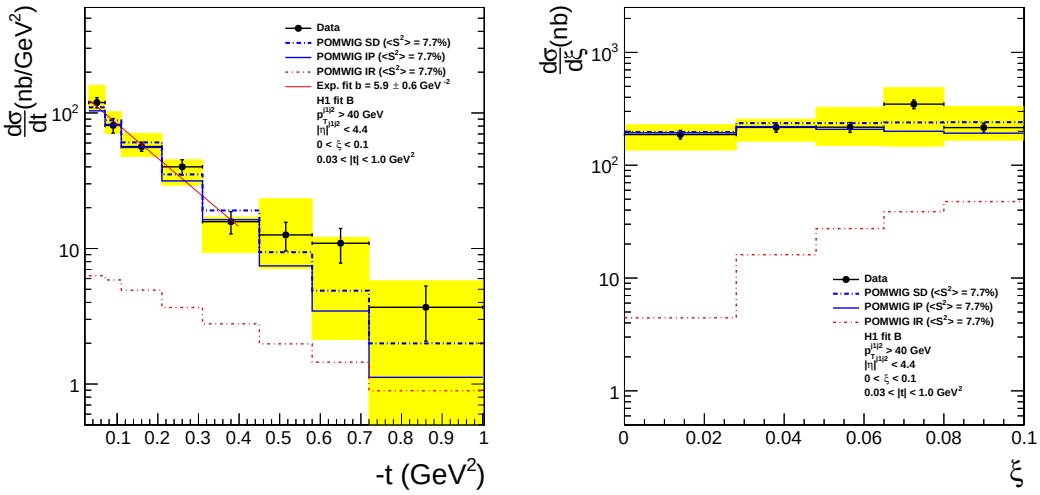

Legend: The data are compared to the POMWIG predictions. The Pomeron (IP) and Reggeon (IR) contributions from POMWIG are shown separately. POMWIG is shown with a correction of $\langle S^2 \rangle = 7.7\%$. The yellow band indicates the systematic uncertainty.
Source: The author, 2017.

suppression factor calculated in this kinematic region is $\mathcal{S} = 0.085$.

The H1 fit B dPDFs used in this analysis include the contribution from proton dissociation in ep collisions. They are extracted from the process ep $\rightarrow$ eXY, where Y can be a proton or a low-mass excitation such that $M_\mathrm{Y} < 1.6$ GeV (7). A comparison with the analogous analysis when the proton is detected yields consistent results apart from different overall normalisations, with relative ratio given by $\sigma\left(M_\mathrm{Y} < 1.6 \text{ GeV}\right) / \sigma\left(M_\mathrm{Y} = M_\mathrm{p}\right) = 1.23 \pm 0.03\,(\text{stat}) \pm 0.16\,(\text{syst})$ (7; 63). No dependence on β, Q^2 or ξ is observed.

In order to account for the different normalisation of the dPDF when a leading proton is detected ($M_\mathrm{Y} = M_\mathrm{p}$), the above normalisation ratio is used as a correction to $\mathcal{S}$, yielding the result:

$$\begin{aligned} \text{POMWIG}: &\quad \mathcal{S} = 0.095 \pm 0.003\,(\text{stat})\, ^{+0.013}_{-0.014}\,(\text{syst}) \pm 0.013\,(\text{pdf p-diss}) \pm 0.004\,(\text{lumi}) \\ \text{PYTHIA8}: &\quad \mathcal{S} = 0.099 \pm 0.003\,(\text{stat})\, ^{+0.014}_{-0.015}\,(\text{syst}) \pm 0.013\,(\text{pdf p-diss}) \pm 0.004\,(\text{lumi}). \end{aligned} \tag{28}$$

We explicitly show the uncertainty (pdf p-diss) from the dPDF normalisation correction. As in the previous case, no model-dependence uncertainty in the MC reference value used to obtain the suppression factor is included.

Figure 75 presents the cross section as a function of t and ξ compared with POMWIG, where the Pomeron and Reggeon contributions are shown separately.

Figure 76 - Distribution of ξ_{CMS} (left) and the differential cross section as a function of ξ for single-diffractive dijet production (right).

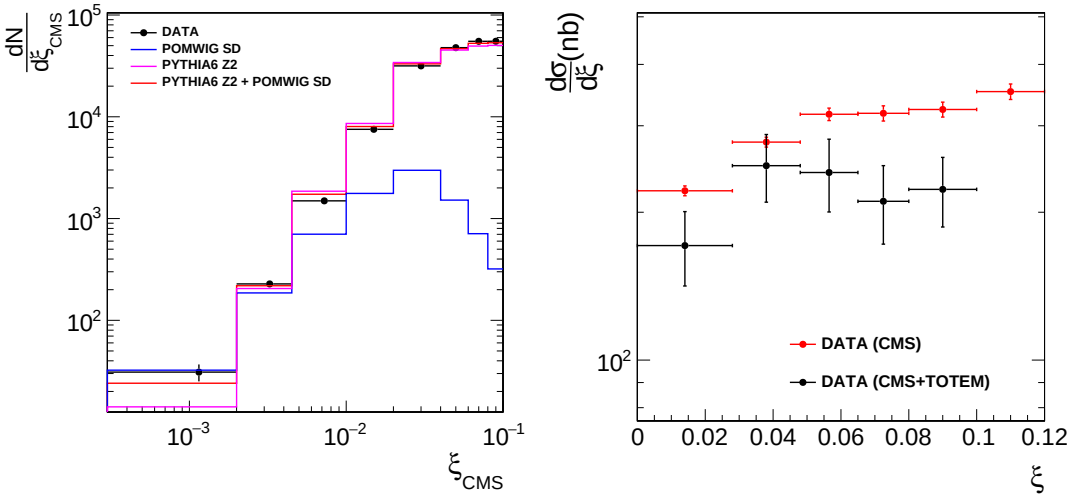

Legend: The left panel represent the distribution after the nominal selection with only CMS information, compared to the prediction of PYTHIA6 and POMWIG. The solid line represents the mixture of the diffractive and non-diffractive generators. The black points in the right panel represent the nominal result obtained after all selection cuts are applied. Red points are the result with CMS information only.
Source: The author, 2017.

5.2.1 Comparison to CMS-only analysis

The cross section for dijet production with transverse momentum $p_T > 20$ GeV at $\sqrt{s} = 7$ TeV as a function of ξ was measured in Ref. (18), based on CMS information only. Figure 76, right panel, shows the result obtained with the approach of Ref. (18) applied to the present data. The red points indicate the cross section as as function of ξ_{CMS} with no requirement on the scattered proton, and the black ones the cross section as a function of ξ_{TOTEM} given in Fig. 74. As was noted in Ref. (18), and also shown in Fig. 76 when ξ_{CMS} is small, the measured cross section is dominated by diffractive events. In the lowest ξ bin of Fig. 76 the two results differ by about a factor ~ 1.8. This difference could be due to a proton-dissociation contribution, i.e. events in which the proton dissociates into a low-mass state that escapes undetected. The inclusion of these events approximately doubles the visible single-diffractive cross section (18). A smaller contribution from non-diffractive events is also expected (18). At higher ξ values, the red points are dominated by non-diffractive events. The measurement of the proton suppresses this background very effectively.

In order to make a direct comparison of the result obtained by Ref. (18) with the previous result, the present data is extrapolated through the acceptance, which is calculated at reconstructed level with the nominal selection ($p_T > 40$ GeV and $|\eta| < 4.4$)

Figure 77 - Differential cross section as a function of ξ_{CMS} for single-diffractive dijet production.

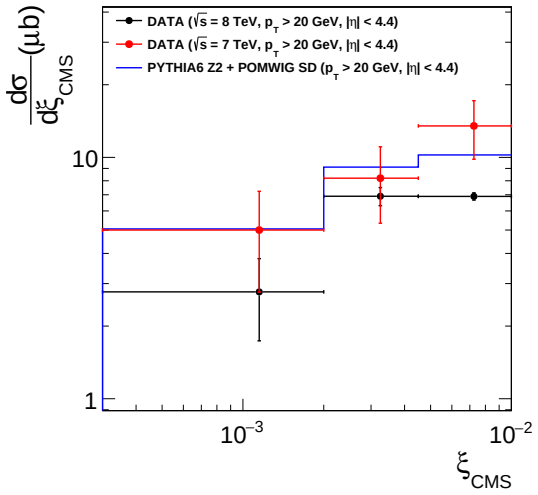

Legend: Black points represent the data based on CMS information only, extrapolated to the kinematic region of $p_T > 20$ GeV. Red points represent the results obtained by Ref. (18) at $\sqrt{s} = 7$ TeV. The solid line represents the mixture of the diffractive and non-diffractive generators.
Source: The author, 2017.

and at generator level selecting dijets with $p_T > 20$ GeV and $|\eta| < 4.4$. The result is shown in Figure 77, where the black points represent the extrapolation and the red ones represent the result obtained at $\sqrt{s} = 7$ TeV (Ref. (18)). In the region of low ξ (first bin in the figure), which is expected to be dominated by the diffractive contribution, the results differ by about a factor of ~ 1.5. No uncertainty to the results in Fig. 77 related to the extrapolation from the region defined by $p_T > 40$ GeV to the defined by $p_T > 20$ GeV has been estimated.

5.3 Extraction of the ratio of the single-diffractive to inclusive dijet yields

The ratio $R(x)$ of the single-diffractive to inclusive dijet cross sections is evaluated as a function of x as:

$$R(x) = \frac{\sigma_{\mathrm{jj}}^{\mathrm{pX}}(x)/\Delta\xi}{\sigma_{\mathrm{jj}}(x)} = \frac{\mathcal{U}\left\{N_{\mathrm{jj}}^{\mathrm{pX}}/A_{\text{CMS-TOTEM}}\right\}/\Delta\xi}{\mathcal{U}\left\{N_{\mathrm{jj}}/A_{\mathrm{CMS}}\right\}}, \tag{29}$$

where $N_{\mathrm{jj}}^{\mathrm{pX}}$ is the number of single-diffractive dijet candidates with $\xi_{\mathrm{TOTEM}} < 0.1$ discussed in the previous sections and N_{jj} is the total number of dijet events without the requirement of a proton selected in the RPs. This number is dominated by the non-diffractive contribution. $A_{\text{CMS-TOTEM}}$ indicates the acceptance of CMS and TOTEM for single-diffractive dijet events, evaluated with POMWIG, PYTHIA8 4C and PYTHIA8 CUETP8M1. A_{CMS} is

Figure 78 - Inclusive dijet cross section as a function of x.

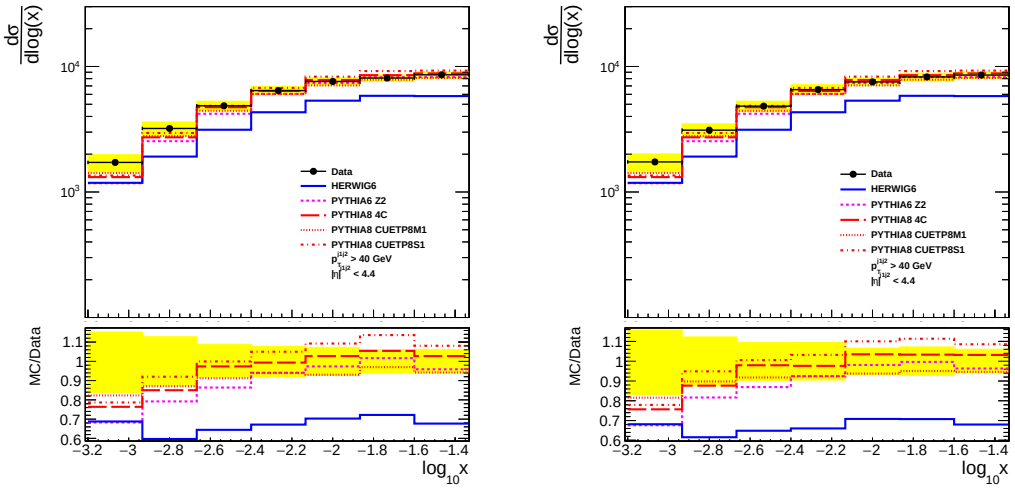

Legend: The data are compared with PYTHIA6, PYTHIA8 4C, PYTHIA8 CUETP8M1, PYTHIA8 CUETP8S1 and HERWIG6. The left panel refers to the incoming proton in the positive z direction and the right panel in the negative z direction. The yellow band represents the systematic uncertainties.
Source: The author, 2017.

the acceptance for non-diffractive dijet production, evaluated with PYTHIA6, PYTHIA8 4C, PYTHIA8 CUETP8M1, PYTHIA8 CUETP8S1 and HERWIG6. The acceptance includes unfolding corrections to the data by using the D'Agostini iterative method with early stopping, denoted by the symbol $\mathcal{U}$ in eq. 29.

The inclusive and single-diffractive dijet cross sections as a function of x are shown in Figs. 78 and 79 respectively. The systematic uncertainties are also shown in the figures as the yellow band. Each individual contribution is listed in Tables 10 and 11. The average and maximum bin-by-bin variations for each contibution are shown in Appendix E.

Figure 80 shows the ratio $R(x)$ for sectors 45 and 56 separately; the yellow band represents the systematic uncertainties listed in Table 12. The data are compared to the ratio of the single-diffractive and non-diffractive cross sections from different models. The single-diffractive contribution was simulated with POMWIG, PYTHIA8 4C, PYTHIA8 CUETP8M1 and PYTHIA8 DYNAMIC GAP (DG). The non-diffractive contribution was simulated with PYTHIA6 and HERWIG6 when POMWIG was used as the diffractive contribution. When using PYTHIA8 the diffractive and non-diffractive contributions are simulated with the same underlying event tune. When no correction factor is applied, POMWIG shows cross sections higher by roughly an order of magnitude, consistent with the results from Sect. 5.2. The supression seen in the data with respect to the MC ratio is not substantially different when using PYTHIA6 or HERWIG6 as the non-diffractive contribution. Using POMWIG with a correction of $\langle S^2 \rangle = 7.7\%$ gives overall a good agreement

Figure 79 - Single-diffractive dijet cross section as a function of $\log(x)$.

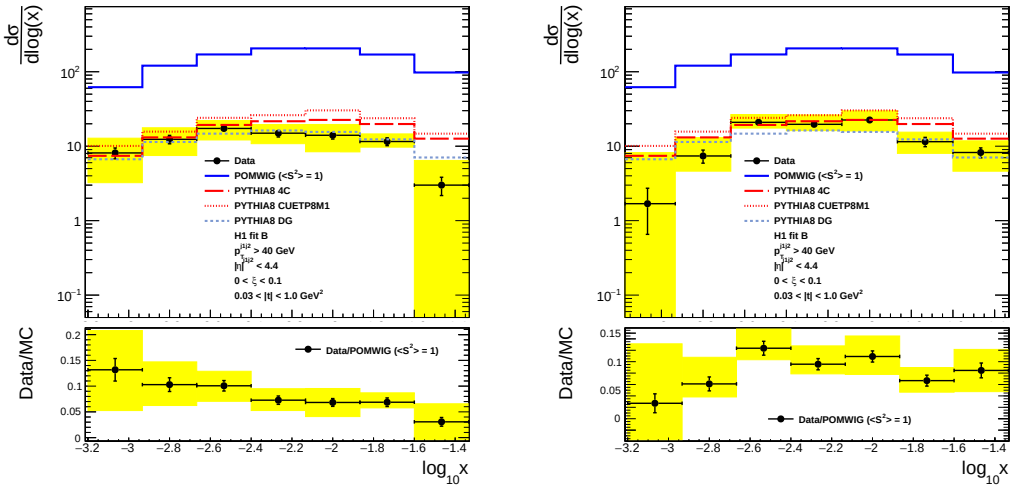

Legend: The data are compared with POMWIG, PYTHIA8 4C, PYTHIA8 CUETP8M1 and PYTHIA8 DYNAMIC GAP (DG), for events when the proton is detected in sector 45 (left) and when it is detected in sector 56 (right). The yellow band represents the systematic uncertainties.
Source: The author, 2017.

with the data. When HERWIG6 is used for the non-diffractive contribution, the agreement is worse in the higher-x region. POMWIG is shown as the sum of the Pomeron (pIP), Reggeon (pIR) and Pomeron-Pomeron (IPIP) exchange contributions while PYTHIA8 includes only the Pomeron (pIP) contribution. The agreement for PYTHIA8 4C and PYTHIA8 CUETP8M1 is fair in the intermediary x region while it is worse in the lower and higher-x regions. PYTHIA8 DYNAMIC GAP shows overall a good agreement with the data. No correction is applied to the PYTHIA8 normalisation. Figure 81 shows the results from the average of the two sectors.

The absolute value of the ratio in the full kinematic region given by $p_T > 40$ GeV, $|\eta| < 4.4$, $\xi < 0.1$, $0.03 < |t| < 1$ GeV^2 and $-3.2 \leq \log_{10} x \leq -1.3$ is:

$$R = (\sigma_{\mathrm{jj}}^{\mathrm{pX}}/\Delta\xi)/\sigma_{\mathrm{jj}} = 0.0209 \pm 0.0008\,(\mathrm{stat})\,^{+0.0021}_{-0.0026}\,(\mathrm{syst}). \tag{30}$$

The single-diffractive cross section thus corresponds to rougly $\sim 0.2\%$ of the dijet production cross section in this region.

Figure 82 compares the present data, averaged between the two sectors, with the results from CDF (6). The shape of the ratio is similar, but the present data are about a factor of two lower than the CDF results. A decrease of the ratio with centre-of-mass energy has also been observed by CDF by comparing their 630 and 1800 GeV data (39). The decrease of the ratio with $\sqrt{s}$ may reflect in part the decrease of the rapidity gap survival probability with $\sqrt{s}$, as expected theoretically (64).

Figure 80 - Ratio of the single-diffractive and inclusive dijet event yields in the region of $0.03 < |t| < 1$ GeV and $\xi < 0.1$ when the proton is detected in the RPs located in sector 45 (top panel) and 56 (bottom panel).

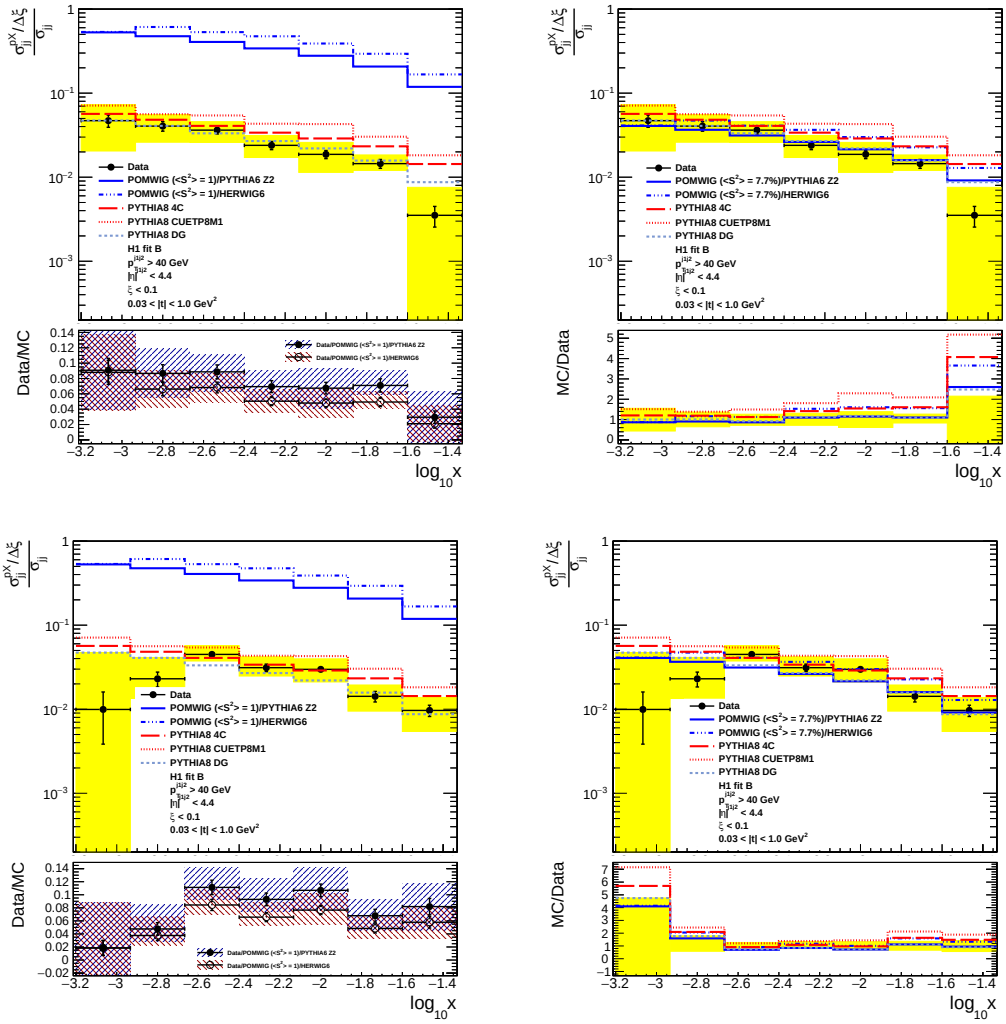

Legend: The ratio between the single-diffractive (Pomwig, Pythia8 4C, Pythia8 Cuetp8m1 and Pythia8 Dynamic Gap (DG)) and non-diffractive (Pythia6, Herwig6, Pythia8 4C and Pythia8 Cuetp8m1) predictions are also shown. Pomwig is shown with no correction for the rapidity gap survival probability ($\langle S^2 \rangle = 1$) (left) and with a correction of $\langle S^2 \rangle = 7.7\%$ (right). The yellow band indicates the systematic uncertainty.

Source: The author, 2017.

Figure 81 - Ratio of the single-diffractive and inclusive dijet cross sections in the region given by $\xi < 0.1$ and $0.03 < |t| < 1$ GeV^2.

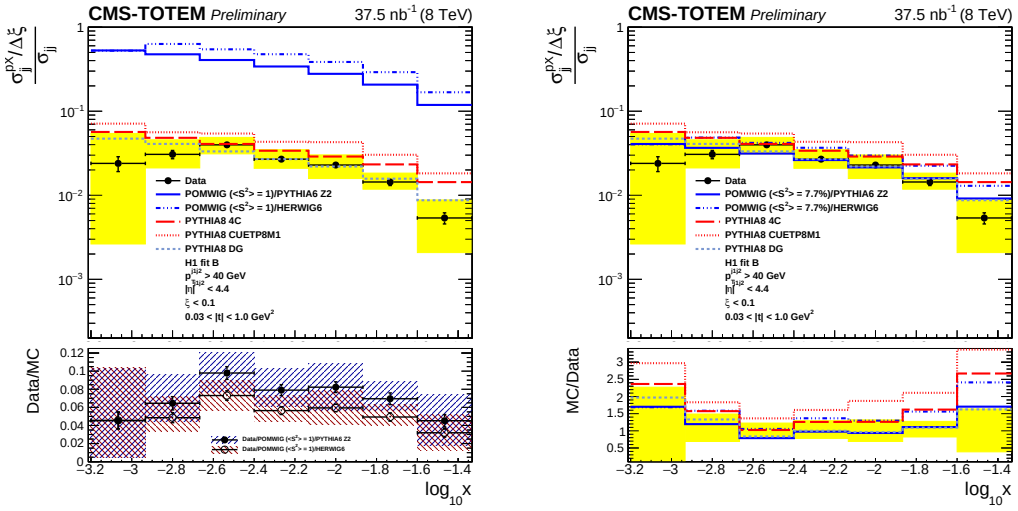

Legend: The ratio between the single-diffractive (POMWIG, PYTHIA8 4C, PYTHIA8 CUETP8M1 and PYTHIA8 DYNAMIC GAP (DG)) and non-diffractive (PYTHIA6, HERWIG6, PYTHIA8 4C and PYTHIA8 CUETP8M1) predictions are also shown. POMWIG is shown with no correction for the rapidity gap survival probability ($\langle S^2 \rangle = 1$) (left) and with a correction of $\langle S^2 \rangle = 7.7\%$ (right). The yellow band indicates the systematic uncertainty. The average of the results for events in which the proton is detected in either side of the interaction point is shown.

Source: The author, 2017.

Figure 82 - Ratio of the single-diffractive and inclusive dijet cross sections in the region of $0.03 < |t| < 1$ GeV^2 and $\xi < 0.1$.

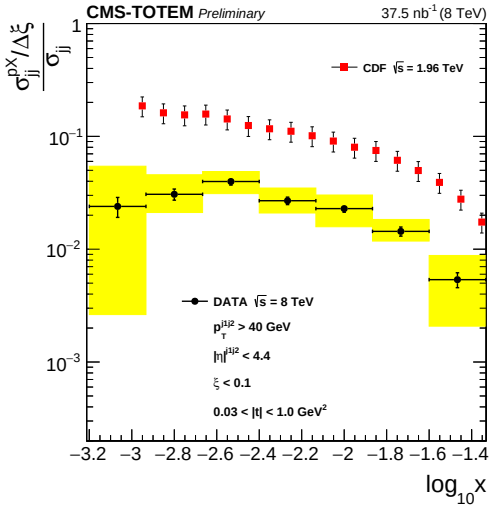

Legend: The results from events with a proton detected in sectors 45 and 56 were averaged, yielding the ratio represented by the black points. The red points represent the results obtained by CDF (6) at $\sqrt{s} = 1.96$ TeV in the kinematic region $0.03 < \xi < 0.09$ and $|t| < 1$ GeV^2.

Source: The author, 2017.

CONCLUSIONS

The differential cross section of single-diffractive dijet production at 8 TeV has been measured as a function of ξ and t using the CMS and TOTEM detectors. The data were collected using a non-standard optics configuration with $\beta^* = 90$ m and correspond to an integrated luminosity of 37.5 nb^{-1}.

This analysis is the first measurement of hard diffraction with a proton tagged at the LHC. A method based on data to estimate the background from beam-halo particles or protons from pileup events has been developed and successfully applied.

The propagation of the scattered protons inside the beam pipe and through the LHC magnets to the TOTEM Roman Pot stations was simulated by means of a parametrisation of the LHC optics and added to the Monte Carlo simulation of diffractive processes.

The considered processes are those of the type $pp \to Xp$ or $pp \to pX$, with X including a system of two jets in the kinematic region $\xi < 0.1$ and $0.03 < |t| < 1.0$ GeV^2. The two jets were measured with $p_T > 40$ GeV and $|\eta| < 4.4$. The integrated cross section in this kinematic region has been measured as $\sigma_{\text{jj}}^{\text{pX}} = 22.6 \pm 1.0\,(\text{stat})\,^{+3.1}_{-3.4}\,(\text{syst}) \pm 0.9\,(\text{lumi})$ nb. It corresponds to the average of the cross sections when the proton scatters to either side of the interaction.

The exponential slope of the cross section as a function of t has been measured as $b = 5.8 \pm 0.5\,(\text{stat}) \pm 1.0\,(\text{syst})$ GeV^{-2}.

The data are compared to the predictions from different hard-diffractive models. After accounting for a constant correction, related to the rapidity gap survival probability, Pomwig shows a good agreement with the data. The Pythia8 Dynamic Gap model describes well the data overall both in shape and normalisation within the uncertainties. This model treats in a novel way the effect of Multiple Partonic Interactions in hard-diffractive processes, leading to the suppression of hard-diffractive cross sections in pp collisions when using diffractive PDFs measured in ep collisions at HERA.

The ratio of the single-diffractive cross section and the corresponding value from either the Pomwig or Pythia8 Dynamic Gap predictions give an estimate of the suppression from the HERA dPDFs used in the analysis. After accounting for the correction in the dPDF normalisation due to proton dissociation, the suppression factors have been found in the range of $\mathcal{S} = 0.10 \pm 0.02$.

The Pythia8 inclusive diffractive model, without any direct assumption for the rapidity gap survival probability, gives a cross section higher than the data by up to a factor two.

The ratio of the single-diffractive to inclusive dijet cross sections has been measured as a function of the parton momentum fraction x. A decrease of the ratio is observed

when compared to the results from CDF at lower centre-of-mass energy. The overall ratio in the kinematic region given by $p_T > 40$ GeV, $|\eta| < 4.4$, $\xi < 0.1$, $0.03 < |t| < 1.0$ GeV^2 and $-3.2 \leq \log_{10} x \leq -1.3$ has been measured as $R = (\sigma_{\mathrm{jj}}^{\mathrm{pX}}/\Delta\xi)/\sigma_{\mathrm{jj}} = 0.0209 \pm 0.0008\,(\mathrm{stat})\,^{+0.0021}_{-0.0026}\,(\mathrm{syst})$.

REFERENCES

1 COLLINS, P. *Cambridge monographs on mathematical physics*: an introduction to Regge theory and high-energy Physics. Cambridge: Cambridge University Press, 2009.

2 UA8 COLLABORATION. Evidence for a superhard pomeron structure. *Physics Letters B*, [s.l.], v.297, p.417, 1992.

3 CDF COLLABORATION. Measurement of diffractive dijet produccion at the Fermilab Tevatron. *Physical Review Letters*, [s.l.], v.79, p.2636, 1997.

4 D0 COLLABORATION. Hard single diffraction in $\bar{p}p$ collisions at $\sqrt{s} = 630$ and 1800 GeV. *Physics Letters B*, [s.l.], v.531, p.52, 2002.

5 CDF COLLABORATION. Diffractive dijets with a leading antiproton in $\bar{p}p$ collisions at $\sqrt{s} = 1800$ GeV. *Physical Review Letters*, [s.l.], v.84, p.5043, 2000.

6 CDF COLLABORATION. Diffractive dijet production in $p\bar{p}$ collisions at $\sqrt{s} = 1.96$ TeV. *Physical Review D*, [s.l.], v.86, p.032009, 2012.

7 H1 COLLABORATION. Measurement and QCD analysis of the diffractive deep-inelastic sacttering cross-section at HERA. *Europhysics Letters*, Bristol, [s.l.], v.48, p.715, 2006.

8 ZEUS COLLABORATION. Deep inelastic scattering with leading protons or large rapidity gaps at HERA. *Nuclear Physics B*, New York, [s.l.], v.816, p.1–61, 2009.

9 ZEUS COLLABORATION. A QCD analysis of ZEUS diffractive data. *Nuclear Physics B*, [s.l.], v.831, p.1-25, 2010.

10 H1 COLLABORATION. Diffractive dijet photoproduction in ep collisions at HERA. *The European Physical Journal C*, [s.l.], v.70, p.15, 2010.

11 TRENTADUNE, L.; VENEZIANO, G. Fracture functions. An improved description of inclusive hard processes in QCD. *Physics Letters B*, [s.l.], v.323, p.201, 1994.

12 COLLINS, J. Proof of factorization for diffractive hard scattering. *Physical Review D*, [s.l.], v.57, p.3051, 1998.

13 GRAZZINI, M.; TRENTADUNE, L.; VENEZIANO, G. Fracture functions from CUT vertices. *Nuclear Physics B*, [s.l.], v.519, p.394, 1998.

14 BJORKEN, J.D. Rapidity gaps and jets as a new-physics signature in very-high-energy hadron-hadron collisions. *Physical Review D*, [s.l.], New York, v.47, p.101-113, 1993.

15 CMS COLLABORATION. The CMS experiment at the CERN LHC. *JINST*, [s.l.], v.03, 2008.

16 TOTEM COLLABORATION. The TOTEM Experiment at the CERN Large Hadron Collider. *JINST*, [s.l.], v.3 S08007, 2008.

17 TOTEM COLLABORATION. Performance of the TOTEM detectors at the LHC. *JINST*, [s.l.], v.28, 2013.

18 CMS COLLABORATION. Observation of a diffractive contribution to dijet production in proton-proton collisions at $\sqrt{s} = 7$ TeV. *Physical Review D*, New York, v.87, p.012006, 2013.

19 BARONE, V.; PREDAZZI, E. *High-energy particle diffraction.* Berlin: Springer, 2002, 423p.

20 HEBECKER, A. Diffraction in deep inelastic scattering. *Phys. Rept.*, [s.l.], v.331, 2000.

21 PREDAZZI, E. Diffraction: retrospectives and perspectives. *Nuclear Physics B:* Proceedings Supplements, New York, v.99, p.3-6, 2001.

22 DESGROLARD, P.; GIFFON, M.; MARTYNOV, E.; PREDAZZI, E. Exchange-degenerate regge trajectories: a fresh look from resonance and forward scattering regions. *The European Physical Journal C*, [s.l.], v.18, p.555-561, 2001.

23 TOTEM COLLABORATION. Luminosity independent measurements of total, elastic and inelastic cross sections at $\sqrt{s} = 7$ TeV. *Europhysics Letters*, Bristol, v.101, p.21004, 2013.

24 DONNACHIE, A.; LANDSHOFF, P. V. Total cross-sections. *Physics Letters B*, Dorchester, v.296, p.227–232, 1992.

25 DOLEN, R.; HORN, S.; SCHMID, C. Finite energy sum rules and their application to πN charge exchange. *Physical Review*, [s.l.], v.166, p.1768-1781, 1968.

26 COHEN-TANNOUDJI, G.; SANTORO, A.; SOUZA, M. Duality and mass - slope correlation in diffractive dissociations. *Nuclear Physics*, [s.l.], v.125, p.445, 1977.

27 VENEZIANO,G. Construction of a crossing-symmetric, Regge behaved amplitude for linearly rising trajectories. *Nuovo Cimento*, [s.l.], v.57, p.190-197, 1968.

28 ENDLER, A.; REGO, M.; SANTORO, A.; SOUZA, M. Application of the Three-Component-Dual-Deck-Model to the ΛK channel in pp reaction. *Z. Physics C - Particles and Fields*, [s.l.], v.7, p.137-141, 1981.

29 HAYOT, F.; MOREL, A.; SANTORO, A.; SOUZA, M. Deck model and mass-slope correlations. *Letters Nuovo Cimento*, [s.l.], v.18, p.185-188, 1977.

30 ANJOS, J.; LEVY, D.; SANTORO, A. A deck like model for the 'ABC' producction in the $pn \to d(\pi\phi)^\circ$ reaction. *Nuovo Cimento A*, [s.l.], v.33, p.23-46, 1976.

31 INGELMAN, G.; SCHLEIN, P. Jet structure in high mass diffractive scattering. *Physics Letters B*, Dorchester, v.152, p.256-260, 1985.

32 BONINO, R. et al. Evidence for transverse jets in high-mass diffraction. *Physics Letters B*, Dorchester, v.211, p.239-246, 1988.

33 AHMED, T. et al. First measurement of the deep-inelastic structure of proton diffraction DESY. *Physics Letters B*, Dorchester, v.348, p.681-696, 1995.

34 DERRICK, M. et al. Observation of jet production in deep inelastic scattering with a large rapidity gap at HERA. *Physics Letters B*, Dorchester, v.332, p.228-243, 1994.

35 DERRICK, M. et al. Observation of hard scattering in photoproduction events with a large rapidity gap at HERA. *Physics Letters B*, Dorchester, v.346, p.399-414, 1995.

36 COLLINS, J. *Foundations of perturbaive QCD*. Cambridge: Cambridge University Press, 2011.

37 CDF COLLABORATION. The diffractive structure function at the Tevatron: CDF. *Nuclear Physics B*, [s.l.], v.99, p.37-46, 2001.

38 CDF COLLABORATION. CDF experimental results on diffraction. Disponível em: <arXiv:0904.2098, 2009>. Acesso em: 27 feb. 2016.

39 CDF COLLABORATION. Diffractive dijet production at $\sqrt{s}$=630 and $\sqrt{s}$=1800 GeV at the Fermilab Tevatron. *Phys. Rev. Lett.*, [s.l.], v.88, p.151802, 2002.

40 EVANS, L.; BRYANT, P. LHC Machine. *JINST*, [s.l.], v.3, 2008.

41 CMS COLLABORATION. Performance of photon reconstruction and identification with the CMS detector in proton-proton collisions at $\sqrt{s} = 8$ TeV. *JINST*, [s.l.], v.10, 2015.

42 SJOSTRAND, T.; MRENNA, S.; SKANDS, P. PYTHIA 6.4 physics and manual. *JHEP*, [s.l.], v.05, p.026, 2006.

43 SJOSTRAND, T.; MRENNA, S.; SKANDS, P. A Brief Introduction to PYTHIA 8.1. *Comput. Physics Commun*, Dorchester, v.178, p.852-867, 2008.

44 CORCELLA, G.; et al. HERWIG6: An event generator for hadron emission reactions with interfering gluons (including supersymmetric processes). *JHEP*, [s.l.], v.101, p.010, 2001.

45 COX, B. E.; FORSHAW J. R. Pomwig: Herwig for diffractive interactions. *Comput. Physics Commun*, Dorchester, v.144, p.104-110, 2002.

46 BENGTSSON, H.; SJOSTRAND, T. The Lund Monte Carlo for hadronic processes: Pythia Version 4.8. *Comput. Physics Commun*, [s.l.], v.46, p.43, 1987.

47 FIELD, R. Early LHC underlying event data - findings and surprises. Disponível em: <arXiv:hep-ph/1010.3558, 2010>. Acesso em: 20 jan. 2017.

48 KHACHATRYAN, V. Event generator tunes obtained from underlying event and multiparton scattering measurements. *Eur. Physics Journal*, [s.l.], v.C76, p.155, 2016.

49 RASMUSSEN, C. O.; SJSTRAND, T. Hard diffraction with dynamic gap survival. *JHEP*, [s.l.], v.02, p.142, 2016.

50 GEANT4 COLLABORATION. Geant4-a simulation toolkit. *Nucl. Instrum. Meth. A*, [s.l.], v.506, p.250, 2003.

51 TOTEM COLLABORATION. LHC optics determination with proton tracks measured

in the Roman Pots detectors of the TOTEM experiment. *New J. Phys.*, [s.l.], v.16, p.103041, 2014.

52 TOTEM COLLABORATION. *Acceptance calculations methods for low-β^* optics.* CMS Physics Analysis Summary, CMS-TOTEM-NOTE, 2006.

53 KASPAR, J. *Description and simulation of beam smearing effects.* CMS Physics Analysis Summary, CMS-TOTEM-NOTE-2007-005, 2007.

54 TOTEM COLLABORATION. Evidence for non-exponential elastic proton-proton differential cross-section at low $|t|$ and $\sqrt{s} = 8$ TeV by TOTEM. *Nucl. Phys. B*, [s.l.], v.899, p.527-546, 2015.

55 TOTEM COLLABORATION. Luminosity-Independent Measurement of the Proton-Proton Total Cross Section at $\sqrt{s} = 8$ TeV. *Phys. Rev. Lett.*, [s.l.], v.111, p.012001, 2013.

56 CACCIARI, M.; SALAM, G.P.; SOYEZ, G. The anti-k_t jet clustering algorithm. *JHEP*, [s.l.], v.04, p.063, 2008.

57 CMS COLLABORATION. Particle-flow reconstruction and global event description with the CMS detector. Disponível em: <arXiv:1706.04965, 2017>. Acesso em: 02 feb. 2014.

58 CMS COLLABORATION. Jet energy scale and resolution in the CMS experiment in pp collisions at 8 TeV. *JINST*, [s.l.], v.12, p.02014, 2017.

59 TOTEM COLLABORATION. Measurement of proton-proton elastic scattering and total cross-section at $\sqrt{s} = 7$ TeV. *Europhys. Lett.*, [s.l.], v.101, p.21002.

60 D'AGOSTINI, G. A multidimensional unfolding method based on Bayes' theorem. *Nucl. Instr. Meth. A*, Dorchester, v.362, p.487-498, 2006.

61 MULTHEI, H.; SCHORR, B. On an iterative method for the unfolding of spectra. *Nucl. Instr. Meth. A*, Dorchester, v.257, p.371, 1987.

62 ADYE, T. Unfolding algorithms and tests using RooUnfold. In: PHYSTAT 2011 WORKSHOP ON STATISTICAL ISSUES RELATED TO DISCOVERY CLAIMS IN SEARCH EXPERIMENTS AND UNFOLDING, 2011, Genève. *Proceedings...* PHYSTAT 2011 Workshop on Statistical Issues Related to Discovery Claims in Search Experiments and Unfolding. Geneva: CERN, 2011. p.313-318.

63 H1 COLLABORATION. Diffractive deep-inelastic scattering with a leading proton at HERA. *Eur. Phys. J.*, [s.l.], v.C48, p.749-766, 1995.

64 KHOZE, V.; MARTIN, A.; RYSKIN, M. The extraction of the bare triple-Pomeron vertex; a crucial ingredient for diffraction. *Phys. Lett. B*, [s.l.], v.643, p.93, 2006.

APPENDIX A – Particle Flow thresholds

To select good reconstructed events and reduce the effect of the background in the analysis, energy threholds are applied to the PF objects.

From the zero-bias data the energy of each PF object is measured. Events were classified according to n_{dof} vertex cut. A signal event comes from a good reconstructed vertex with $n_{dof} \geq 4$. A vertex with bad quality is defined when $n_{dof} < 4$, and no vertex is found when $n_{dof} = 0$.

Figures 83, 84, 85, 86 show the energy distribution for the PF objects in each detector region: Barrel, Endcap, Transition and Forward. The values (Table 7) were chosen in order to reject most of the events with not a good reconstructed vertex.

Figure 83 - Distributions of energy for the PF Gamma particle.

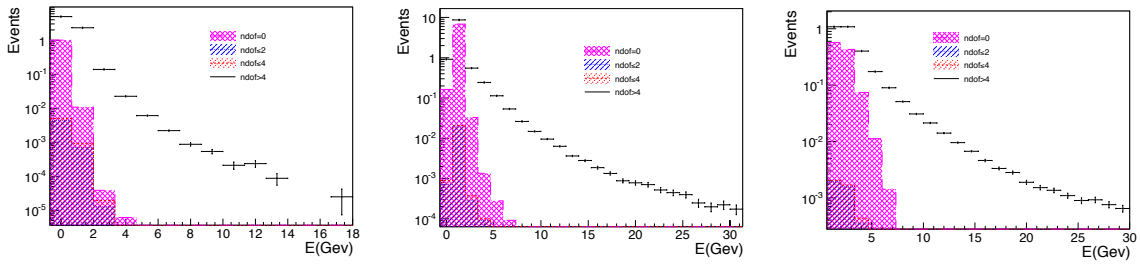

Legend: The distributions are shown for the detector regions: barrel (left panel), endcap (central panel) and transition (right panel). Each plot show the distributions for $n_{dof} = 0$, $n_{dof} < 2$, $n_{dof} < 4$ and $n_{dof} \geq 4$.
Source: The author, 2017.

Figure 84 - Distributions of energy for the PF Neutral Hadron particle.

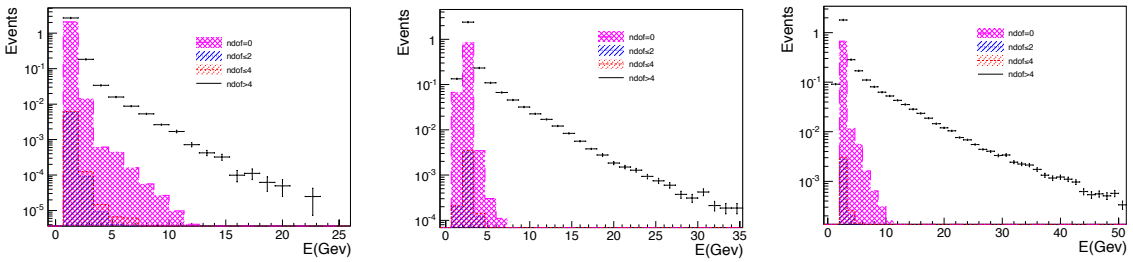

Legend: The distributions are shown for the detector regions: barrel (left panel), endcap (central panel) and transition (right panel). Each plot show the distributions for $n_{dof} = 0$, $n_{dof} < 2$, $n_{dof} < 4$ and $n_{dof} \geq 4$.
Source: The author, 2017.

Figure 85 - Distributions of energy for the PF Gamma HF particle.

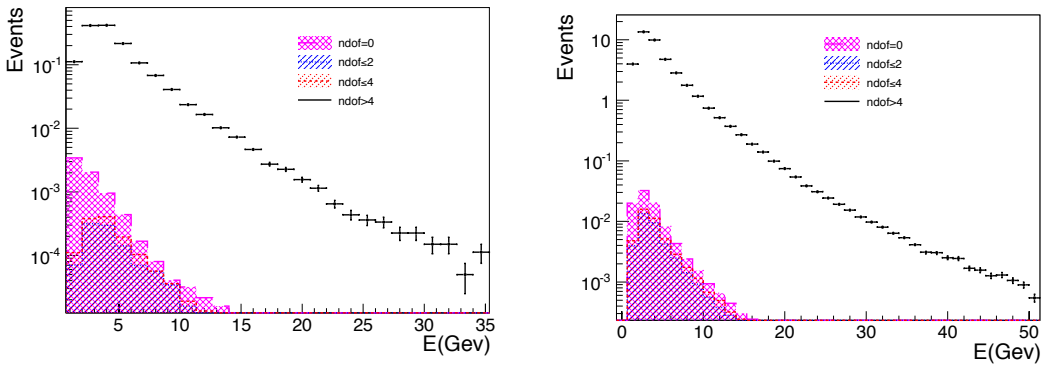

Legend: The distributions are shown for the detector regions: transition (left panel) and forward (right panel). Each plot show the distributions for $n_{dof} = 0$, $n_{dof} < 2$, $n_{dof} < 4$ and $n_{dof} \geq 4$.
Source: The author, 2017.

Figure 86 - Distributions of energy for the PF Hadron HF particle.

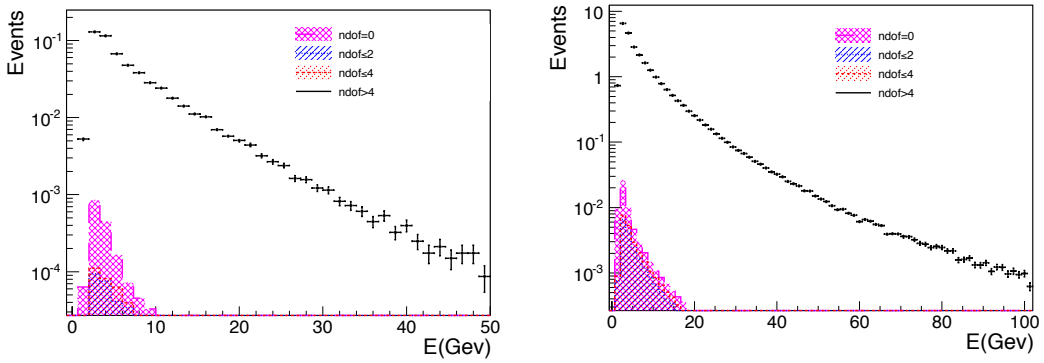

Legend: The distributions are shown for the detector regions: transition (left panel) and forward (right panel). Each plot show the distributions for $n_{dof} = 0$, $n_{dof} < 2$, $n_{dof} < 4$ and $n_{dof} \geq 4$.
Source: The author, 2017.

APPENDIX B – Effect of the reweighting on the generators

In Section 3 the reweighting as a function of β was discussed. The correction to the b slope of the data was also described previously. These weights were applied to the generator in order to improve the description of the data. The next figures show the effect of each correction applied to the MC.

Figures 87 and 88 present the effect of each correction applied to POMWIG for sector 45 and 56 respectively, Fig. 89 and 90 present the results for PYTHIA8. The figures compare the distributions when no correction is applied to the MC, when the β reweighting is applied and when both β and b slope corrections are applied at the same time.

The comparison between the two sectors with POMWIG events, when no correction is applied to the MC, when the β reweighting is applied and when both β and b slope corrections are applied at the same time are presented in Figures 91, 92 and 93, respectively. The same comparison is presented in Figures 94, 95 and 96 for PYTHIA8.

Figure 87 - Cross sections as a function of t and ξ, as well as the ratio of the single-diffractive and non-diffractive event yields.

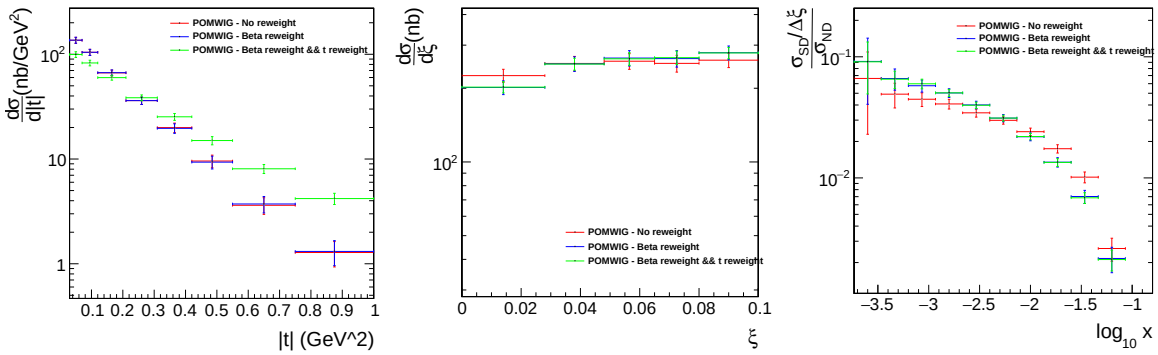

Legend: The distributions compare the effect of the reweighting for events in which the proton is detected in sector 45 using POMWIG. The MC is shown without reweighting (red points), with the reweighting in β only (blue points) and with the reweighting in β and in the b-slope (black points).
Source: The author, 2017.

Figure 88 - Cross sections as a function of t and ξ, as well as the ratio of the single-diffractive and non-diffractive event yields.

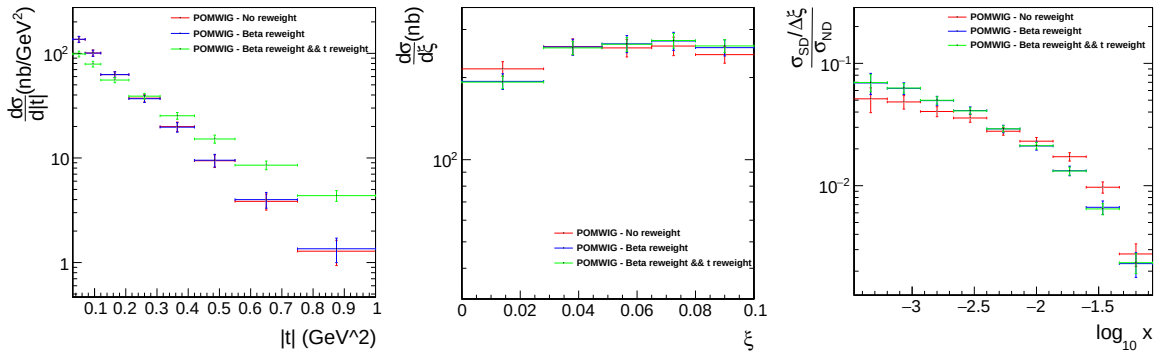

Legend: The distributions compare the effect of the reweighting for events in which the proton is detected in sector 56 using POMWIG. The MC is shown without reweighting (red points), with the reweighting in beta only (blue points) and with the reweighting in beta and in the b-slope (black points).
Source: The author, 2017.

Figure 89 - Cross sections as a function of t and ξ, as well as the ratio of the single-diffractive and non-diffractive event yields.

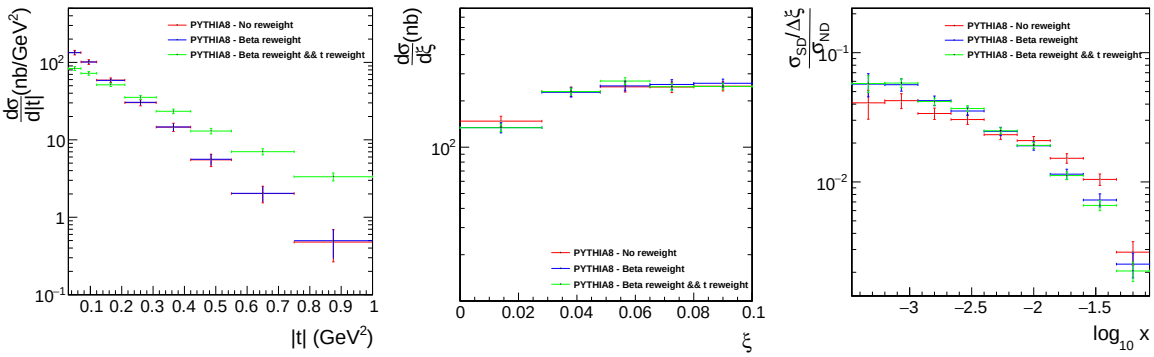

Legend: The distributions compare the effect of the reweighting for events in which the proton is detected in sector 45 using POMWIG. The MC is shown without reweighting (red points), with the reweighting in beta only (blue points) and with the reweighting in beta and in the b-slope (black points).
Source: The author, 2017.

Figure 90 - Cross sections as a function of t and ξ, as well as the ratio of the single-diffractive and non-diffractive event yields.

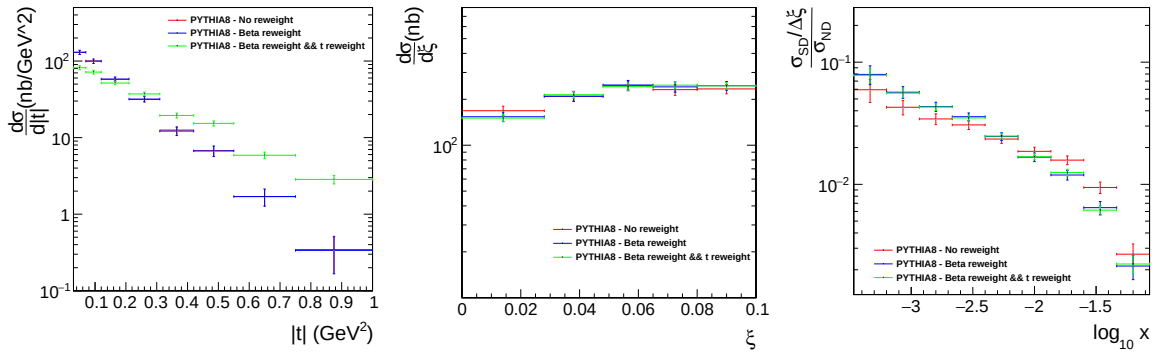

Legend: The distributions compare the effect of the reweighting for events in which the proton is detected in sector 56 using POMWIG. The MC is shown without reweighting (red points), with the reweighting in beta only (blue points) and with the reweighting in beta and in the b-slope (black points).
Source: The author, 2017.

Figure 91 - Cross sections as a function of t and ξ, as well as the ratio of the single-diffractive and non-diffractive event yields.

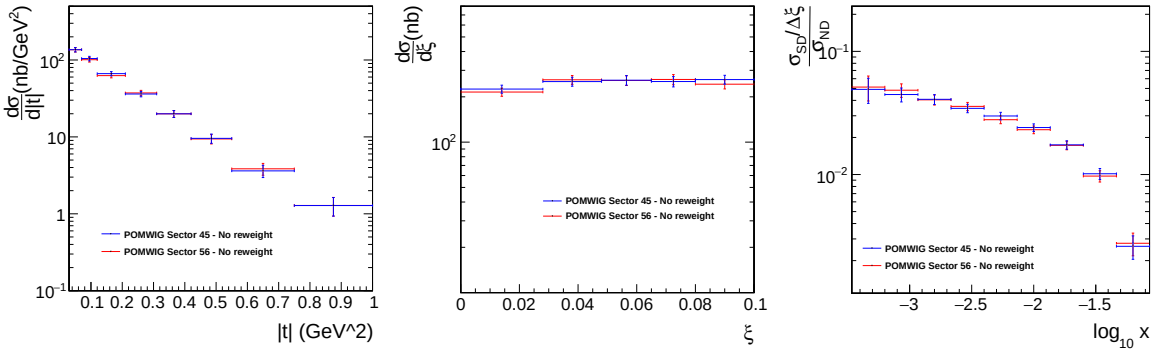

Legend: The distributions compare the results for both sectors using POMWIG. The MC is shown without reweighting. Blue points represent the results when the proton is detected in sector 45 and the red points when it is detected in sector 56.
Source: The author, 2017.

Figure 92 - Cross sections as a function of t and ξ, as well as the ratio of the single-diffractive and non-diffractive event yields.

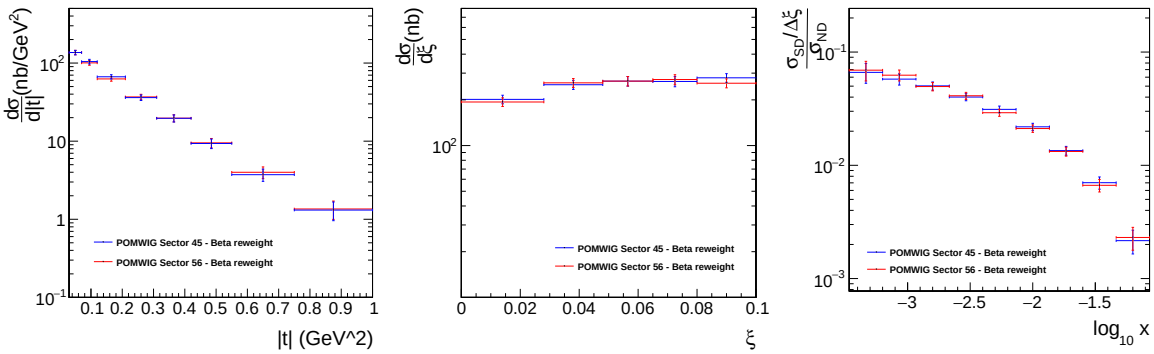

Legend: The distributions compare the results for both sectors using POMWIG. The MC is shown with the reweighting in beta. Blue points represent the results when the proton is detected in sector 45 and the red points when it is detected in sector 56.
Source: The author, 2017.

Figure 93 - Cross sections as a function of t and ξ, as well as the ratio of the single-diffractive and non-diffractive event yields.

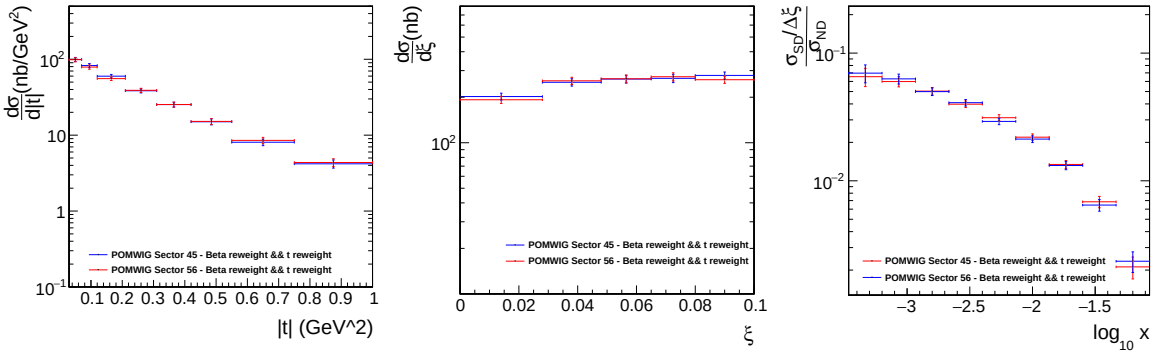

Legend: The distributions compare the results for both sectors on the generator POMWIG. The MC is shown with the reweighting in β and b-slope. Blue points represent the results when the proton is detected in sector 45 and the red points when it is detected in sector 56.
Source: The author, 2017.

Figure 94 - Cross sections as a function of t and ξ, as well as the ratio of the single-diffractive and non-diffractive event yields.

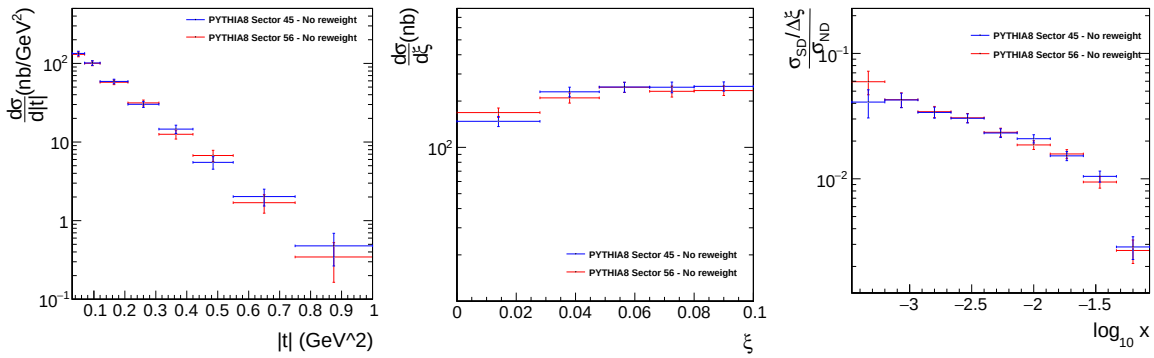

Legend: The distributions compare the results for both sectors using PYTHIA8. The MC is shown without reweighting. Red points represent the results when the proton is detected in sector 45 and the blue points when it is detected in sector 56.
Source: The author, 2017.

Figure 95 - Cross sections as a function of t and ξ, as well as the ratio of the single-diffractive and non-diffractive event yields.

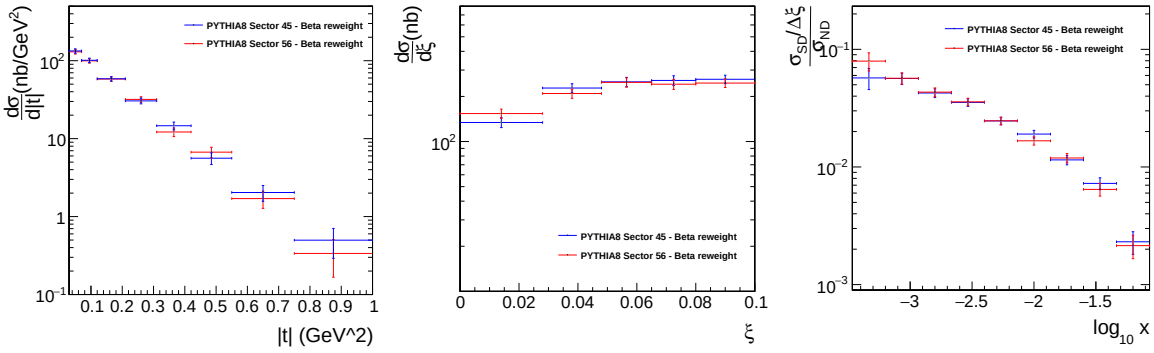

Legend: The distributions compare the results for both sectors using PYTHIA8. The MC is shown with the reweighting in beta. Red points represent the results when the proton is detected in sector 45 and the blue points when it is detected in sector 56.
Source: The author, 2017.

Figure 96 - Cross sections as a function of t and ξ, as well as the ratio of the single-diffractive and non-diffractive event yields.

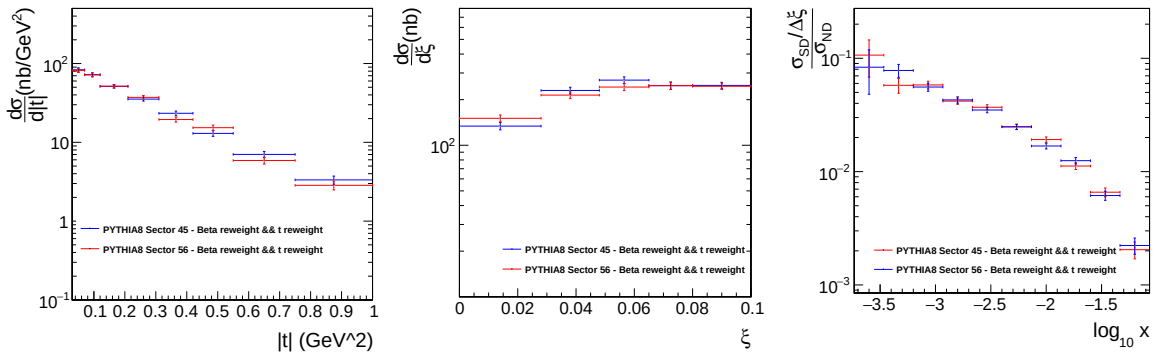

Legend: The distributions compare the results for both sectors using PYTHIA8. The MC is shown with the reweighting in beta and b-slope. Red points represent the results when the proton is detected in sector 45 and the blue points when it is detected in sector 56.
Source: The author, 2017.

APPENDIX C – p_T threshold in t distribution

This section describes the effect of the jets p_T cut on the t distribution.

Figure 97 shows the number of events as a function of t after the whole selection discussed in Section 4.2 but with the cut of $p_T > 30$ GeV for the jets, the black dots represent the events when the proton is detected in the sector 45 and the red ones when it is detected in the sector 56. Both results are compatible except for the region $0.08 \leq |t| \leq 0.12$ GeV in which the difference between the two sectors is $\sim 30\%$ higher than the statistical uncertainty.

Investigating this issue after each stage in the selection, it was found that increasing the p_T threshold for the jets, decreases the discrepancy at low t. Figure 98 shows the t distribution for events with $p_T > 35$ GeV and $p_T > 40$ GeV, which present a difference of $\sim 10\%$ and $\sim 2\%$ at low t respectively. The discrepancy between the two sectors at low p_T threshold seems to be related to the efficiency of the trigger (Fig. 36); for events with $p_T > 30$ GeV the trigger has a efficiency $> 60\%$, while for $p_T > 40$ GeV the efficiency is $> 90\%$. The higher threshold was chosen as the nominal in the selection.

The Figure 99 shows the ratio of the single-diffractive to inclusive dijet yields comparing sector 45 and sector 56 for each p_T threshold, and Figure 100 the ratio of the two sectors taken together versus the p_T threshold.

Figure 97 - Number of events as a function of t after the full event selection with the cut in $p_T > 30$ GeV.

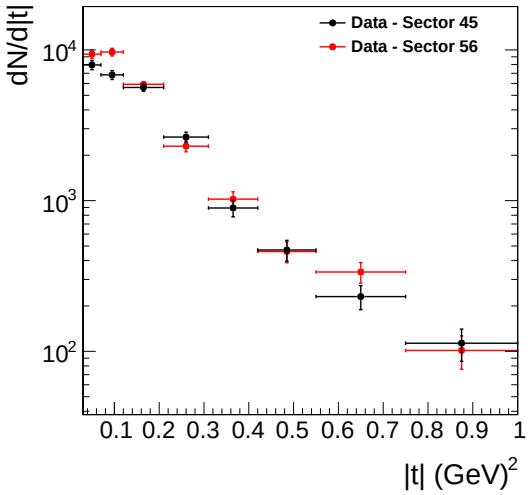

Legend: The black dots represent the events when the proton is detected in the sector 45 and the red ones when it is detected in the sector 56.
Source: The author, 2017.

Figure 98 - Number of events as a function of t after the full event selection with the cut in $p_T > 35$ GeV (left panel) and $p_T > 40$ GeV (right panel) for the jets.

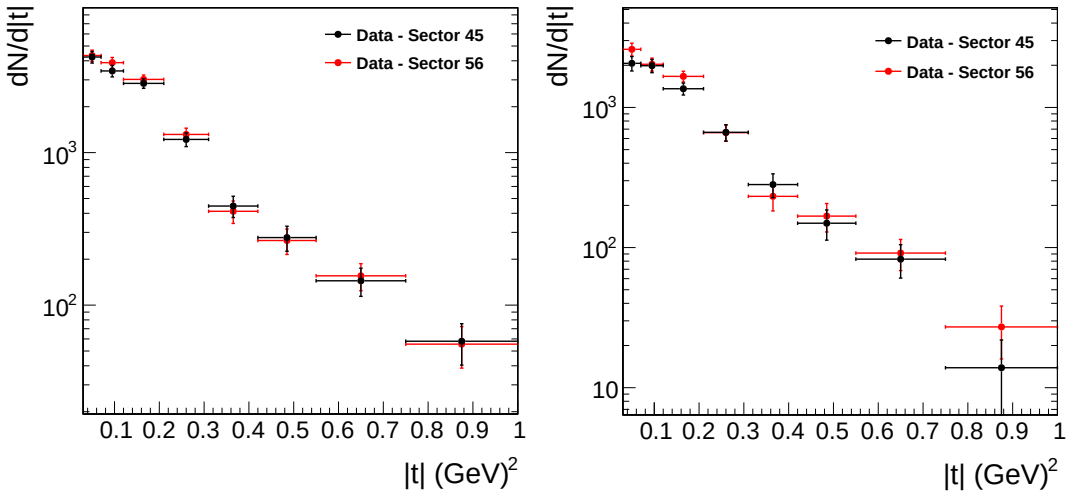

Legend: The black dots represent the events when the proton is detected in sector 45 and the red ones when it is detected in sector 56.
Source: The author, 2017.

Figure 99 - Ratio of the single-diffractive to the non-diffractive events with the cut in $p_T > 30$ GeV (left), $p_T > 35$ GeV (center) and $p_T > 40$ GeV (right).

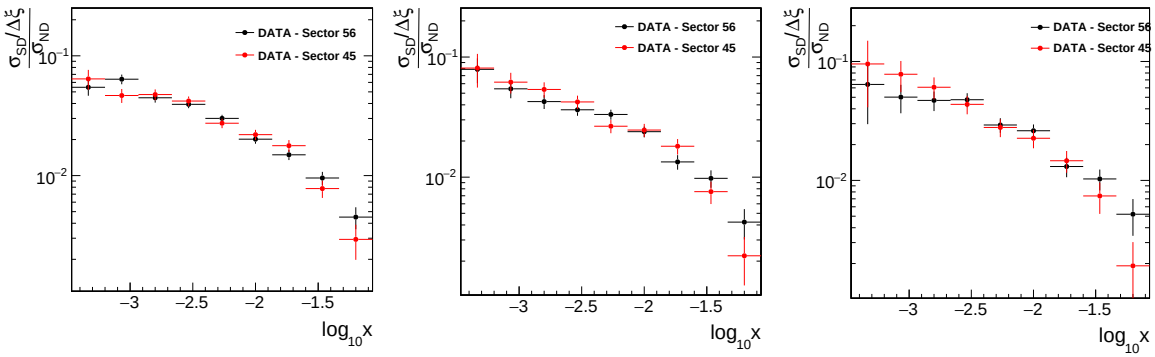

Legend: The black dots represent the events when the proton is detected in sector 45 and the red ones when it is detected in sector 56.
Source: The author, 2017.

Figure 100 - Ratio of the single-diffractive to the non-diffractive events.

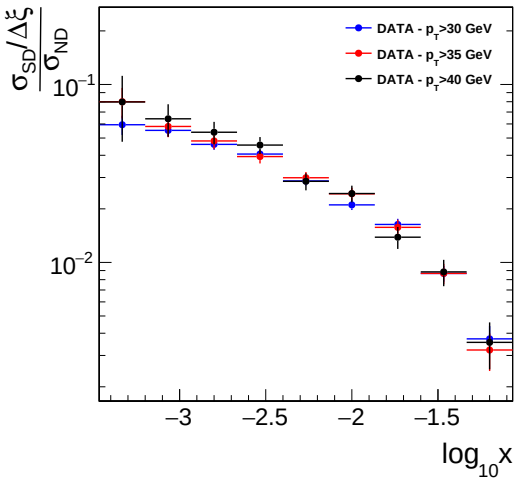

Legend: The blue dots represent the results with the cut of $p_T > 30$ GeV, the red ones with the cut of $p_T > 35$ GeV and the black ones with $p_T > 40$ GeV.
Source: The author, 2017.

APPENDIX D – Background

This section presents the results of the estimated background with an alternative ZB method.

Each MC event (both POMWIG and PYTHIA6) was associated an event taken randomly from the full ZB sample, this event may or may not contain a proton measured by TOTEM, if not the event is rejected. Around 1k of ZB events with a proton are mixed to the MC.

The POMWIG sample was normalised as discussed in Sect. 3. The mixture MC+ZB was then passed through the selection procedure illustrated in Sect. 4.2, except for the cut $\xi_{\text{CMS}} - \xi_{\text{TOTEM}} \leq 0$, which was not applied.

An event with a proton in the RPs is considered as signal if it originates from the MC sample, or as background if it originates from the ZB sample. Should an event have a proton in both MC and ZB sample, the proton with smallest ξ is chosen. The probability of such combination is however small and none of these events pass all selection cuts. The background is estimated separately for top-top and bottom-bottom RPs and the combination of these is used in the analysis. Figure 101 shows the distribution of $\xi_{\text{CMS}} - \xi_{\text{TOTEM}}$ for the data compared to the MC+ZB mixture. The requirement $\xi_{\text{CMS}} - \xi_{\text{TOTEM}} \leq 0$ selects the signal events and rejects the kinematically forbidden region populated by the background events (yellow histogram). The remaining contamination of background in the signal region was estimated to be $\sim 9.5\%$ for sector 45 and $\sim 12.8\%$ for sector 56.

Figure 102 shows the distribution of ξ_{TOTEM}, again for the data and the MC+ZB sample, before the $\xi_{\text{CMS}} - \xi_{\text{TOTEM}} \leq 0$ cut. Figure 103 shows the distribution of ξ_{TOTEM} after the $\xi_{\text{CMS}} - \xi_{\text{TOTEM}} \leq 0$ cut. The residual background after the $\xi_{\text{CMS}} - \xi_{\text{TOTEM}}$ cut is concentrated at values of ξ_{TOTEM} larger than about 0.05.

Figure 104 shows the distributions as a function of t, also after the $\xi_{\text{CMS}} - \xi_{\text{TOTEM}} \leq 0$ cut.

This method gives a good description of the background region, however few MC events are matched to a proton.

Figure 101 - Distribution of $\xi_{\mathrm{CMS}} - \xi_{\mathrm{TOTEM}}$ for sector 45 (left panel) and sector 56 (right panel).

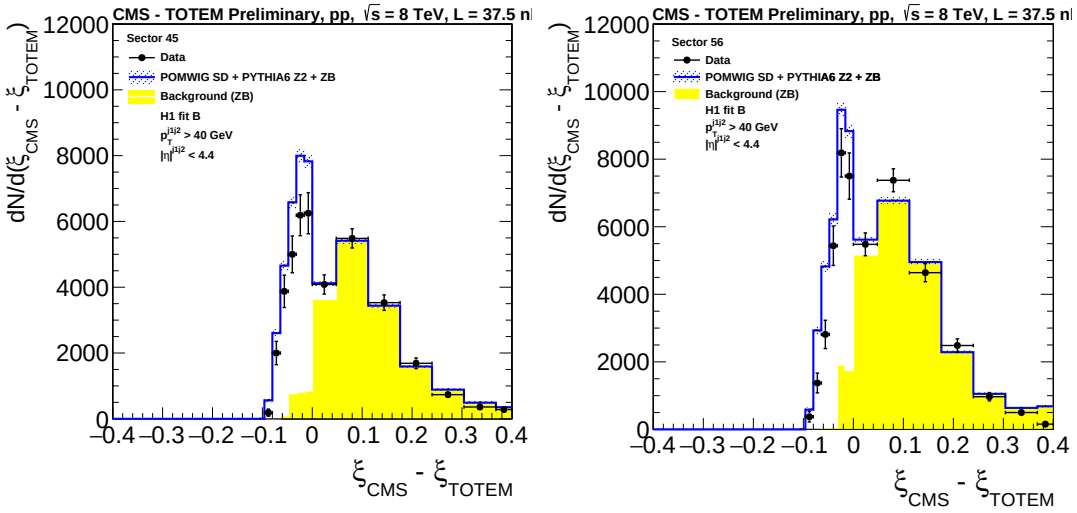

Legend: The data are indicated by full circles. The blue histogram is the mixture of Pomwig, Pythia and ZB data events described in the text. An event with the proton measured in the RPs contributes to the white histogram (signal) if it originates from the MC sample, or to the yellow histogram (background) if it originates from the ZB sample. The shaded band represents the statistical uncertainty of the MC+ZB sample, which reflects the size of the ZB sample.
Source: The author, 2017.

Figure 102 - Distribution of ξ_{TOTEM} for sector 45 (left) and sector 56 (right) before the $\xi_{\mathrm{CMS}} - \xi_{\mathrm{TOTEM}}$ cut.

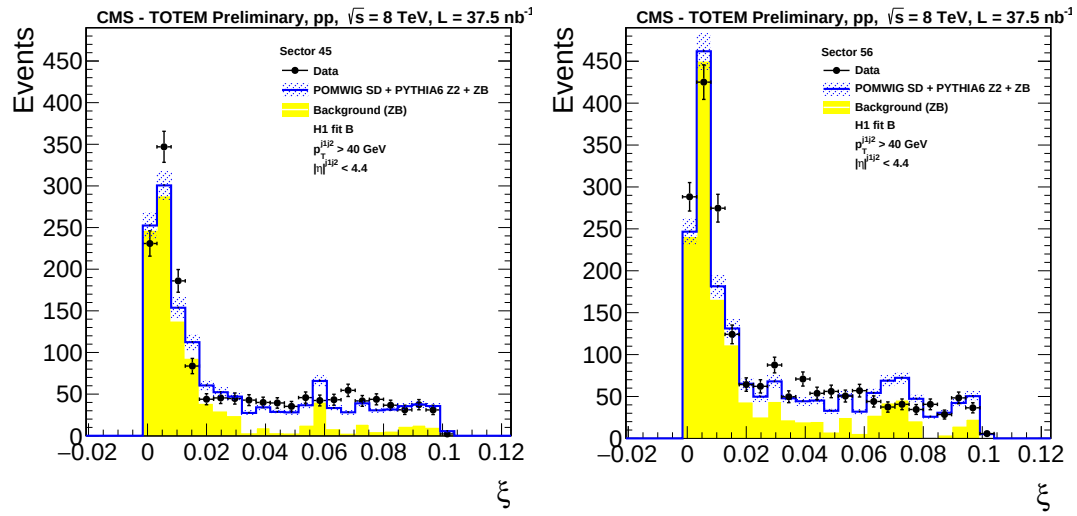

Legend: The data are indicated by full circles. The blue histogram is the mixture of Pomwig, Pythia and ZB data events described in the text. An event with the proton measured in the RPs contributes to the white histogram (signal) if it originates from the MC sample, or to the yellow histogram (background) if it originates from the ZB sample. The shaded band represents the statistical uncertainty of the MC+ZB sample, which reflects the size of the ZB sample.
Source: The author, 2017.

Figure 103 - Distribution of ξ_{TOTEM} for sector 45 (left) and for sector 56 (right) after the $\xi_{\mathrm{CMS}} - \xi_{\mathrm{TOTEM}}$ cut.

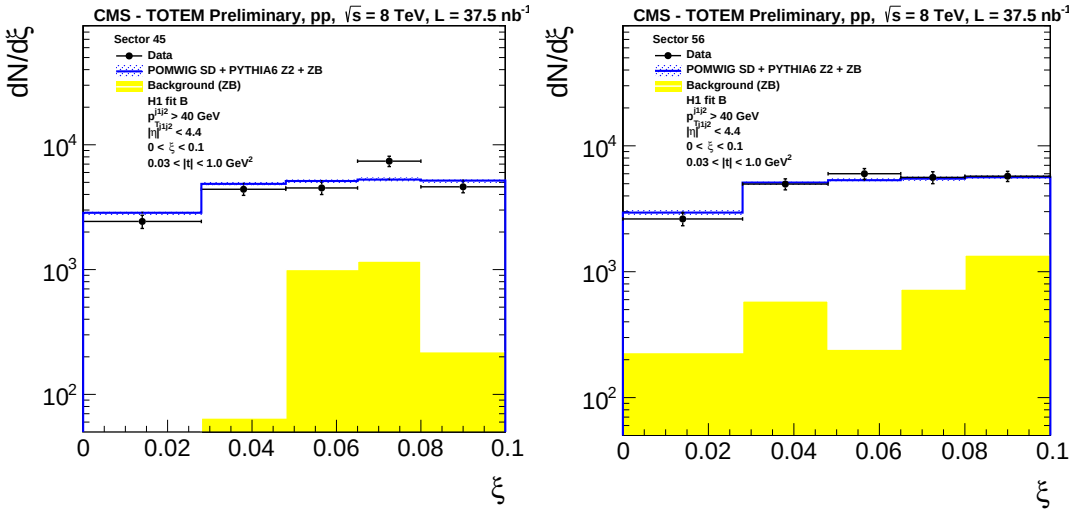

Legend: The data are indicated by full circles. The blue histogram is the mixture of Pomwig, Pythia and ZB data events described in the text. An event with the proton measured in the RPs contributes to the white histogram (signal) if it originates from the MC sample, or to the yellow histogram (background) if it originates from the ZB sample. The shaded band represents the statistical uncertainty of the MC+ZB sample, which reflects the size of the ZB sample.
Source: The author, 2017.

Figure 104 - Distribution of t for sector 45 (left panel) and for sector 56 (right panel), after all cuts including the $\xi_{\mathrm{CMS}} - \xi_{\mathrm{TOTEM}}$ cut.

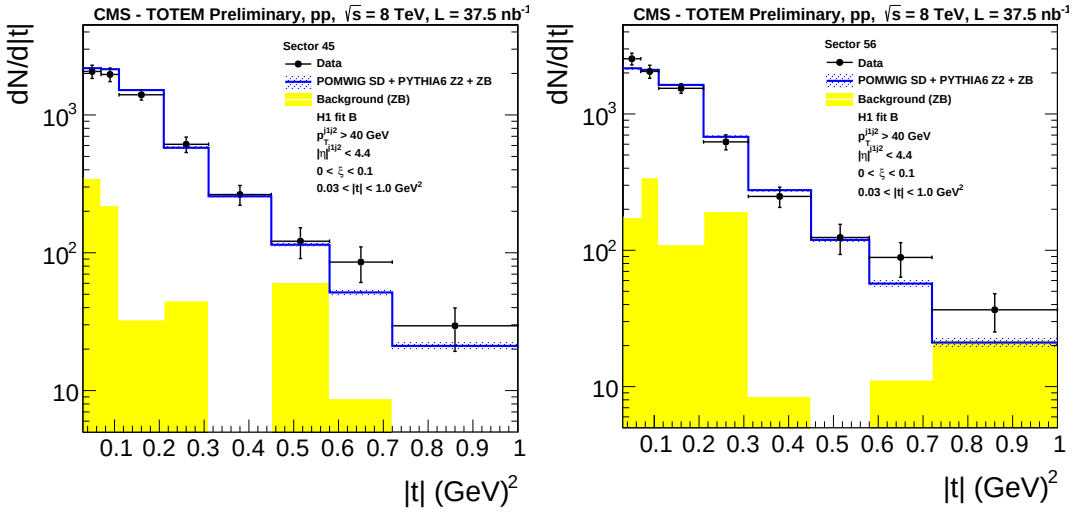

Legend: The data are indicated by full circles. The blue histogram is the mixture of Pomwig, Pythia and ZB data events described in the text. An event with the proton measured in the RPs contributes to the white histogram (signal) if it originates from the MC sample, or to the yellow histogram (background) if it originates from the ZB sample. The shaded band represents the statistical uncertainty of the MC+ZB sample, which reflects the size of the ZB sample.
Source: The author, 2017.

APPENDIX E – Systematic Uncertainties

In addition to the tables shown in Section 5.1, this chapter presents the percentages of the systematics uncertainties for each result, the cross section as a function of t, ξ, x and the ratio as a function of x.

- t **cross section:** The tables below summarize the effect of each systematic check on the cross section differential in t. Tables 14 and 15 show the values for the average and the maximum variation between all the bins for sector 45 and 56 separately. The effect of each unertainty is shown for the values of $|t| = 0.09$ GeV^2 and $|t| = 0.52$ GeV^2.

- ξ **cross section:** The tables below summarize the effect of each systematic check on the cross section differential in ξ. Tables 16 and 17 show the values for the average and the maximum variation between all the bins for sector 45 and 56 separately. The effect of each unertainty is shown for the value of $\xi = 0.056$.

- **Single-diffractive and inclussive cross section as a function of** x**:** The tables below summarize the effect of each systematic check on the cross section differential in x for the non-diffractive and single-diffractive samples. Tables 18 and 19 show the values for the average and the maximum variation between all the bins for sector 45 and 56 separately.

- **Ratio:** The tables below summarize the effect of each systematic check on the ratio in x. Tables 20 and 21 shows the values for the average and the maximum variation between all the bins for sector 45 and 56 separately. The effect of each unertainty is shown for the value of $logx = -2.27$.

Table 14 - Individual contributions of the different systematic effects to the measurement of the t cross section for sector 45.

Uncertainty source	**Sector 45**			
	Average	**Maximum**	$\|t\| = 0.09$ GeV^2	$\|t\| = 0.52$ GeV^2
Trigger efficiency	±2.45%	±2.84%	±2.42%	±2.84%
Jet energy scale	(+7.48/-14.59)%	(+20.07/73.11)%	+12.34%	(+7.60/28.10)%
Calorimeter energy scale	(+1.88/-0.67)%	(+5.49/-1.40)%	(+4.66/-1.21)%	(+0.01/-14.00)%
Background	±5.78%	±13.76%	±1.14%	±12.48%
RPs acceptance	±4.67%	±14.34%	±2.74%	±1.15%
Beam divergence	±9.08%	±19.60%	±4.40%	±14.44%
Horizontal dispersion	+(6.90/-5.12)%	+(20.39/-10.07)%	(+6.66/-4.25)%	(+20.40/-10.07)%
t-slope	±4.27%	±11.68%	±2.11%	±8.35%
β-reweighting	±1.88%	±4.45%	±1.05%	±4.31%
Acceptance and unfolding	±18.27%	±34.54%	±3.39%	±34.54%
Unfolding regularisation	±1.40%	±4.24%	±0.13%	±1.57%
Unfolding Bias	±28.90%	±74.91%	±3.13%	±57.60%
Sector difference	±9.54%	±18.24%	±0.37%	±16.00%
Total	(+39.17/-40.83)%	(+94.59/-116.39)%	(+16.72/-8.98)%	(+75.60/-78.33)%

Legend: The total uncertainty is the quadratic sum of the individual contributions. The last column present the values of each contribution for $|t| = 0.52$ GeV^2.
Source: The author, 2017.

Table 15 - Individual contributions of the different systematic effects to the measurement of the t cross section for sector 56 are shown separately.

Uncertainty source	**Sector 56**			
	Average (%)	**Maximum** (%)	$\|t\| = 0.09$ GeV^2 (%)	$\|t\| = 0.52$ GeV^2 (%)
Trigger efficiency	±2.19%	±2.57%	±2.57%	±2.40%
Jet energy scale	(+4.09/-12.29)%	(+14.23/-70.84)%	-5.44%	+6.42%
Calorimeter energy scale	(+1.54/-2.39)%	(+7.24/-7.64)%	-4.61%	+0.44%
Background	±5.07%	±13.31%	±5.79%	±6.25%
RPs acceptance	±9.77%	±45.48%	±1.12%	±5.25%
Beam divergence	±5.53%	±11.37%	±3.98%	±11.37%
Horizontal dispersion	(+6.90/-14.43)%	(+27.65/-57.28)%	(+27.65/-7.79)%	(+1.65/-3.12)%
t-slope	±4.64%	±23.66%	±0.59%	±3.04%
β-reweighting	±1.02%	±1.51%	±0.35%	±0.99%
Acceptance and unfolding	±23.85%	±102.55%	±2.43%	±49.85%
Unfolding regularisation	±2.27%	±7.26%	±0.70%	±2.23%
Unfolding Bias	±28.76%	±81.89%	±9.68%	±81.89%
Sector difference	±10.87%	±28.71%	±0.38%	±12.12%
Total	(+42.01/-45.42)%	(+148.53/-171.47)%	(+30.38/-14.48)%	(+97.97/-97.80)%

Legend: The total uncertainty is the quadratic sum of the individual contributions. The last column present the values of each contribution for $|t| = 0.52$ GeV^2.
Source: The author, 2017.

Table 16 - Individual contributions of the different systematic effects to the measurement of the ξ cross section for sector 45.

Uncertainty source	**Sector 45**		
	Average	**Maximum**	$\xi = 0.056$
Trigger efficiency	±2.49%	±2.65%	±2.43%
Jet energy scale	(+5.43/-4.58)%	(+18.26/-10.32)%	-3.67%
Calorimeter energy scale	(+2.82/-1.12)%	(+7.15/-3.21)%	-1.47%
Background	±14.80%	±29.70%	±29.70%
RPs acceptance	±1.15%	±1.63%	±1.57%
Beam divergence	±3.72%	±9.75%	±2.33%
Horizontal dispersion	(+19.07/-9.68)%	(+59.75/-31.76)%	+59.75
t-slope	±1.64%	±2.52%	±2.52%
β-reweighting	±0.48%	±1.23%	±0.49%
Acceptance and unfolding	±15.78%	±27.35%	±27.35%
Unfolding regularisation	±2.98%	±4.61%	±4.61%
Unfolding bias	±12.25%	±17.50%	±15.80%
Sector difference	±14.39%	±25.35%	±10.75%
Total	(+35.49/-31.21)%	(+81.65/-61.95)%	(+74.88/-45.30)%

Legend: The total uncertainty is the quadratic sum of the individual contributions. The last column present the values of each contribution for $\xi = 0.056$.
Source: The author, 2017.

Table 17 - Individual contributions of the different systematic effects to the measurement of the ξ cross section for sector 56.

Uncertainty source	**Sector 56**		
	Average	**Maximum**	$\xi = 0.056$
Trigger efficiency	±2.44%	±2.52%	±2.52%
Jet energy scale	(+6.85/-3.25)%	(+14.17/-6.03)%	(+4.43/-6.03)%
Calorimeter energy scale	(+3.51/-0.93)	(+13.00/-3.45)%	(+0.50/-0.66)%
Background	±4.96%	±8.59%	±4.32%
RPs acceptance	±1.26%	±2.12%	±0.41%
Beam divergence	±3.18%	±8.75%	±3.56%
Horizontal dispersion	(+12.33/-11.89)%	(+36.67/-30.93)%	-30.93%
t-slope	±1.39%	±1.99%	±0.68%
β-reweighting	±0.29%	±0.75%	0.26%
Acceptance and unfolding	±6.23%	±9.89%	±5.42%
Unfolding regularisation	±0.38%	±0.96%	±0.40%
Unfolding bias	±4.27%	±7.06%	±3.12%
Sector difference	±17.45%	±51.41%	±8.84
Total	(+24.84/-23.63)%	(+68.35/-62.95)%	(+13.26/-33.90)%

Legend: The total uncertainty is the quadratic sum of the individual contributions. The last column present the values of each contribution for $\xi = 0.056$.
Source: The author, 2017.

Table 18 - Individual contributions of the different systematic effects to the measurement of the non-diffractive dijet cross section as a function of x.

Uncertainty source	σ_{jj} **Plus side**		σ_{jj} **Minus side**	
	Average	**Maximum**	**Average**	**Maximum**
Jet energy scale	(+8.93/-7.09)%	(+14.74/-13.75)%	(+9.01/-7.30)%	(+14.92/-13.91)%
Calorimeter energy scale	+0.91%	+1.02%	+0.89%	+0.98%
Acceptance and unfolding	±2.53%	±4.75%	±2.87%	±4.58%
Unfolding regularisation	±0.01%	±0.02%	±0.01%	±0.01%
Total	(+9.71/-7.99)%	(+16.40/-15.48)%	(+10.01/-8.46)%	(+16.55/-15.61)%

Legend: The values for z-plus and z-minus sides are shown separately. The total uncertainty is the quadratic sum of the individual contributions.
Source: The author, 2017.

Table 19 - Individual contributions of the different systematic effects to the measurement of the single-diffractive cross section as a function of x.

Uncertainty source	σ_{jj}^{pX} **Sector 45**		σ_{jj}^{pX} **Sector 56**	
	Average	**Maximum**	**Average**	**Maximum**
Trigger efficiency	±2.50%	±3.06%	±2.59%	±4.30%
Jet energy scale	(+8.05/-5.52)%	(+22.00/-20.85)%	(+7.12/-3.50)%	(+28.35/-11.32)%
Calorimeter energy scale	(+2.40/-0.61)%	(+8.62/-1.28)%	(+1.55/-1.71)%	(+3.44/-5.02)%
Background	±26.16%	±69.44%	±20.72%	±97.17%
RPs acceptance	±0.67%	±1.04%	±0.72%	±1.10%
Beam-divergence	±1.98%	±3.66%	±1.50%	±2.33%
t-slope	±1.63%	±2.32%	±1.50%	±1.93%
β-reweighting	±4.69%	±11.75%	±4.74%	±15.22%
Acceptance and unfolding	±7.73%	±18.01%	±9.62%	±30.75%
Unfolding regularisation	±0.22%	±0.86%	±2.01%	±5.63%
Unfolding bias	±9.40%	±29.17%	±8.36%	±17.59%
Sector difference	±29.08%	±87.13%	±42.20%	±90.99%
Total	(+42.69/-41.92)%	(+120.92/-119.80)%	(+50.82/-49.69)%	(+179.99/-118.05)%

Legend: The values for sector 45 and 56 are shown separately. The total uncertainty is the quadratic sum of the individual contributions.
Source: The author, 2017.

Table 20 - Individual contributions of the different systematic effects to the measurement of the single-diffractive to non-diffractive dijet yields for sector 45.

Uncertainty source	$\sigma_{jj}^{pX}/\sigma_{jj}$ **Sector 45**		
	Average	**Maximum**	$logx = -2.27$
Trigger efficiency	±2.50%	±3.07%	±2.29%
Jet energy scale	(+4.75/-3.73)%	(+18.16/-6.47)%	(+1.24/-0.22)%
Calorimeter energy scale	(+1.86/-1.39)%	(+7.60/-2.24)%	+1.27%
Background	±26.15%	±69.43%	±23.29%
RPs acceptance	±0.68%	±1.05%	±0.46%
Beam-divergence	±2.00%	±3.69%	±3.69%
Horizontal dispersion	(+6.19/-3.62)%	(+17.51/-12.60)%	-4.11%
t-slope	±1.64%	±2.32%	±1.88%
β-reweighting	±4.68%	±11.75%	±0.08%
Acceptance and unfolding	±7.49%	±15.93%	±1.87%
Unfolding regularisation	±0.22%	±0.88%	±0.01%
Unfolding bias	±8.54%	±25.44%	±2.00%
Sector difference	±29.49%	±87.25%	±29.88%
Total	(+42.21/-41.79)%	(+119.15/-117.08)%	(+38.32/-38.50)%

Legend: The total uncertainty is the quadratic sum of the individual contributions. The last column present the values of each contribution for $logx = -2.27$.
Source: The author, 2017.

Table 21 - Individual contributions of the different systematic effects to the measurement of the single-diffractive to non-diffractive dijet yields for sector 56.

Uncertainty source	$\sigma_{jj}^{pX}/\sigma_{jj}$ **Sector 56**		
	Average	**Maximum**	$logx = -2.27$
Trigger efficiency	±2.59%	±4.30%	±2.13%
Jet energy scale	(+5.08/-4.63)%	(+16.42/-11.09)%	(+4.02/-4.13)%
Calorimeter energy scale	(+0.95/-2.49)%	(+2.57/-5.96)%	+(1.56/-2.71)%
Background	±20.79%	±97.76%	±1.41%
RPs acceptance	±0.72%	±1.00%	±0.63%
Beam-divergence	±1.50%	±2.33%	±2.33%
Horizontal dispersion	(+10.92/-6.59)%	(+28.73/-15.19)%	(+0.69/-14.04)%
t-slope	±1.50%	±1.93%	±1.93%
β-reweighting	±4.75%	±15.30%	±0.23%
Acceptance and unfolding	±10.60%	±27.11%	±10.08%
Unfolding regularisation	±2.02%	±5.73%	±1.05%
Unfolding bias	±9.28%	±15.05%	±11.98%
Sector difference	±42.62%	±99.72%	±18.70%
Total	(+51.30/-50.56)%	(+149.79/-144.70)%	(+25.13/-28.88)%

Legend: The total uncertainty is the quadratic sum of the individual contributions. The last column present the values of each contribution for $logx = -2.27$.
Source: The author, 2017.

APPENDIX F – Prompt Reconstruction vs Reprocessed data

The calibration procedure is designed to take place at different times during and after the data taking, with increasing degree of precision. The prompt reconstruction of physics objects is obtained within 48 hours from the data taking, using the "prompt" determination of the calibration constants. The offline calibration take place well after the data taking and aims at providing the best understanding of the detector. The offline calibration and alignment procedure is performed and used for data reprocessing with ultimate accuracy. This section compares the results obtained with prompt reconstruction and data reprocessing.

Table 22 shows the number of merged events, luminosity and efficiency for each CMS run. The table presents the information for prompt reconstruction and reprocessed data.

The number of events after the full selection as decribed in Sec. 4.2 with the proton detected in the RPs in sector 45 (56) for PromptReco data is 390 (445) and for ReReco it is 376 (411).

The quantity of background calculated as described in Sec. 4.3 with PromptReco data was found to be 7.6%(9.6%) for sector 45 (56) and 7.2% (9.9%) for sector 45 (56) with ReReco data.

Figure 105 compares the cross section a function of t and ξ with prompt reconstruction data and with reprocessed data, the ratio of single-diffractive and inclusive cross sections as a function of x is shown as well.

Table 22 - Merged CMS+TOTEM samples for dijets events at 8 TeV.

	CMS Run	**Sample**	**Number of Events**	**L** (nb^{-1})	**Eff**	**L*Eff** (nb^{-1})
PromptReco	198902	/LP_Jets1/Run2012C-PromptReco-v1/RECO	836948	31.76	89%	28.27
		/LP_Jets2/Run2012C-PromptReco-v1/RECO	816961			
	198903	/LP_Jets1/Run2012C-PromptReco-v1/RECO	466932	17.40	95%	16.53
		/LP_Jets2/Run2012C-PromptReco-v1/RECO	466930			
ReReco	198902	/LP_Jets1/Run2012C-22Jan2013-v1/RECO	814568	31.87	87%	27.73
		/LP_Jets2/Run2012C-22Jan2013-v1/RECO	815514			
	198903	/LP_Jets1/Run2012C-22Jan2013-v1/RECO	466934	17.40	91%	15.83
		/LP_Jets2/Run2012C-22Jan2013-v1/RECO	466929			

Legend: The Table shows the run numbers for the CMS experiment, the number of events, luminosity and efficiency. The latter refers to the merging efficiency. PromptReco refers to prompt reconstruction data and ReReco to the reprocessed data.
Source: The author, 2017.

Figure 105 - Cross sections as a function of t and ξ.

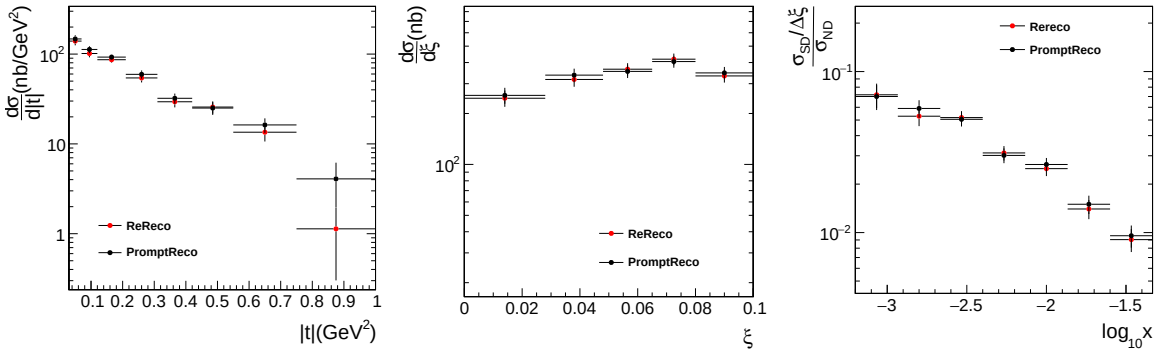

Legend: Ratio of the single-diffractive to the non-diffractive event yields. The black dots represent the result using the prompt reconstruction data, the red dots represent the result using the reprocessed data.

Source: The author, 2017.